

Investigation of Oscillations in Idealized Katabatic Slope Flows

by

Sebastian Henao-Garcia

B.Sc. Mechanical Engineering, Universidad Nacional de Colombia, 2018

Submitted to the Graduate Faculty of
the Swanson School of Engineering in partial fulfillment
of the requirements for the degree of
Master of Science

University of Pittsburgh

2021

UNIVERSITY OF PITTSBURGH
SWANSON SCHOOL OF ENGINEERING

This thesis was presented

by

Sebastian Henao-Garcia

It was defended on

July 12, 2021

and approved by

Dr. Inanc Senocak, Department of Mechanical Engineering and Materials Science

Dr. Shervin Sammak, Department of Mechanical Engineering and Materials Science

Dr. Jeffrey S. Vipperman, Department of Mechanical Engineering and Materials Science

Copyright © by Sebastian Henao-Garcia
2021

Investigation of Oscillations in Idealized Katabatic Slope Flows

Sebastian Henao-Garcia, M.S.

University of Pittsburgh, 2021

Katabatic winds are down-slope, drainage flows that are characterized by strong jets of cold air capped by a reverse flow. Katabatic winds typically form when air right above a sloping surface cools rapidly due to radiative heat transfer to clear skies and, subsequently, gets transported down the slope by the action of gravity. Idealized katabatic flows form the theoretical foundation for exploring turbulent winds over complex terrains under stably stratified atmospheric conditions. Recent numerical investigations of idealized katabatic flows have established the presence of organized vortical structures in the laminar flow regime along with an instability map as a function of relevant slope flow dimensionless parameters, including a recently introduced stratification perturbation parameter. The current thesis investigates the oscillatory dynamics of these vortical rolls through direct numerical simulations of idealized katabatic flows for numerous points in the instability map. The simulation results further confirm the presence of both temporal and spatial oscillations in the flow fields that are associated with the emergence and propagation of flow instabilities. Damped *en masse* oscillations, which were previously identified in the context of turbulent slope flows, are observed to dominate the initial oscillatory stage of laminar katabatic slope flows as well. Unlike in the turbulent regime, these *en masse* oscillations become insignificant at most heights in the dynamically unstable laminar regime with the emergence of well-defined flow instabilities. Stationary longitudinal rolls, which are dominant at shallow slopes, are observed to meander with increasing stratification perturbation parameter. Traveling slope waves, which emerge on very steep slopes, are observed to be transported by the mean jet velocity of the flow. Both types of instability rolls coexist for certain combinations of the dimensionless parameter space, forming intricate structures that break into turbulence as the flow becomes more dynamically unstable.

Table of Contents

Preface	ix
1.0 Introduction	1
1.1 Prior Work	4
1.2 Thesis Statement	10
2.0 Technical Background	11
2.1 Governing Equations	11
2.2 Prandtl’s Laminar Solution	13
2.3 Relevant Dimensionless Parameters and Flow Scales	14
2.4 Instability Map	16
2.5 Direct Numerical Simulations	19
2.6 Data Analysis in the Frequency and Wavelength Domains	20
2.7 Reduced-Order Model Formulation	24
3.0 Results	27
3.1 Instability Modes	27
3.2 <i>En Masse</i> Oscillations’ Dynamics	39
3.3 Instability of the Longitudinal Rolls	43
3.4 Progression Toward Turbulence	46
3.5 Longitudinal Rolls Dynamics	57
3.6 Traveling Wave Rolls	59
3.7 Reduced-Order Representation of Instabilities	69
4.0 Summary	82
4.1 Overall Dynamics of Instabilities	82
4.2 Longitudinal Rolls Dynamics	83
4.3 Traveling Wave Dynamics	84
4.4 Future Work	84
Appendix A. MATLAB Implementation of the PSD Estimate	86

Appendix B. MATLAB Implementation of the DMD algorithm	87
Bibliography	89

List of Figures

1.1	Slope flow under katabatic conditions	2
2.1	Prandtl’s laminar solution	14
2.2	Instability map for katabatic flows	17
2.3	Analyzing a temporal signal in the frequency domain	23
2.4	Analyzing a spatial signal in the wavelength domain	23
3.1	Temporal signal breakdown - Longitudinal instability rolls	29
3.2	Temporal signal breakdown - Traveling wave instability rolls	30
3.3	Temporal signal breakdown - Mixed instability rolls	31
3.4	Longitudinal vorticity rolls	33
3.5	Longitudinal rolls in contour plots	34
3.6	Traveling wave vorticity rolls	35
3.7	Traveling wave rolls in contour plots	36
3.8	Mixed vorticity rolls	37
3.9	Mixed instability rolls in contour plots	38
3.10	<i>En masse</i> oscillations dynamics for multiple slope flow parameters	41
3.11	Most dominant frequency in the initial oscillatory regime for changing N and α	42
3.12	Amplitude decay of <i>en masse</i> oscillations for multiple simulation parameters	42
3.13	Longitudinal rolls disturbance with increasing Π_S for a fixed slope $\alpha = 50^\circ$	44
3.14	Refined instability map	45
3.15	Unstable longitudinal rolls for large domain sizes	45
3.16	Vorticity structures at low Π_s numbers	49
3.17	Contour plot visualizations at low Π_s numbers	50
3.18	Vorticity structures at moderate Π_s numbers	51
3.19	Contour plot visualizations at moderate Π_s numbers	52
3.20	Vorticity structures at high Π_s numbers	53
3.21	Contour plot visualizations at high Π_s numbers	54

3.22	Zoomed frequency spectra for low, moderate, and high Π_s values	55
3.23	Complete frequency spectra for low, moderate, and high Π_s values	56
3.24	Longitudinal rolls wavelength along the cross-slope direction	58
3.25	Longitudinal rolls wavelength as a function of α and Π_s	58
3.26	Temporal and spatial PSD for $\alpha = 80^\circ, \Pi_s = 20$	60
3.27	Temporal and spatial PSD for $\alpha = 80^\circ, \Pi_s = 40$	60
3.28	Most dominant frequencies at multiple heights for $\alpha = 80^\circ, \Pi_s = 20$	62
3.29	Most dominant frequencies at multiple heights for $\alpha = 20^\circ, \Pi_s = 4$	63
3.30	Normalized traveling wave speed as a function of Π_s	65
3.31	Normalized mean jet velocity as a function of Π_s	65
3.32	Normalized traveling wave frequency as a function of Π_s	66
3.33	Normalized traveling wave wavelength as a function of Π_s	66
3.34	Curved traveling wave rolls for large domain sizes - $L_y = 800l_0$	67
3.35	Curved traveling wave rolls for large domain sizes - $L_y = 2400l_0$	68
3.36	SVD eigenvalues for $\alpha = 20^\circ, \Pi_s = 4$	71
3.37	DMD modes and eigenvalues for $\alpha = 20^\circ, \Pi_s = 40$	72
3.38	DMD reconstruction for $\alpha = 20^\circ, \Pi_s = 4$	72
3.39	Spatial PSD of most dominant DMD mode for $\alpha = 20^\circ, \Pi_s = 4$	73
3.40	SVD eigenvalues for $\alpha = 80^\circ, \Pi_s = 20$	74
3.41	DMD modes and eigenvalues for $\alpha = 80^\circ, \Pi_s = 20$	75
3.42	DMD reconstruction for $\alpha = 80^\circ, \Pi_s = 20$	76
3.43	Spatial PSD of the second most dominant DMD mode for $\alpha = 80^\circ, \Pi_s = 20$	76
3.44	Temporal PSD from the DMD reconstruction for $\alpha = 80^\circ, \Pi_s = 20$	77
3.45	SVD eigenvalues for $\alpha = 60^\circ, \Pi_s = 30$	78
3.46	DMD modes and eigenvalues for $\alpha = 60^\circ, \Pi_s = 30$	79
3.47	DMD reconstruction for $\alpha = 60^\circ, \Pi_s = 30$	80
3.48	Spatial PSD of most dominant DMD modes for $\alpha = 60^\circ, \Pi_s = 30$	80
3.49	Temporal PSD from the DMD reconstruction for $\alpha = 60^\circ, \Pi_s = 30$	81

Preface

I am incredibly grateful to everyone who has supported me through my graduate studies at Pitt. Firstly, I would like to thank Dr. Inanc Senocak for the opportunity to work together on the research leading to the completion of this thesis. He has been a great source of support to navigate such challenging concepts, and I have grown into a better researcher from our academic interactions. I also want to thank my committee members Dr. Shervin Sammak and Dr. Jeffrey Vipperman for accepting to go through this exciting academic journey with me. Additionally, Dr. Peyman Givi and Dr. Anne M. Robertson provided me with lots of tools to better navigate academia. Thank you all.

Thank you as well to everyone in the High-Performance Simulation Laboratory for Thermo-Fluids (HiPerSimLab) for welcoming me to Pittsburgh and for all the good times we shared. I want to specifically thank Dr. Chengnian Xiao for the countless hours we spent discussing the katabatic flow business together, and Dustin Ma for all his support with the use of GIN3D.

I dedicate this thesis to my mom Yanet Garcia-Gonzalez, who is the engine of my life by empowering and encouraging me through every challenge. This final product would have not been possible without the incredible support from my friends Jessica, Alexis, and Katia. There is a piece of you all in this manuscript.

Computational resources were provided by the Center for Research Computing (CRC) at the University of Pittsburgh, and this research was partially supported by the National Science Foundation under Grant No. 1936445.

1.0 Introduction

Katabatic flows constitute an atmospheric flow phenomenon characterized by strong jets of cold air flowing downslope along inclined terrains as a product of net radiative cooling of the ground surface (Fig. 1.1). Such slope flows, also known as drainage winds, typically take place during calm nights with clear skies over continental mountainous regions, starting before midnight and with an average duration in the order of a few hours. In high latitudes, however, where slope distances can extend for hundreds of kilometers, katabatic flows can also be observed during day time and can last multiple days. Along such vast surfaces, Coriolis effects deviate the jet's direction from the along-slope direction, yet these effects are negligible over less extensive surfaces, on which the along-slope velocity component dominates over the cross-slope and slope-normal components [1, 2, 3].

From a fluid dynamics perspective, katabatic flows are gravity-driven (or equivalently buoyancy-driven) boundary-layer flows happening as a consequence of stably stratified atmospheres forming above sloping surfaces which are subject to net radiative cooling. When the surface cools down against a background stable environment, a slope-normal temperature gradient is formed between the colder surface and the warmer atmosphere, a phenomenon known as surface inversion. This kind of slope-normal temperature profile features a layer of colder, and hence denser, air lying above the surface resulting in the formation of horizontal temperature, density, and pressure gradients for a given vertical height. Gravity then accelerates the heavier air down the slope against the stably stratified atmosphere and viscous friction forces at the surface, thus leading to the formation of a velocity jet pointing downslope that displays a maximum velocity just above the surface. When the net radiative cooling is replaced in the physical setting described above by a net radiative heating—typically happening after sunrise—the air in contact with the surface gets warmer, and hence less dense, causing it to rise because of buoyancy. For such flows, known as anabatic flows, the horizontal pressure gradient reverses and pushes the air against the surface, causing the warmer air to move up in the direction of the slope rather than rising vertically, thus resulting in a jet-like velocity profile pointing upslope [1, 2, 3, 4].

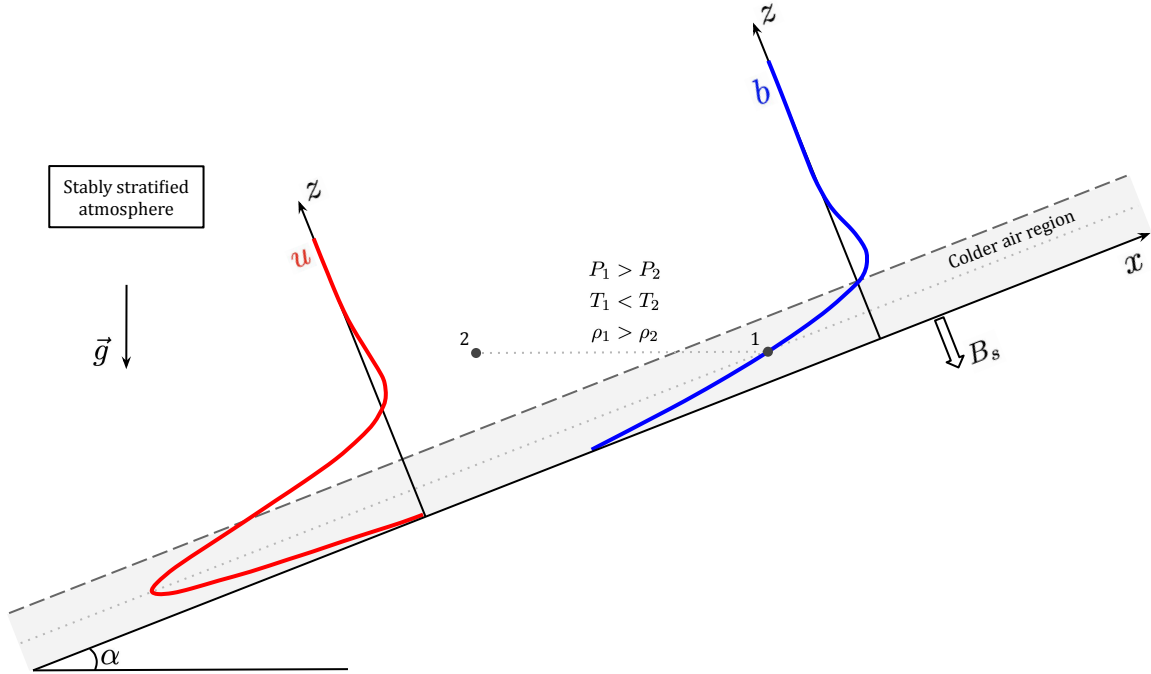


Figure 1.1: Slope flow under katabatic conditions. The along-slope velocity profile u is depicted in red and the buoyancy profile b is depicted in blue. The surface buoyancy flux is denoted by B_s and \vec{g} represents the gravity vector.

Katabatic flows, as a local wind phenomenon, are particularly strong over large-scale ice sheets and snow-covered inclined terrains, despite being part of diurnal-cycle effects on continental mountainous regions at a smaller scale. In both scenarios, however, such slope flows have implications in multiple regional-scale circulations [1]. In polar latitudes, they can reach hurricane forces and control local climate, affecting atmospheric circulation and contributing to ablation of ice sheets, i.e. near-surface removal of ice, given the turbulence fluxes of sensible heat appearing in the energy budget [5, 6, 7, 8, 9, 10, 11]. In continental terrains, they impact the local weather in mountainous regions. Air quality on such regions is closely coupled to the dynamics of slope flows, and stable atmospheres are known to be an aggravating factor regarding air pollutant dispersion issues [12, 13, 14]. Their impact also spans to other human activities happening within the troposphere, such as aviation,

agriculture, wind energy generation, and military and fire fighting operations. Particularly, katabatic flows affect fog formation, hence having a significant impact on the visibility and energy usage conditions on such human activities [15, 16, 17, 18, 19].

Despite recent advances in the understanding of the heat and fluid dynamics principles underlying katabatic flows, they remain an open area of research within the atmospheric science community. Primarily, the stable atmospheric boundary layer (ABL), as described by Mahrt [20], is indeed a challenging phenomenon given the turbulent and nonturbulent motions that coexist in the flow at a wide range of scales. When stable conditions are present on ABLs, a qualitative classification scheme would yield in two regimes, namely the weakly stable ABL and the very stable ABL. The former can be modeled through the Monin-Obukhov similarity theory [21] and exhibits well-defined boundary layer velocity and potential temperature profiles, on which the turbulent kinetic energy (TKE) continuously decreases with height. As stability increases in the flow, however, the classical definition of turbulence becomes harder to identify, to the point that the very stable regime cannot be modeled as a traditional boundary layer flow. In such a regime, which is the one leading to the occurrence of katabatic flows, the TKE might increase with height and then start decreasing after reaching a maximum. This behavior limits the applicability of similarity theory to describe the very stable regime, and a complete understanding of the underlying physics remains to be formulated. Particularly, there are organized vortical structures emerging in such stable ABLs that are not yet fully understood and direct numerical simulations (DNS) are a promising tool to shed light into their dynamics, overcoming current challenges in high-resolution temporal and spatial data collection from field observations.

Such organized vortical structures manifest themselves as instability modes emerging as the slope flow becomes more dynamically unstable, constituting a nonlinear and unstable phenomenon that is still not fully turbulent. Hypotheses about these instability modes have been formulated based on field measurements, where strong wave-like motions have been observed on signals collected in the temporal domain, and observations in the spatial domain based on fog patterns have revealed the presence of such organized vortical structures [20]. However, a full characterization of the unstable motions have not been possible based on experimental data alone. A milestone in the study of such instabilities came from the

contributions of Xiao and Senocak [22], who, based on the exact solution for an prototype katabatic flow scenario, established an instability map through linear stability analysis that predicts the organized vortical structures emerging in the flow, known as instability modes, as a function of the dimensionless slope flow parameters. Entire flow field visualizations obtained through DNS confirmed the existence of such structures, and the current challenge then becomes leveraging such high-resolution spatial and temporal flow field data to explore the underlying relationship between the slope flow parameters and the instability modes' dynamics, with a particular interest on understanding how these organized vortical structures evolve as the flow becomes turbulent and how the wave-like motions can be characterized.

1.1 Prior Work

Katabatic flows have received a large amount of attention from the atmospheric science community over the course of the last century given the challenging physical phenomenon they represent by combining atmospheric stratification, heat transfer, buoyant forcing, instabilities, turbulence, and flows over complex terrains all together. The first hypotheses about the nature of such flows came from field observations, which were followed by quantitative descriptions of the physical phenomenon under certain prototype scenarios through analytical models, and later, with advances in computing power, a more structured understanding of the flows became possible through computer simulations.

One of the earliest experimental campaigns reported about katabatic flows dates back to 1933 [23], and since then a plethora of experimental data has been collected all over the world and reported in the literature up to current times. Heywood [23] reported an experimental campaign that took place between 1929 and 1931 over a slope of about 2° . The velocity and temperature measurements revealed that katabatic flows are always accompanied by a surface inversion, and they observed how clear skies were the most favorable condition for katabatic flows while the formation of cold air ponds at the bottom of the valleys could cause the slope flows to stop. Such experimental measurements, however, were not continuous and could only be started for a limited time when there was a likelihood of a clear night. These

limitations were overcome in later experimental campaigns, where continuous measurements were taken over extended periods of time by using higher resolution instruments that could cover a greater slope-normal distance for collecting data in the temporal domain. Still the sampling frequency remained a limiting factor for observing high-frequency, or equivalently small-period, phenomena.

Among such improved experimental campaigns are the one reported by Horst and Doran in 1986 [24] over slopes ranging from 6.5° to 22° , and the one reported both by Helmis and Papadopoulos in 1996 [25] and by Papadopoulos et al. in 1997 [26] over slopes ranging from 9° to 34° . These measurements provided more details about the physics leading to the emergence of the katabatic flows and confirmed earlier conclusions about their nature. The authors reported good agreement between the experimental measurements and available analytical formulations for the averaged bulk flow quantities integrated along the slope-normal direction. These experimental results featured large-period oscillations, whose frequency changed in time for both the velocity and temperature temporal signals, thus defining multiple oscillatory regimes in the flow with a possible phase lag in the signals for each flow field.

More recent experimental campaigns include the ones reported by Geiss and Mahrt in 2015 [27] over a 2° slope and by Stipersky et al. in 2020 [28] over a 1° slope featuring data in the temporal domain only. Geiss and Mahrt [27] computed a reduced-order representation of their entire experimental data set through the Singular Value Decomposition (SVD), finding that only a few SVD modes have the power to represent the entire data set and hence providing insight about the presence of organized vortical structures in the flow. Stipersky et al. [28], on the other hand, analyzed the structure of turbulence on katabatic flows featuring a high-frequency sampling rate of 20 Hz and compared it against the expected structure above flat terrain. Large differences were found between these two flow scenarios despite the shallow slope analyzed, namely a smaller boundary layer height and constant eddy size observed for the katabatic flows. They argued that the jet's maximum velocity is a source of turbulence and stressed the importance of appropriately including the slope's effect on numerical models. Regarding experimental measurements in the spatial domain, several field observations based on natural and machine-generated fog, as reported by Mahrt

[20], have revealed the presence of submeso motions, i.e. nonturbulent motions on scales smaller than 2 km, in katabatic flows. These motions have been observed to include both wave-like and non-wave-like motions, and the experimental data available has shown how the waves' amplitude can evolve in time and how the non-wave motions are mainly two dimensional. Yet, no complete parameterization of these motions is available and their relationship with turbulent motions requires further investigation, for which Mahrt stresses the need of both developing new observational approaches and formulating models that respond to the observed physics.

The first quantitative approach to describe katabatic flows under an idealized scenario was proposed by Prandtl in 1942 [29] and has been revised by multiple authors since then [30, 3, 31, 32]. The base prototype katabatic flow scenario is represented by an infinitely long surface in all directions inclined with a constant slope. The surface is subject to uniform and constant cooling and the atmosphere above features a linear and stable stratification with constant viscosity. Prandtl also assumed the flow to be parallel to the slope, laminar, and steady, resulting in an idealized solution defined by one-dimensional velocity and buoyancy profiles that exhibit a jet pointing downslope with a maximum right above the surface followed by a weaker reverse jet, as shown in Fig. 1.1. The original model was formulated with a prescribed temperature at the surface, and was later modified by Fedorovich and Shapiro [3] to include the scenario where a heat flux, or equivalently buoyancy flux, is prescribed instead. Despite its simplicity, this analytical model for slope flows qualitatively resembles the structure of the katabatic flows observed in nature, and can be extended to more intricate atmospheric conditions, as shown by Lykosov and Gutman [32], who included the presence of an ambient wind aloft the surface, in contrast to the original model that assumed the flow far away from the surface to be quiescent [3].

The simple laminar and steady Prandtl's solution has enabled the formulation of more refined models that provide greater insight into the nature of katabatic flows. Fedorovich and Shapiro [31] formulated the analytical solution for a transient slope flow scenario that started from rest and reached Prandtl's solution as the steady state response. The proposed analytical solution consists of an oscillator whose amplitude, damping rate, frequency, and phase are controlled by the dynamics of the surface shear stress. Particularly, the surface

shear stress was found to converge to a constant value much faster than the rest of the flow fields, thus weakening the damping of the oscillators of those fields and causing a longer persistence of this oscillatory behavior in the flow, although eventually converging to the steady state solution. These oscillations, denoted as *en masse* oscillations, confirm the oscillatory behavior observed in previous numerical simulations of stratified anabatic and katabatic flows, which had initially been associated with internal gravity waves [3, 2]. The characteristic frequency of the *en masse* oscillations was found to match the natural buoyancy frequency of the flow $N \sin \alpha$, being a function of both the slope angle α and the Brunt–Väisälä frequency N , where N^2 is a measure of the background stratification.

An additional model based on Prandtl’s slope flow solution has been obtained through Linear Stability Analysis applied to the simple laminar solution to assess the growth of instabilities in the flow from infinitesimal disturbances. Xiao and Senocak have applied this technique to slope flows under katabatic conditions with both quiescent flow aloft [33] and ambient winds [34], and anabatic conditions [22]. Their contributions have shown the existence of organized vortical structures in the unstable laminar regime and provide instability maps that predict the emergence of three types of instability, namely stationary longitudinal rolls aligned along the slope direction, called transverse mode; traveling wave rolls aligned along the cross-slope direction that move along the slope direction, called longitudinal mode; and a higher-order mixed mode regime, where both the longitudinal and traveling wave rolls are interwoven and coexist in the flow. These instability maps are presented as a function of the dimensionless slope flow parameters identified through the Buckingham π theorem, namely the Prandtl number Pr , the slope angle α , and a newly introduced stratification perturbation parameter Π_s .

With the advent of increased computing power in the late 1980s, carrying out computer simulations of atmospheric-scale flow phenomena became possible. As reported by Mason and Derbyshire [35], Large-Eddy Simulation (LES) is a feasible tool for numerically assessing the stably stratified atmospheric boundary layer over flat terrains despite limitations regarding computational power, the scales that can be resolved for, and the challenges of simulating the very stable regime. Schumann [2] carried out wall-modeled LES of slope flow under turbulent anabatic conditions. The simulations considered the Prandtl’s slope flow

scenario with an infinitely long surface subject to a constant and uniform heat flux with the additional inclusion of surface roughness. The uniformly stratified atmosphere above is initially at rest and no rotation is considered in the setup. The obtained results further confirmed the benefits of the reliable and detailed picture LES provides of the nature of slope flows, highlighting a weak dependence on the surface roughness and an oscillatory behavior governed by the *en masse* oscillations. Indeed, this work represents the first evidence of the presence of such oscillations in the flow, which were initially regarded as gravity oscillations and required the implementation of a relaxation algorithm in the simulations such that the numerical solution would reach a steady state sooner. The focus of these simulations was to assess the structure of the turbulent boundary layer, and hypotheses about the presence of slope-dependent organized vortical structures generated both by shear and buoyancy were confirmed as a mechanism for turbulence generation. Signatures of the longitudinal and traveling wave rolls were observed, attributing the latter to Kelvin-Helmholtz waves.

Numerical investigations of turbulent slope flows under both katabatic and anabatic conditions were also carried out by Fedorovich and Shapiro [3] through DNS, leveraging more advanced computing resources that allow to resolve for all scales in the flow and to analyze the long-term response of the flow with longer simulated times, which were the main limitations of previous works using LES. The used physical simulation setup corresponds to the prototype katabatic flow scenario, and their results for instantaneous and mean flow field quantities exhibit both turbulent fine-scale fluctuations that vanished with increasing height and *en masse* oscillations in all locations above the surface. They did not observe any damping on the *en masse* oscillations and concluded that their persistence in the flow was a natural and expected condition. This conclusion was reaffirmed in their later work with an analytical formulation of the transient Prandtl’s model [31], whose oscillatory dynamics were found to be in good agreement with the *en masse* oscillations observed in the simulations. Not explicitly reported, though, is the domain size used for their turbulent slope flow simulations, which is a potential constraining factor for the development of a different set of motions that could overtake the *en masse* oscillations. The simulation results also revealed how the turbulent katabatic flows resemble Prandtl’s laminar profile more than their anabatic counterparts, and confirmed the absence of constant turbulent fluxes, thus limiting

the applicability of similarity theory to these kinds of slope flows. They also did not observe any scale separation that would allow for any of the slope flow parameters to be dropped from the analysis.

Additional numerical slope flow simulations include the contributions of Umphrey et al. [36], who carried out DNS simulations of katabatic flows implementing several immersed-boundary reconstruction schemes to model the buoyancy flux boundary condition on the surface, establishing a benchmark against a body-fitted approach where the gravity vector was rotated instead to account for the surface inclination. The simulations were carried out for both laminar and turbulent regimes, and while all the immersed-boundary schemes agreed with Prandtl's solution for the laminar case, differences increased for some of these schemes when compared against the body-fitted approach for turbulent simulations. Due to these differences the authors identified one of the assessed reconstruction schemes as the most optimal one, for which the first- and second-order turbulence statistics had the best agreement with respect to the body-fitted solution despite not showing any improvement over this direct approach. These contributions resulted in a validated DNS code that was then used by Xiao and Senocak to verify the organized vortical structures predicted by the Linear Stability Analysis [33, 22, 34] through slope flow simulations in the unstable laminar regime, as dictated by the recently introduced instability maps. The presence of the instabilities was confirmed for the stationary longitudinal, traveling wave, and mixed types of rolls, while also highlighting large structural differences between anabatic and katabatic flow scenarios for the same set of slope flow parameters only differing in the sign of the buoyancy flux at the surface. Therefore, this validated DNS code provides a powerful tool to survey the proposed instability maps and further explore the underlying relationship between the instability modes and the slope flow parameters.

1.2 Thesis Statement

This thesis explores the dynamics of the longitudinal and traveling wave instability rolls emerging in the unstable laminar regime of katabatic flows, which have been proven analytically and whose signature has been traced in experimental and numerical studies. To advance the current understanding of these organized vortical structures, the presented research leverages direct numerical simulations and establishes predictive relationships for the behavior of the temporal and spatial oscillations observed in such slope flows as functions of relevant dimensionless flow parameters.

2.0 Technical Background

This chapter presents the governing equations for slope flows, along with their analytical solution under an idealized laminar and stationary scenario, known as Prandtl's model for slope flows. An instability map [33] for predicting the type of instabilities emerging in katabatic flows is also presented along with relevant dimensionless parameters and appropriate flow scales. Finally, the key numerical methods and postprocessing tools are discussed.

2.1 Governing Equations

The governing equations for the katabatic slope flow phenomenon come from conservation laws subject to a series of modeling simplifications. The problem is studied using a Cartesian coordinate system $x_i = [x_1, x_2, x_3] = [x, y, z]$ rotated by the slope's inclination angle α , such that the x -direction is aligned with the along-slope direction, the y -direction is aligned with the cross-slope direction, and the z -direction is aligned with the slope-normal direction, as shown in Fig. 1.1. The along-slope and cross-slope directions are alternatively called longitudinal and transverse directions, respectively. The normalized vertical gravity vector expressed in this coordinate system becomes $g_i = [\sin \alpha, 0, \cos \alpha]$. The flow fields to be studied are the velocity vector field $u_i = [u, v, w]$, the pressure scalar field p , and the buoyancy scalar field $b = g(\Theta - \Theta_e)/\Theta_r$, where g is the acceleration of gravity, Θ is the potential temperature, i.e. the temperature a parcel of air will reach if brought adiabatically to a reference pressure, and Θ_e and Θ_r denote the environmental and constant reference potential temperature, respectively. The Boussinesq approximation is employed to model density as a constant except for buoyancy effects, allowing the use of the incompressible version of the continuity equation. The effects of buoyancy are included through buoyancy forcing terms in the Navier-Stokes equations, and Coriolis forces are neglected. The resulting governing equations for conservation of mass, linear momentum, and energy are presented in Eqs. 2.1-2.3, respectively, following the presentation proposed by Fedorovich and Shapiro [3].

$$\frac{\partial u_i}{\partial x_i} = 0, \quad (2.1)$$

$$\frac{\partial u_i}{\partial t} + \frac{\partial u_i u_j}{\partial x_j} = -\frac{1}{\rho} \frac{\partial p}{\partial x_i} + \frac{\partial}{\partial x_j} \left(\nu \frac{\partial u_i}{\partial x_j} \right) + b g_i, \quad (2.2)$$

$$\frac{\partial b}{\partial t} + \frac{\partial b u_j}{\partial x_j} = \frac{\partial}{\partial x_j} \left(\beta \frac{\partial b}{\partial x_j} \right) - N^2 g_j u_j, \quad (2.3)$$

where ν and β denote the momentum and thermal diffusivities of the fluid, respectively, and ρ denotes density. N corresponds to the Brunt-Väisälä frequency, with N^2 being a measure of the stable background stratification in the flow. In the presented katabatic flow model, the vertical gradient of the environmental potential temperature is assumed to be constant, which also implies N to be constant and corresponds to the linear background stratification simplification.

In the prototype slope flow scenario characterized by an infinitely long surface in all directions inclined with a constant slope under a linear and stable background stratification, katabatic conditions are generated by a constant and uniform surface cooling denoted by $B_s < 0$. When considering this prototype flow, the boundary conditions can be represented as follows: At the bottom boundary with height $z = 0$, the no-slip and impermeability conditions are applied to the velocity field, while the buoyancy field is subject to a Neumann boundary condition such that $\partial b / \partial z|_{z=0} = B_s / \beta$; the top boundary is modeled through free-slip and zero normal gradient boundary conditions for velocity and buoyancy, respectively; and the lateral boundaries are modeled through periodic boundary conditions for all fields.

2.2 Prandtl's Laminar Solution

Considering the steady state, laminar, one-dimensional, and slope-parallel idealized slope flow scenario would reduce Eqs. 2.1-2.3 into Eqs. 2.4 and 2.5, corresponding to Prandtl's model for slope flows [3, 29].

$$b \sin \alpha + \nu \frac{\partial^2 u}{\partial z^2} = 0, \quad (2.4)$$

$$-N^2 u \sin \alpha + \beta \frac{\partial^2 b}{\partial z^2}, \quad (2.5)$$

which was originally formulated with a Dirichlet boundary condition applied at the surface for the buoyancy field, prescribing the buoyancy value at $z = 0$. This model was later extended by Fedorovich and Shapiro [3] to consider a Neumann boundary condition instead, thus prescribing the surface buoyancy gradient $\partial b / \partial z|_{z=0}$ based on the surface heat flux B_s that drives the flow. Introducing appropriate flow scales, Eqs. 2.4-2.5 can be normalized and then solved analytically as shown Fedorovich and Shapiro [3], yielding the solutions presented in Eqs. 2.6 and 2.7.

$$u_n = \sqrt{2} \sin(z_n / \sqrt{2}) \exp(-z_n / \sqrt{2}), \quad (2.6)$$

$$b_n = \sqrt{2} \cos(z_n / \sqrt{2}) \exp(-z_n / \sqrt{2}), \quad (2.7)$$

where $z_n = z/l_0$, $u_n = u/u_0$, and $b_n = b/b_0$ correspond to the height above the surface, along-slope velocity and buoyancy, respectively, normalized using the flow scales shown in Eqs. 2.8-2.10.

$$l_0 = (\nu\beta)^{1/4} N^{-1/2} \sin^{-1/2} \alpha, \quad (2.8)$$

$$u_0 = (\nu\beta)^{-1/4} N^{-3/2} B_s \sin^{-1/2} \alpha, \quad (2.9)$$

$$b_0 = \nu^{1/4} \beta^{-3/4} N^{-1/2} B_s \sin^{-1/2} \alpha. \quad (2.10)$$

The maximum jet velocity in Prandtl's laminar solution has a normalized magnitude of $u_{n,\text{jet}} = e^{-\pi/4}$ and occurs at a height $z_{n,\text{jet}} = \pi\sqrt{2}/4 \approx 1.11$. Note that while the proposed length scale in Eq. 2.8 was proposed as a generic scale with no direct association in the flow field [3], the analytical solution revealed that the jet's height is observed at a dimensional

height $z_{\text{jet}} \approx l_0$. The normalized velocity and buoyancy profiles are depicted in Figs. 2.1(a) and (b), respectively, which are valid for both katabatic and anabatic scenarios when the appropriate sign of the surface buoyancy flux is used in the flow scales. Slope flows in nature have been observed to resemble the structure predicted by these analytical profiles with a better agreement for the katabatic scenario, and tuning parameters have been proposed to be included into Prandtl’s model to improve such predictions [26, 30].

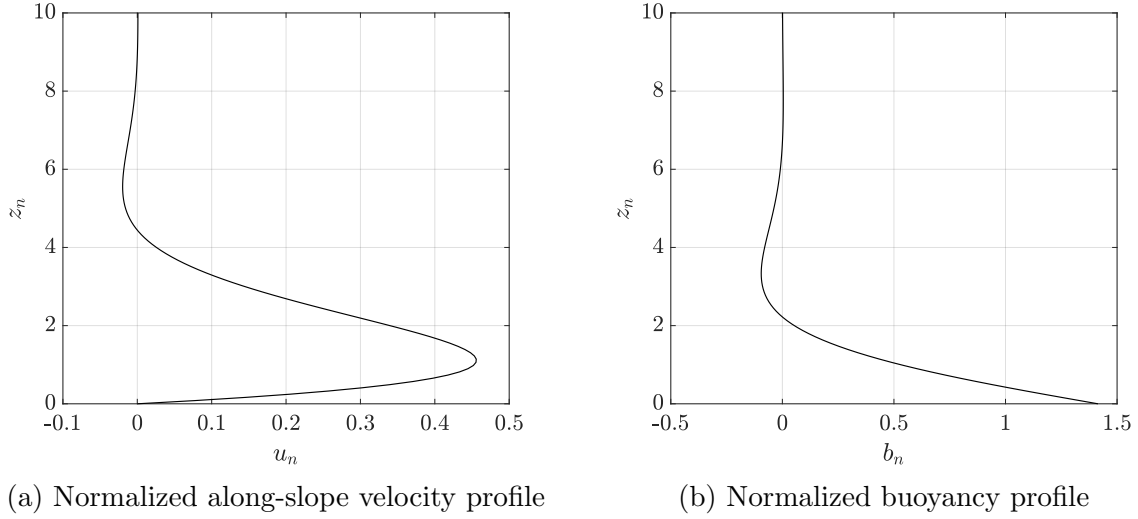


Figure 2.1: Prandtl’s laminar solution

2.3 Relevant Dimensionless Parameters and Flow Scales

Applying the Buckingham π theorem to Prandtl’s idealized slope flows scenario, Xiao and Senocak [33] have showed that there are three dimensionless groups governing the physics of such flows. These parameters are the slope angle α , the Prandtl number $Pr = \nu/\beta$, which compares the momentum and thermal diffusivities of the fluid, and the stratification perturbation parameter Π_s (Eq. 2.11), which is the ratio between the surface buoyancy gradient and a measure of the background stratification. This last parameter represents a new contribution and is interpreted by the authors as a measure of the disturbance to the background stratification by heat conduction at the surface. Slope flows are found

to become dynamically more unstable with increasing Π_s , hence the flow will be closer to turbulence for large Π_s values when the other two parameters are fixed, transitioning through several instability modes along its way. Note that no length or velocity scales appear in such dimensionless parameters as neither is applied externally in the prototype slope flow scenario.

$$\Pi_s = \frac{|B_s|}{\beta N^2} = \frac{|\frac{\partial b}{\partial z}|_{z=0}}{N^2}. \quad (2.11)$$

Based on the dimensionless parameters presented above, the flow scales from Eqs. 2.8-2.10 can be rewritten as:

$$l_0 = \beta^{1/2} N^{-1/2} Pr^{1/4} \sin^{-1/2} \alpha, \quad (2.12)$$

$$u_0 = \beta^{1/2} N^{1/2} Pr^{-1/4} \Pi_s \sin^{-1/2} \alpha, \quad (2.13)$$

$$b_0 = \beta^{1/2} N^{3/2} Pr^{1/4} \Pi_s \sin^{-1/2} \alpha, \quad (2.14)$$

where l_0 is independent of Π_s when β and N are set constant, in contrast to u_0 and b_0 , which show a linear dependency on Π_s . Additional flow scales can be introduced, such as a convective time scale $t_{0,c}$ (Eq. 2.15), a buoyancy frequency scale $f_{0,en}$ (Eq. 2.16) based on the *en masse* oscillations' frequency [31], and a pressure scale p_0 (Eq. 2.17) corresponding to the dynamic pressure.

$$t_{0,c} = l_0/|u_0| = N^{-1} Pr^{1/2} \Pi_s^{-1}, \quad (2.15)$$

$$f_{0,en} = \frac{N \sin \alpha}{2\pi}, \quad (2.16)$$

$$p_0 = \frac{1}{2} \rho u_0^2. \quad (2.17)$$

Hence, a complete set of normalized quantities can be defined to describe the dynamics of slope flows, which will be used to present the results in Chapter 3. Namely, $u_n = u/u_0$, $v_n = v/u_0$, and $w_n = w/u_0$ correspond to the normalized velocity components, while $b_n = b/b_0$ and $p_n = p/p_0$ are the normalized buoyancy and pressure fields, respectively. The normalized time $t_n = t/t_{0,c}$ and normalized frequency $f_n = f/f_{0,en}$ help describe oscillating dynamics in time, while the normalized along-slope λ_x/l_0 and cross-slope λ_y/l_0 wavelengths help describe oscillations in the spatial domain.

Note that the frequency scale $f_{0,\text{en}}$ presented in Eq. 2.16 does not correspond to the reciprocal of the convective time scale $t_{0,c}$ presented in Eq. 2.15. Such a frequency scale was chosen to directly compare the observed frequencies with respect to the *en masse* oscillations' frequency. When the convective time scale $t_{0,c}$ is used to normalize the proposed frequency scale, the relationship presented in Eq. 2.18 is obtained, which becomes the dimensionless *en masse* oscillations' frequency.

$$f_0 t_0 = \frac{N \sin \alpha}{2\pi} t_0 = \frac{Pr^{1/2} \Pi_s^{-1} \sin \alpha}{2\pi} \quad (2.18)$$

Additionally, for the katabatic flow scenario with ambient wind aloft U_∞ , the wind forcing number Π_w is introduced by Xiao and Senocak [34] as the ratio between the kinetic energy in the ambient wind and the damping of kinetic energy due to both viscous forces and the stabilizing effect of the stratified atmosphere.

$$\Pi_w = \frac{U_\infty^2}{\nu N}. \quad (2.19)$$

2.4 Instability Map

Linear Stability Analysis has enabled the study of the propagation of infinitesimal disturbances on Prandtl's laminar solution for slope flows, revealing the emergence of three types of instabilities as shown by Xiao and Senocak for multiple slope flow scenarios considering katabatic flows with and without ambient winds aloft and anabatic flows [4, 33, 22, 34]. Such instabilities are defined by the propagation of wave-like unstable modes along either the longitudinal or transverse directions, which results in the longitudinal and transverse modes of instability, respectively. Additionally, these instabilities can coexist in the flow in a regime denoted as mixed/higher order instabilities. Their contributions for the katabatic flow scenario are summarized through the instability map presented in Fig. 2.2, which parameterizes the emergence of the instability modes as a function of the three dimensionless parameters governing the slope flows dynamics as presented in section 2.3. The absence of

instabilities is known as a linearly stable regime, for which the Prandtl’s laminar solution holds, being stable with respect to small perturbations.

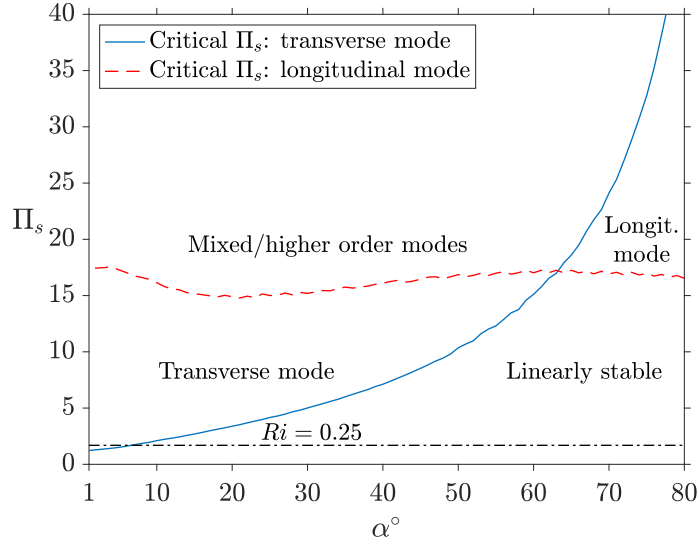


Figure 2.2: $\Pi_s - \alpha$ Instability map for katabatic flows at $Pr = 0.71$. The region above the horizontal line denotes $Ri < 0.25$. Reproduced from [33]

Validating the presence of these instabilities through computer simulations, Xiao and Senocak [33] observed how each type of instability manifests as organized vortical structures that are aligned with a corresponding flow direction and that either travel or remain stationary. Such vortical structures are also known as instability or vortex rolls. The transverse mode exhibits longitudinal instability rolls that are aligned with the along-slope direction—equivalently the base-flow direction—and that remain stationary. The longitudinal modes, on the other hand, exhibit vortex rolls that are aligned with the cross-slope direction and that travel along slope direction, thus defining a traveling wave instability. These traveling wave rolls have been regarded as a generalized Kelvin-Helmholtz type of instability while the longitudinal rolls characterizing the transverse mode of instability resemble Görtler or Taylor-Couette vortices. [22]. In the mixed mode regime, both the longitudinal and traveling wave rolls are present, forming complex interwoven structures that can fall either on a weakly-mixed condition with one of them being stronger and trying to overcome the other one, or a well-mixed condition, where both of them have comparable strength.

A milestone in the study of the propagation of instabilities in inviscid unbounded stratified flows is the Miles-Howard theorem [37], which proposes a criterion for the presence of instabilities in such flows. This criterion establishes a threshold based on the gradient Richardson number $Ri = Pr/\Pi_s^2$, such that the flow will remain stable as long as $Ri > 0.25$. From this formulation, having $Ri < 0.25$ would be a necessary but not sufficient condition for instability [38]. However, extending such a criterion to katabatic flows reveals different instability thresholds, as seen in Fig. 2.2. Firstly, katabatic flows exhibit the transverse mode of instability for shallow slopes $\alpha < 5^\circ$ and Π_s values such that $Ri > 0.25$, thus contradicting the first part of the criterion. Secondly, stability is observed for steep slopes and Π_s values such that Ri is as low as 2×10^{-3} . Therefore, Xiao and Senocak [33] concluded that a criterion based on the gradient Richardson number alone is not enough for describing the instability regions of katabatic slope flows. Note that this conclusion does not question the validity of the Miles-Howard theorem for the idealization it is originally based upon. Issues arise when this criterion is extended to different flow configurations that were not considered at the time the theorem was formulated, being the katabatic flow scenario one particular example of those.

2.5 Direct Numerical Simulations

Direct numerical simulations (DNS), on which the governing equations presented Eqs. 2.1-2.3 are integrated numerically resolving all scales of motion, were carried out adopting the GIN3D flow solver [39]. This code leverages efficient computations on graphical processing units (GPUs) and features a Cartesian mesh three-dimensional solver that has been validated for katabatic slope flow simulations through a body-fitted representation of the inclined surface, on which the coordinate system is rotated to account for the slope angle [36]. This is the same solver used by Xiao and Senocak [4, 33, 22, 34] to validate the presence of the instability rolls on multiple slope flow configurations. The code exhibits a global second order of accuracy through second-order accurate central difference discretization scheme in space and second-order accurate Adams-Bashfort discretization scheme in time. The pressure field is solved through the Poisson equation using a geometric multigrid technique [39].

The simulation domain, representing the prototype slope flow scenario, consisted of a rectangular box with size $L_x \times L_y \times L_z$. The choice of the domain size was such that the top boundary was placed at $L_z = 50l_0$, with l_0 being the length scale introduced in Eq. 2.12. The longitudinal and transverse directions were chosen as a function of the separation observed among the instability rolls, with a base case of $L_x = L_y = 200l_0$ that was modified along each direction separately as needed in order to capture several of the dominant instability rolls. The mesh resolution was chosen such that there were at least two points per length scale, maintaining an equal resolution along the x and y directions and making the resolution along the z direction twice as fine. The temporal discretization was chosen through the Courant-Fiedrichs-Lewis stability condition $CFL = u_{\max}\Delta t/\Delta x$ such that $CFL \leq 0.4$ for all the assessed mesh resolutions.

The boundary conditions for representing the prototype slope flow scenario were implemented matching the boundary conditions listed in section 2.1, and the initial condition was defined as Prandtl's laminar solution for the base case, with an alternate scenario considered for the flow starting from rest through a zero-field initial condition. The fluid properties corresponded to a reference density $\rho = 1 \text{ kg m}^{-3}$, a fixed Prandtl number of $Pr = \nu/\beta = 0.71$, with $\nu = 5 \times 10^{-4} \text{ m}^2 \text{ s}^{-1}$ and $\beta = 7.04 \times 10^{-4} \text{ m}^2 \text{ s}^{-1}$. The stratification of the atmo-

sphere above the surface was defined through a Brunt-Väisälä frequency value of $N = 1 \text{ s}^{-1}$. Keeping all the fluid properties constant, the Π_s number for each simulation was modified changing the surface buoyancy gradient $\partial b/\partial z|_{z=0}$ only. No external disturbances were required for triggering the instabilities in the flow, which are predicted by linear stability based on infinitesimal perturbations. Roundoff errors from the iterative numerical computations and discretization errors were sufficient for those instabilities to emerge after the simulated time covered numerous time scales [4].

2.6 Data Analysis in the Frequency and Wavelength Domains

Let $a_n = a(t)/a_0$ be a normalized signal which is a function of time $t = t/t_n$ and is sampled at a set of N_s discrete points with a frequency F_s . The Discrete Fourier Transform (DFT) of this signal, presented in Eq. 2.20, approximates the continuous Fourier Transform and reveals its frequency components, thus shifting the analysis domain from the temporal domain to the frequency domain. An equivalent domain translation is achieved from signals in the spatial domain to the wavenumber domain, or equivalently the wavelength domain [40, 41].

$$\hat{a}_k = \sum_{j=0}^{N_s-1} a_j e^{i2\pi jk/N_s}, \quad k = 0, 1, \dots, N_s - 1, \quad (2.20)$$

where i represents the imaginary unit and $\hat{a}_n = \hat{a}_k/a_0$ is the normalized amplitude corresponding to the frequency $f_k = kF_s/N_s$, which can be normalized with any relevant frequency scale.

The Fast Fourier Transform (FFT) is an efficient algorithm for computing the DFT of a given signal, with improved computational performance when N_s is a power of two [40, 41]. The FFT package available in Matlab is used in this thesis to compute the frequency and wavelength components of the multiple temporal and spatial signals to be analyzed. A sample script showing the use of FFT for the present flow problem is presented in Appendix A, which reflects the considerations listed below [40, 41]:

- The mean value is subtracted from the signals and a Hann window is applied before computing the FFT, which reduces spectral leakage errors when identifying the dominant frequencies among a set of discrete frequencies [41]. Applying such a window requires scaling the FFT output using a factor of 2.02 as presented by Harris [42].
- The signals are padded with trailing zeros at the end to bring the signal's length to the closest power of two such that the performance of the FFT is improved. No error is induced from such a change.
- The FFT amplitude \hat{a}_k for real signals exhibits both real and imaginary components and is symmetrical with respect to the Nyquist (folding) frequency $F_s/2$, and the sampling frequency F_s itself needs to be at least twice the largest frequency to be captured in the signal to satisfy the sampling theorem, also known as the Nyquist criterion [41]. Hence, only one half of the FFT spectrum is shown being multiplied by a factor of 2, which results in resolving for any frequency component f_i such that $f_i < F_s/2$.
- The FFT results are normalized using the original signal's length and the FFT amplitude is presented through the Power Spectral Density (PSD) estimate shown in Eq. 2.21.

$$S(a_k) = \frac{1}{F_s N_s} |\hat{a}_k|^2, \quad k = 0, 1, \dots, N_s - 1, \quad (2.21)$$

where $|\hat{a}_k|$ denotes the complex magnitude. The units of $S(a_k)$ are square units of a_k per unit frequency, thus requiring appropriate normalization for both temporal and spatial signals.

- The wavelength domain λ is defined as the reciprocal of the wavenumber domain k , such that $\lambda = 2\pi/k$. Wavelength domains are defined for each direction, with λ_x and λ_y corresponding to the x and y directions, respectively.
- The resolvability of the FFT in the frequency domain is defined by integer multiples of $F_s/N_s = 1/(\Delta t_s N_s) = 1/T$ where Δt_s is the sampling period and T is the total sampled time when considering temporal signals. Equivalently, for spatial signals, the resolvability of the FFT in the wavelength domain is defined by integer fractions of $1/(F_s/N_s) = \Delta x N_s = L_x$ where Δx is the distance between two consecutive samples and L_x is the total sampled length.

- Averaging is performed among multiple FFT results for spatial signals collected at multiple domain locations and several time snapshots to identify the mean most dominant wavelengths.
- The Short-time Fourier Transform (STFT) was implemented as a windowed approach to determine the change in both amplitude and frequency of signals over time. This technique slides a window through the signal and makes every value outside the window to become zero. The discrete formulation of this technique is shown in Eq. 2.22, where w denotes the window with fixed length and m is the index of the window, for a total of N_m windows that are centered at different samples. Note that this technique required to discretize both the temporal and frequency domains, and it is equivalent to splitting up the signal into multiple overlapping segments (windows) whose initial time differs by a fixed offset. Then the Fourier transform (Eq. 2.20) is applied to each one of windows and the resulting frequency spectra are now a function of time [40].

$$\hat{a}_{k,m} = \sum_{j=0}^{N_s-1} w_m (a_j e^{i2\pi jk/N_s}), \quad k = 0, 1, \dots, N_s - 1, \quad m = 0, 1, \dots, N_m - 1. \quad (2.22)$$

Examples of such an FFT implementation are presented below for sample signals both in the temporal and spatial domains. Figure 2.3(a) shows a noisy signal that is known to be the superposition of two sinusoidal waves, with one of them having twice the frequency and twice the amplitude of the other one, as seen in Eq 2.23. Such frequency components which becomes clear from analyzing the normalized FFT amplitudes and normalized dominant frequencies observed in Fig. 2.3(b). Note that the random noise added to the signal did not affect the FFT results. Figure 2.4(a), on the other hand, shows the spatial signal with normalized wavelength equal to 1 presented in Eq. 2.24. This wavelength can be measured directly as the distance between two peaks in the spatial domain and also observed from the most dominant wavelength identified in Figure 2.4(b), which corresponds to a single peak happening at $\lambda_x/l_0 = 1$.

$$a_{n,\text{time}} = \frac{a(t)}{a_0} = \sin(2\pi f_0 t) + 2 \sin(4\pi f_0 t) + \text{random noise} \quad (2.23)$$

$$a_{n,\text{space}} = \frac{a(x)}{a_0} = \cos\left(\frac{2\pi x}{l_0}\right) \quad (2.24)$$

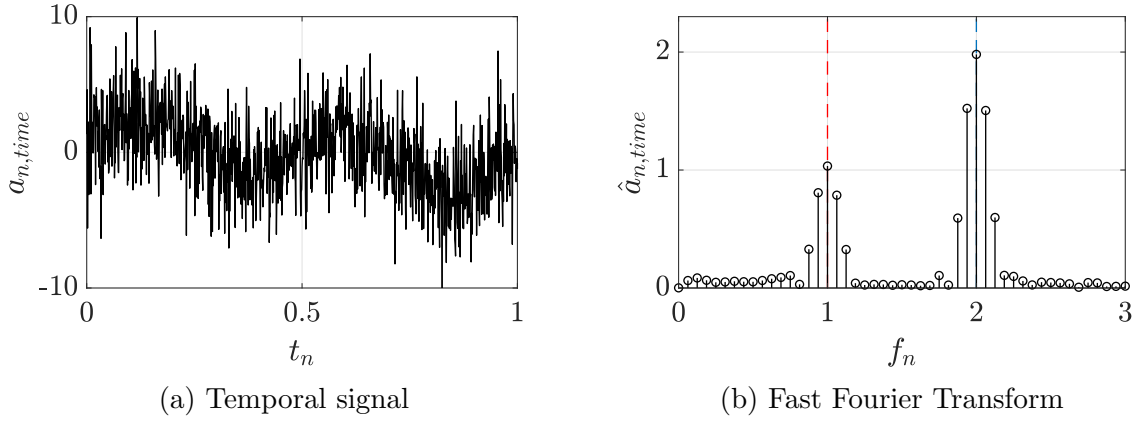


Figure 2.3: Analyzing a temporal signal in the frequency domain. Vertical axes normalized with a_0 , while $t_n = tf_0$ and $f_n = f/f_0$, where a_0 and f_0 are the characteristic amplitude and frequency of the signal in Eq. 2.23, respectively. Red and blue dashed lines correspond to the frequencies f_0 and $2f_0$, respectively.

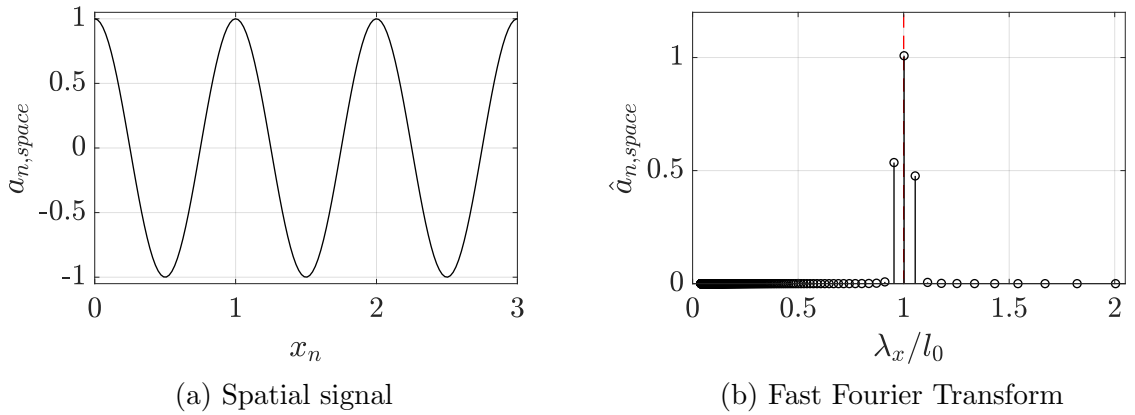


Figure 2.4: Analyzing a spatial signal in the wavelength domain. Vertical axes normalized with a_0 , while $x_n = x/l_0$, where a_0 and l_0 are the characteristic amplitude and wavelength of the signal in Eq. 2.24, respectively. λ_x denotes the wavelength along the x -direction. Red dashed line corresponds to the characteristic wavelength l_0 .

2.7 Reduced-Order Model Formulation

Reduced-order models (ROMs) are a powerful tool for exploiting the low dimensionality of complex systems, reducing them into more tractable forms while still capturing most of the relevant physics involved [43]. ROMs can be built based on either a set of governing equations describing the dynamics of the system or measurements from the system alone, which can come from experiments or computer simulations. These data-driven ROMs are especially powerful for analyzing scenarios where the governing equations are beyond their range of validity and even when such equations are unknown for a given system [43]. The Dynamic Mode Decomposition (DMD) is one example of these equation-free techniques that seeks to identify the spatio-temporal structures present in high-dimensional data captured from a complex system [40] that carry most of the information contained in the data set. This method was proposed by Schmid [44] as a tool for studying fluid flows, yet its applications have extended to a wider spectrum of fields including, among others, biological systems, video processing, and robotics [40, 45].

One of the main advantages of DMD is that, while no equations are needed, the method provides a simple and efficient algorithm to decompose the collected snapshot from a given system into a set of dynamic modes that evolve linearly in time with a given frequency and growth or decay rate [40, 46, 47]. Hence, while DMD relies on a linear formulation, it is still capable of representing nonlinear dynamical systems through an algorithm that identifies the best-fit linear dynamical system that advances the system's snapshots forward in time [40]. Such a linear dynamical system is represented by the linear operator \mathbf{A} that relates two states of the system $\vec{x}_k = \vec{x}(t_k)$ and $\vec{x}_{k+1} = \vec{x}(t_{k+1})$ through:

$$\vec{x}_{k+1} = \mathbf{A}\vec{x}_k, \tag{2.25}$$

where $t_{k+1} = t_k + \Delta t$, with Δt being the temporal spacing between snapshots, and \vec{x} being a one-dimensional column vector containing all the information of the system for a given snapshot in time with size N . Then, \mathbf{A} is defined such that the error between the actual

system state and the linear approximation is minimized for all collected snapshots M , as seen in Eq. 2.26 [40].

$$\mathbf{A} = \operatorname{argmin} \|\vec{x}_{k+1} - \mathbf{A}\vec{x}_k\|, \quad k = 1, 2, \dots, M - 1. \quad (2.26)$$

Although an exact formulation of the optimization problem presented in Eq. 2.26 is available in terms of the Moore–Penrose pseudoinverse [46], solving for \mathbf{A} directly is not computationally efficient since it has size $N \times N$ and $N \gg M$, such that the dimension of the system is much larger than the number of snapshots collected. However, the DMD algorithm provides an efficient approach to approximate the eigenvectors of \mathbf{A} , known as DMD modes $\vec{\phi}$, and their corresponding eigenvalues λ without computing the full matrix \mathbf{A} . Such an approach is based on computing a reduced matrix $\tilde{\mathbf{A}}$ that is based on the singular value decomposition (SVD) of the collected snapshots from the system [40]. This reduced matrix is of size $r \times r$, where $r < M$ corresponds to the reduction size and defines the number of DMD modes to be constructed. Each DMD eigenvalue is defined as $\lambda = a + ib$, where a defines the growth or decay rate of its corresponding DMD mode and b defines its frequency. Lastly, the time evolution of system state based on the DMD modes is defined by [40, 46]:

$$\vec{x}(t) = \sum_{j=1}^r \vec{\phi}_j \exp(\omega_j t) b_j, \quad (2.27)$$

where $\omega_j = \log(\lambda_j)/\Delta t$ and b_j corresponds to the coefficients for writing the system’s initial condition as a linear combination of the DMD modes, such that $\vec{x}_1 = \Phi \vec{b}$, with Φ being the matrix formed by the DMD modes as columns. Note that Eq. 2.27 is, in theory, valid for any time t , even if it is beyond the time period on which the snapshots were collected. Hence, the DMD model in Eq. 2.27 can also be used to both interpolate the state of the system between snapshots and to predict its future state. Yet, since a linear dynamical model is being used to predict the evolution in time of a nonlinear dynamical system, the accuracy of such a prediction is expected to decrease rapidly for future times.

The algorithm for implementing the DMD based on a given data set is introduced in [40, 43, 46], and a custom implementation of it is presented in Appendix B. Some important remarks about implementing DMD are outlined below:

- The high-dimensional snapshots collected from the system, which in the current implementation correspond to two-dimensional flow fields, are reshaped into one-dimensional vectors (\vec{x}_k) and then stacked as columns in a matrix \mathbf{X} . This way the rows of \mathbf{X} contain spatial measurements and its columns define separate time snapshots.
- \mathbf{X}_1 contains the time snapshots $1 \leq k \leq M - 1$ and \mathbf{X}_2 contains the time snapshots $2 \leq k \leq M$. Therefore, each separate data set contains $M - 1$ snapshots.
- Identifying the appropriate reduction size is one of the most important steps of DMD, yet it is highly subjective and there are not definite rules [40]. The implemented approach is based on the concept of the *energy* contained in the SVD modes, which refers to the amount of information that they carry about the data set. The energy of a SVD mode can be measured through the square of its corresponding eigenvalue, and the total energy is measured through the summation of the energy contributions across all eigenvalues [46]. Hence, for a given reduction size r , the amount of energy to be captured in percentage points is:

$$e(r) = \frac{\sum_{i=1}^r \sigma_i^2}{\sum_{i=1}^{M-1} \sigma_i^2} \times 100\%, \quad (2.28)$$

Therefore, the reduction size can be specified either with a target energy content in mind or through the desired number of SVD modes. Note that the choice of r conditions the results of the DMD since the beginning of the algorithms, since r corresponds to the number of SVD modes to preserve from the decomposition of the data set \mathbf{X}_1 , which ultimately defines the number of DMD modes to construct.

- Once all DMD modes have been computed, their relevance in the model can be measured through the real part of their eigenvalues. Then, the DMD modes can be sorted from the most energetic to the least energetic one.
- All DMD eigenvalues need to be at the boundary or within the unit circle in the complex plane, otherwise, the corresponding modes would be unstable and the dynamical system in Eq. 2.27 will eventually blow up.

3.0 Results

This chapter presents the simulation results, starting with a thorough presentation of the instability modes and corresponding vorticity rolls before further exploring their oscillation dynamics. Considerations about the way results are presented include the full simulation domain being shown in all the figures and flow quantities being always normalized using the appropriate scales presented in section 2.3. Unless specified, all results were extracted at the location of the jet's maximum velocity as predicted by Prandtl's laminar solution $z_{n,\text{jet}} = \pi\sqrt{2}/4$. Averaging of the results was performed at later stages of the simulation only.

3.1 Instability Modes

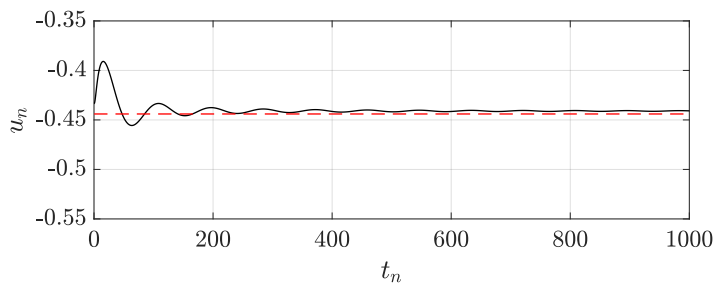
The first step into the analysis of the organized vortical structures observed in katabatic slope flows is to present each one of them separately. Based on the computer simulations carried out according to the parameters outlined in section 2.5 and using the instability map presented in Fig. 2.2 as a guide to navigate the parameter space of katabatic flows, three base cases were chosen to illustrate the presence of the instabilities and discuss their main characteristics, namely a transverse-mode case defined by $\alpha = 20^\circ, \Pi_s = 4$, a longitudinal-mode case defined by $\alpha = 80^\circ, \Pi_s = 20$, and a mixed-mode case defined by $\alpha = 60^\circ, \Pi_s = 30$. The Prandtl number was set constant to $Pr = 0.71$ for all the simulations to be presented.

The first insight about the presence of these instabilities is observed through temporal signals captured at any point in the domain for any of the flow fields. The chosen point P for the current study corresponds to the center point of the domain slice parallel to the xy plane such that $P = (0.5L_x, 0.5L_y, z_{n,\text{jet}})$. The signals collected for the three analysis base cases are presented in Figs. 3.1-3.3. The signals are presented in three different temporal windows, where each window represents a different regime that are common for all the analyzed slope flow scenarios.

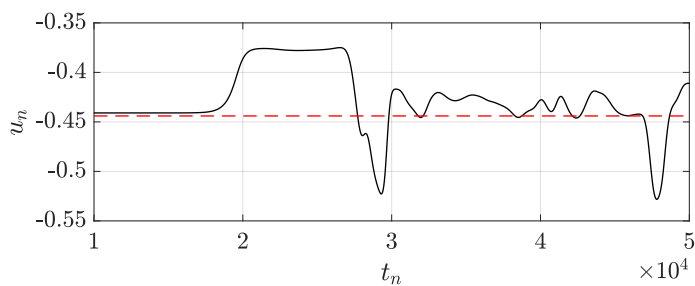
Firstly, with an starting flow field defined by Prandtl’s laminar solution everywhere, the signals exhibit an initial oscillatory regime with constant frequency and damped amplitude. Comparison of subfigure (a) in Figs. 3.1-3.3 reveal how the period of these oscillations changes in the normalized time domain among the base cases with smaller changes in their initial amplitude and mean value. The frequency of such oscillations matches the *en masse* oscillations frequency presented in Eq. 2.16, and their dynamics are discussed in section 3.2. Note that the flow remains stable during this regime despite the oscillations.

After sufficiently long simulated times, a transition regime toward instability happens for each of the base cases. This regime precedes the emergence of well-defined instabilities that are known to be different for each case as predicted by the instability map, and as such each transition regime exhibits different characteristics, as observed from subfigure (b) in Figs. 3.1-3.3. Although the transition happens at different times for each of the base cases, this time doesn’t carry any physical significance, since it only represents the saturation point triggering the instabilities, which happens as a consequence of the infinitesimal disturbances present in the numerical solution, as discussed in section 2.5.

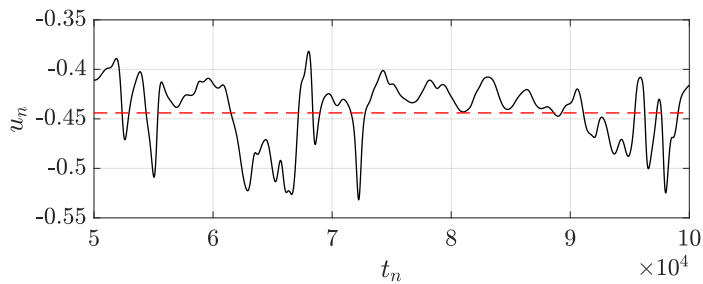
Lastly, the signals reach a quasi-stationary regime where the predicted instability modes develop and persist in the flow. Fig. 3.1(c) reveals how the transverse mode case exhibits irregular and intermittent fluctuations, which are in agreement with the intermittence phenomenon in stratified atmospheric boundary layers described by Mahrt [20]. This signal represents aperiodic motions that can not be characterized in the frequency domain, corresponding to the slow dynamics that characterize the transverse mode of instability and that might require longer simulated times. On the other hand, the longitudinal and mixed modes cases shown in Figs. 3.2(c) and 3.3(c), respectively, exhibit a continuous oscillatory behavior with well-defined frequency components and whose amplitude is not damped in time, thus confirming the presence of the predicted traveling wave rolls.



(a) Initial oscillatory regime

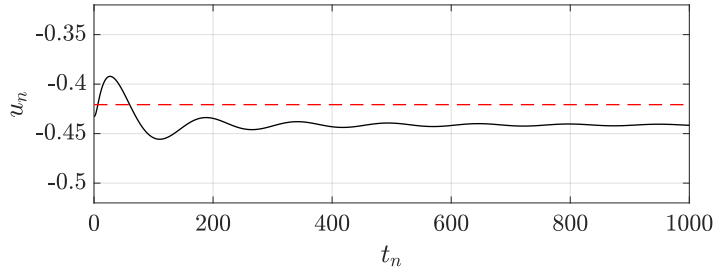


(b) Transition regime

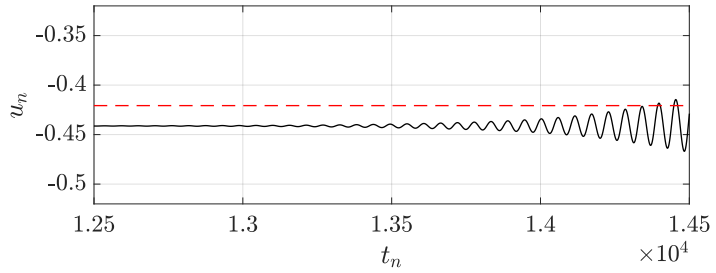


(c) Quasi-stationary regime

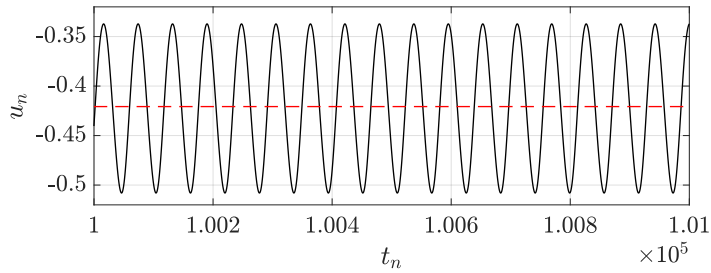
Figure 3.1: Temporal signal breakdown - Longitudinal instability rolls ($\alpha = 20^\circ, \Pi_s = 4$). Red dashed line denotes the mean velocity in the quasi-stationary regime $\bar{u}_n = -0.444$. Horizontal axis normalized using the convective time scale shown in Eq. 2.15



(a) Initial oscillatory regime

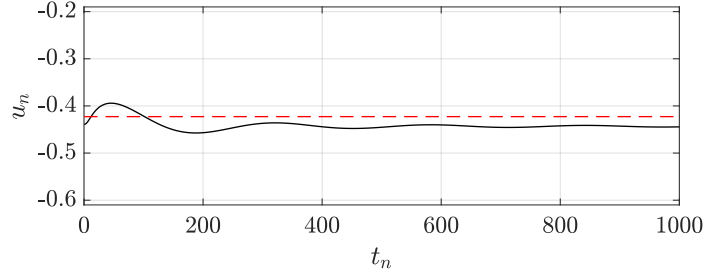


(b) Transition regime

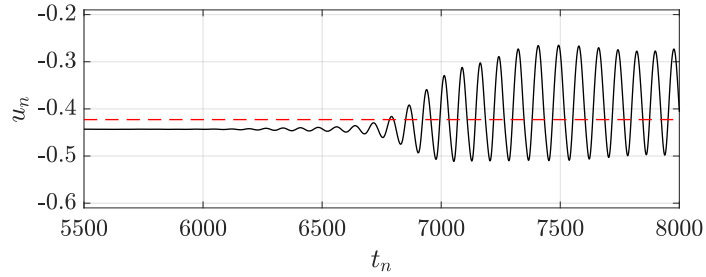


(c) Quasi-stationary regime

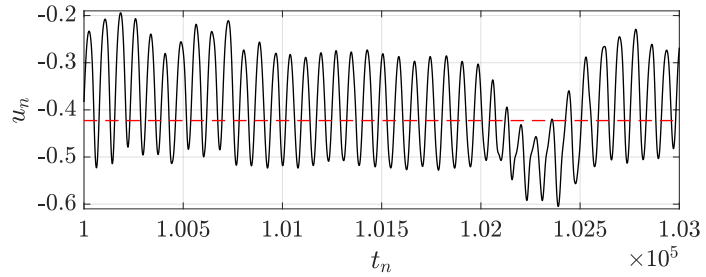
Figure 3.2: Temporal signal breakdown - Traveling wave instability rolls ($\alpha = 80^\circ$, $\Pi_s = 20$). Red dashed line denotes the mean velocity in the quasi-stationary regime $\bar{u}_n = -0.421$. Horizontal axis normalized using the convective time scale shown in Eq. 2.15



(a) Initial oscillatory regime



(b) Transition regime



(c) Quasi-stationary regime

Figure 3.3: Temporal signal breakdown - Mixed instability rolls ($\alpha = 60^\circ, \Pi_s = 30$). Red dashed line denotes the mean velocity in the quasi-stationary regime $\bar{u}_n = -0.423$. Horizontal axis normalized using the convective time scale shown in Eq. 2.15

After confirming the existence of the instabilities in the flow from temporal signals, the shape of the vortical rolls can be examined through detailed flow field visualizations enabled by DNS. Such organized structures are presented in two different ways based on single snapshots of the flow field. Firstly, instantaneous visualizations of isosurfaces of the Q -criterion at 4% of its maximum positive value, as proposed by Hunt et al. [48] for vortex identification, reveal the structure of the instability rolls in a three-dimensional representation. These isosurfaces are colored using the w -velocity component and are shown in Figs. 3.4, 3.6, and 3.8. Secondly, direct visualizations of two-dimensional contour plots of the flow field reveal how these instability rolls manifest differently for each flow field, as shown in Figs. 3.5, 3.7, and 3.9. The height at which the contour plots were plotted corresponded to the jet's height as predicted by Prandtl's laminar solution, which was chosen as a reference location for comparison among all analyzed cases. The observed fluctuations in the v -velocity component were much smaller than for its u and w counterparts, and hence contour plots of the cross-slope velocity component field are not shown.

Longitudinal rolls visualizations, corresponding to the transverse mode of instability, reveal continuous and smooth vortical structures, with a clear separation among them both in the two- and three-dimensional representations. Note that the distance between the rolls and their width is consistent only between the u - and w -velocity component fields and changes for the buoyancy and pressure scalar fields. Additionally, from the linear stability analysis performed by Xiao and Senocak [33], these rolls are predicted to remain stationary, however, in the general case analyzed through DNS, these modes slowly meander along the cross-slope direction.

The traveling wave rolls, corresponding to the longitudinal mode of instability, exhibit a constant separation between the rolls and differences in the phase of the wave-like vortical structures observed among the flow fields. The rolls are completely parallel to the y direction and are observed to move along the base flow direction x as time evolves. Note how the w -velocity component had equal magnitude and opposed sign in the front and trailing edge of three-dimensional vorticity rolls.

The mixed modes regime, characterized by intricate vortical structures from interwoven longitudinal and traveling wave rolls, also exhibits a mostly constant separation among

cross-slope rolls, while an inconsistent behavior is observed for the along-slope rolls, whose presence is not equally strong in all flow fields. Note from Fig. 3.9 how the presence of the longitudinal rolls is almost negligible, but they are significantly more stronger in the u -velocity component field.

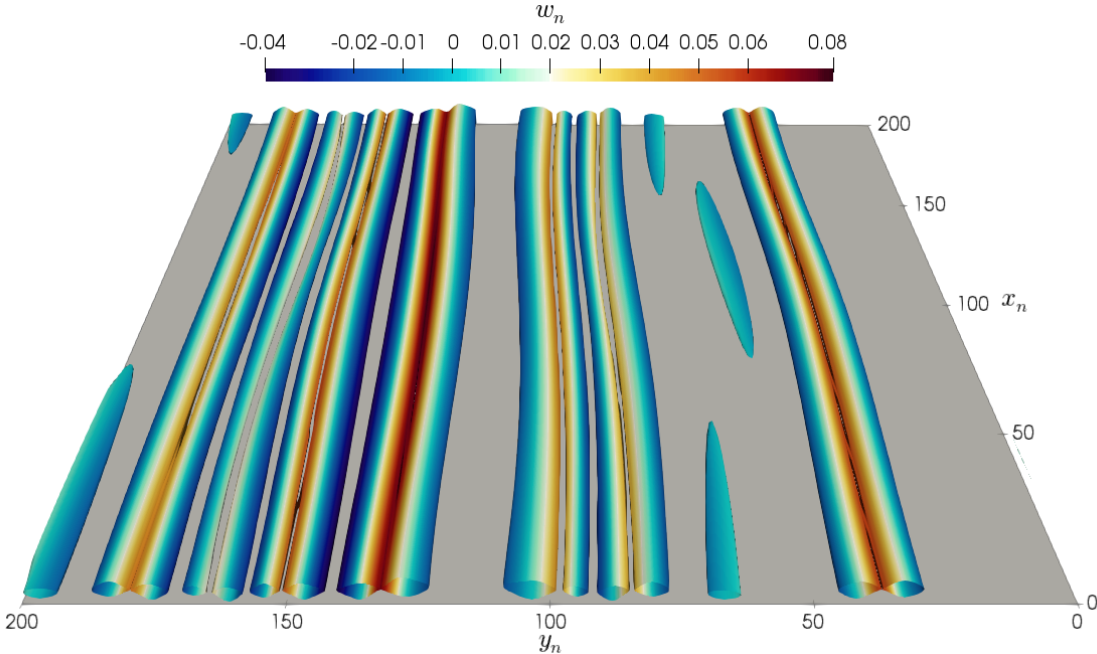


Figure 3.4: Longitudinal vorticity rolls ($\alpha = 20^\circ, \Pi_s = 4$)

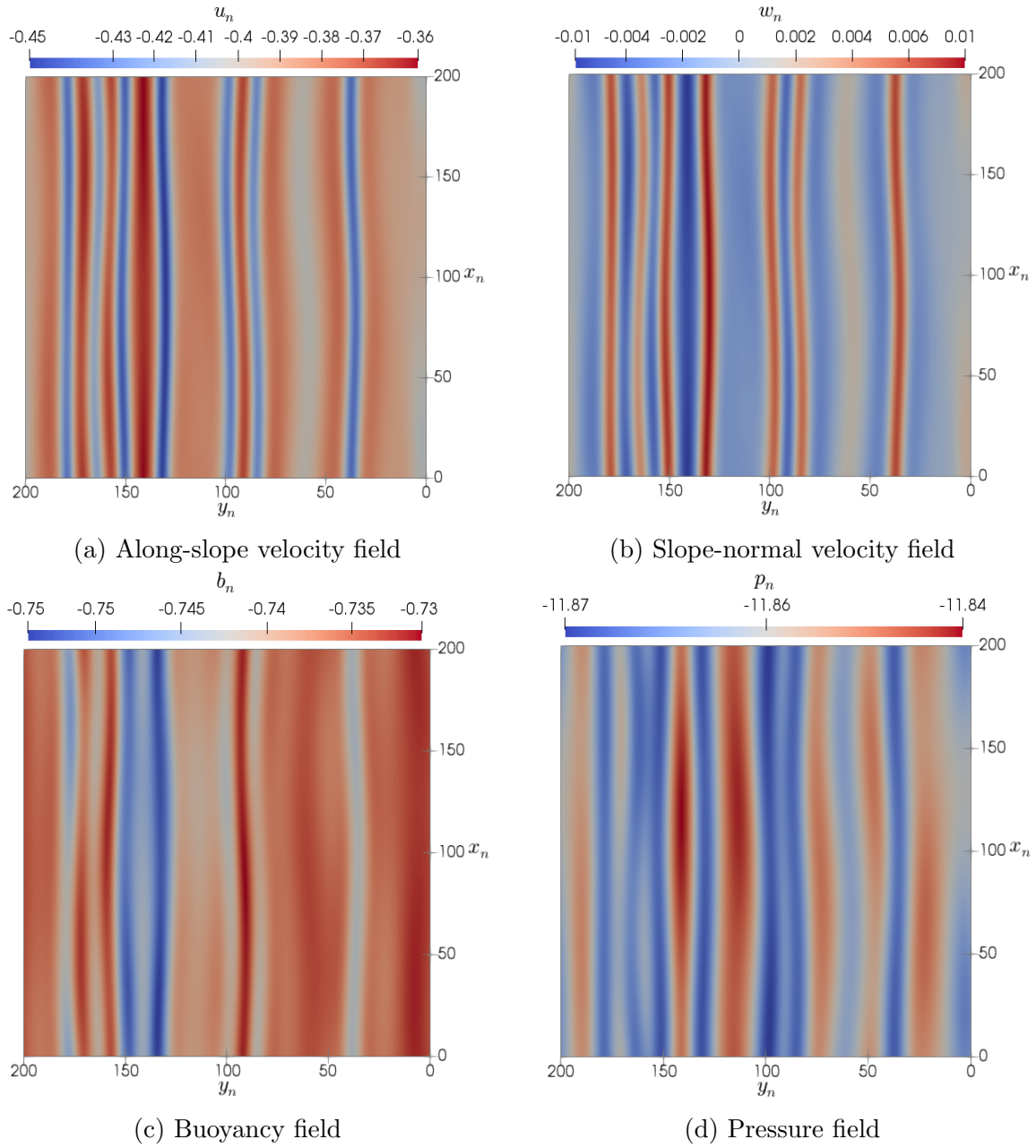


Figure 3.5: Longitudinal rolls in contour plots ($\alpha = 20^\circ$, $\Pi_s = 4$)

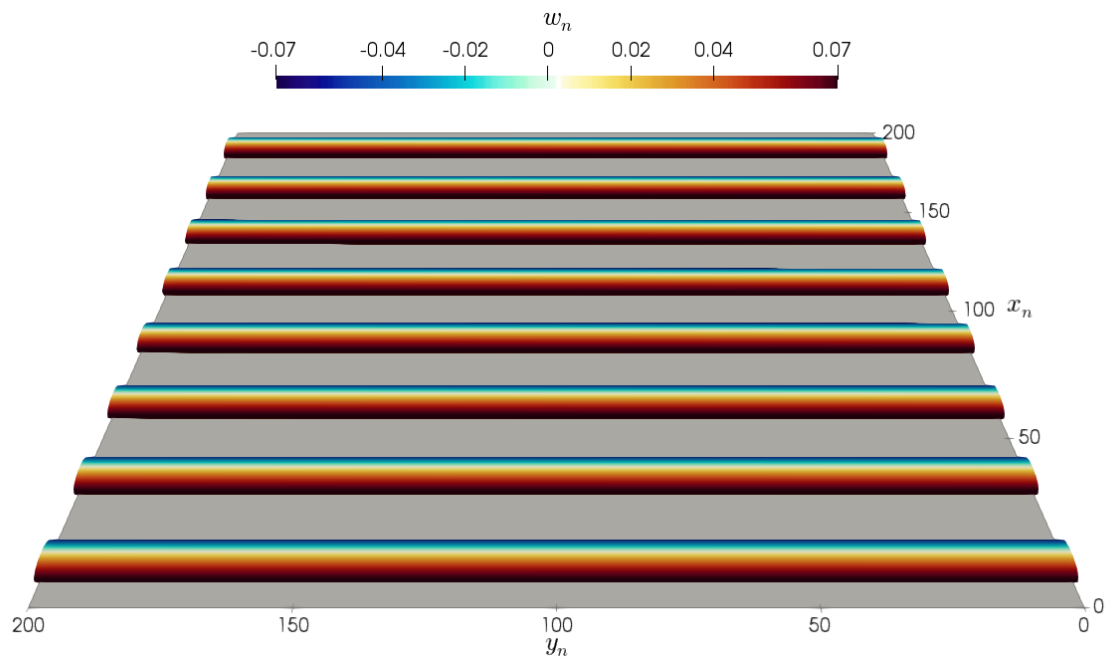


Figure 3.6: Traveling wave vorticity rolls ($\alpha = 80^\circ, \Pi_s = 20$)

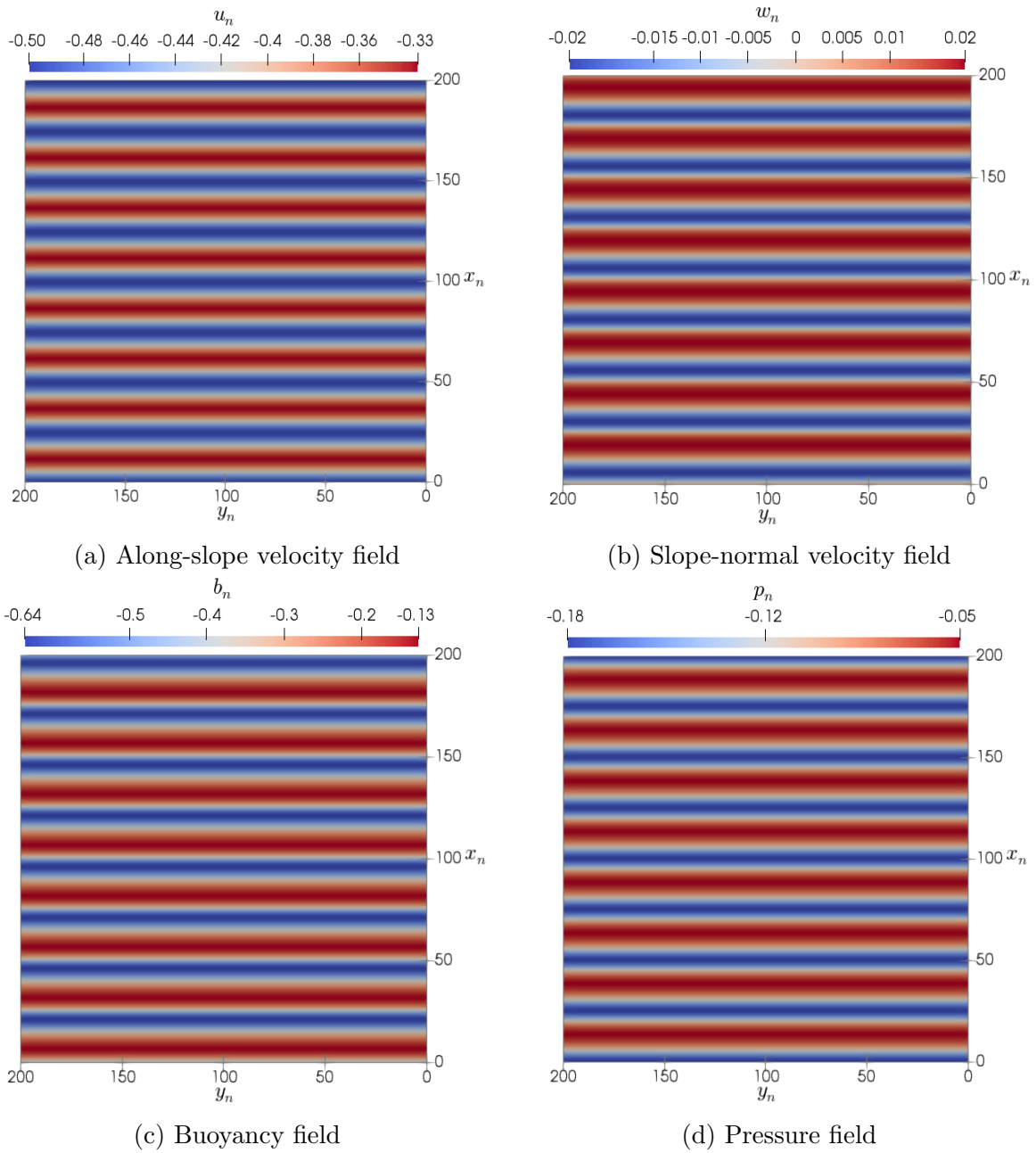


Figure 3.7: Traveling wave rolls in contour plots ($\alpha = 80^\circ$, $\Pi_s = 20$)

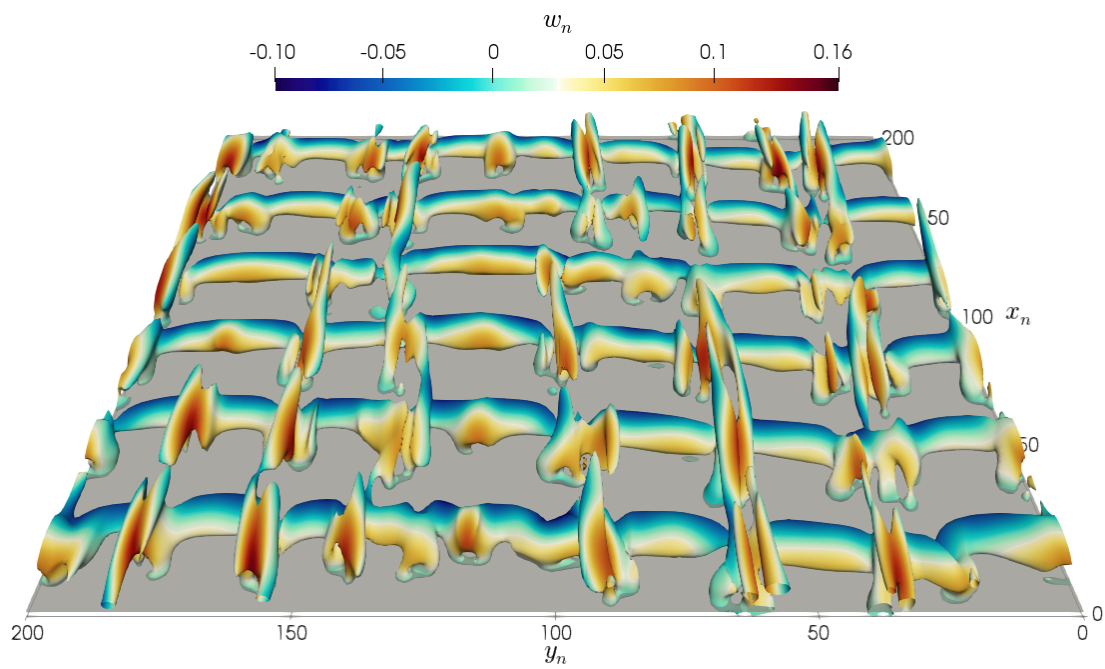


Figure 3.8: Mixed vorticity rolls ($\alpha = 60^\circ$, $\Pi_s = 30$)

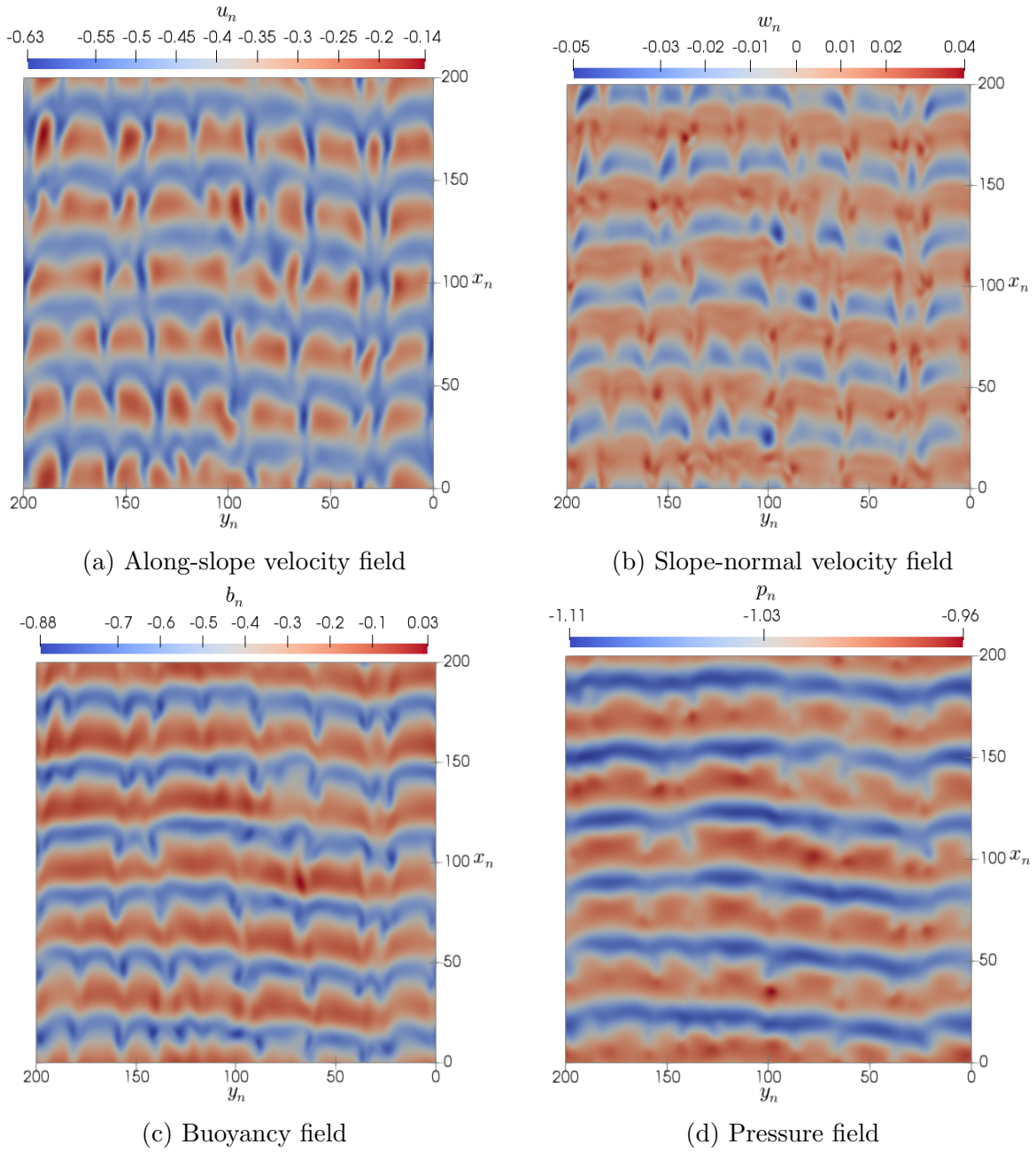


Figure 3.9: Mixed instability rolls in contour plots ($\alpha = 60^\circ, \Pi_s = 30$)

3.2 *En Masse* Oscillations' Dynamics

The frequency component of the signals corresponding to the initial oscillatory adjustment regime for all the three base cases shown in Figs. 3.1-3.3 reveals that the only dominant frequency in each of those signals is equal to the *en masse* frequency presented in Eq. 2.16. Figure 3.10(a), (b), and (c) show the normalized PSD computed from signals sampled in a base temporal window featuring 10 complete periods of such oscillations starting at the normalized time $t_{start}/t_0 = 0$ for the three katabatic base cases presented in section 3.1. Those results in the frequency domain highlight that both the normalized frequency and normalized amplitude of these oscillations remains the same among different slope flow configurations for the analyzed temporal window. However, the amplitude decay *en masse* oscillations changes among the analyzed cases, as revealed by the amplitude decay analysis shown in Fig. 3.10(d).

The amplitude decay was obtained following the STFT technique described in section 2.6, on which the starting time of the base temporal window described above was moved forward with an offset of 1 unit of time while keeping the signal length constant, and then the PSD was computed again for the signal sampled at this new window. The amplitude obtained for the *en masse* frequency was recorded and plotted against the normalized starting time of each window, revealing that for all cases, such oscillations are damped exponentially, with faster amplitude decay observed for lower Π_s values, which feature larger time scales according to Eq. 2.15. Note that the corresponding instabilities were always triggered for each one of the base cases regardless of the amplitude the *en masse* frequency exhibited at the onset of the transition regime.

Such oscillations have also been observed for simulated katabatic flows in turbulent regimes [3, 2], as well as in an idealized transient katabatic flow scenario for which an analytical solution was found [31]. In these studies, however, these oscillations were reported to persist indefinitely in the flow, contrary to the damping behavior that is observed in Figs. 3.1-3.3 and which is confirmed by the analysis presented in Fig. 3.10(d). Note, however, that these analyses have been computed based on temporal signals extracted at the jet's height predicted by Prandtl's laminar solution, and different behaviors have been ob-

served at greater heights away from the surface, as reported in section 3.6, with the *en masse* oscillations persisting at certain heights. Therefore, questions remain about whether these oscillations represent an actual physical phenomenon. To partially address this question, additional simulations were carried out modifying either of the two parameters governing the *en masse* frequency as shown in Eq. 2.16 while keeping the other one constant. The results of this analysis are presented in Fig. 3.11(a) for changing N and in Fig. 3.11(b) for changing α . In all cases the obtained oscillation's frequency coincided with the corresponding *en masse* frequency.

Additionally, to verify whether or not these oscillations corresponded to a numerical artifact, simulations were carried out changing relevant parameters, such as the flow initial condition, the mesh resolution, and the domain size (Fig. 3.12). For all the assessed cases, not only the obtained oscillation's frequency remained constant and equal to the *en masse* frequency, but also the amplitude decay remained unmodified.

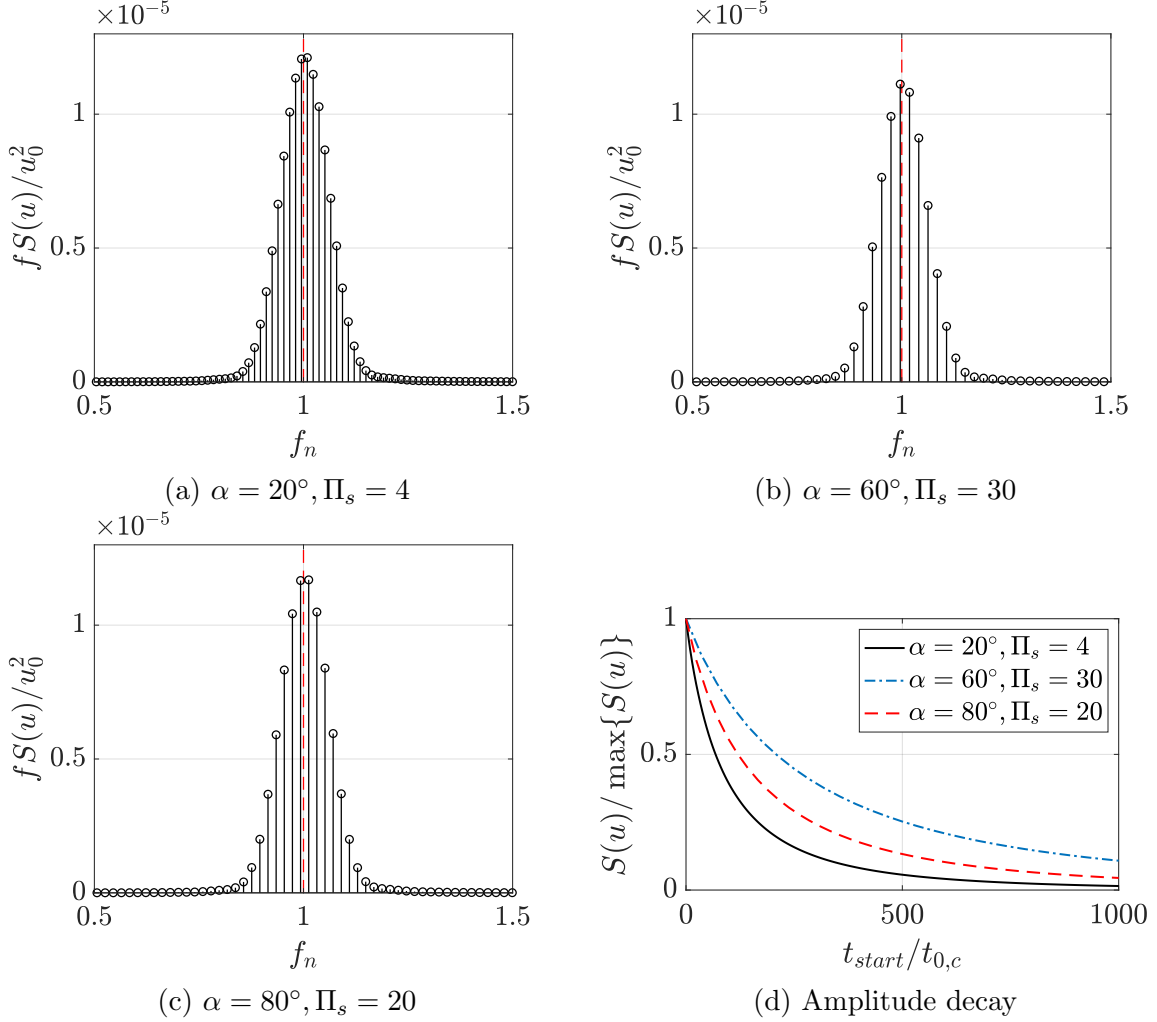


Figure 3.10: *En masse* oscillations dynamics for multiple slope flow parameters computed from the temporal spectra of the u velocity component. Vertical red dashed line denotes the *en masse* frequency in subfigures (a), (b), and (c). Horizontal temporal axis in subfigure (d) normalized using the convective time scale shown in Eq. 2.15

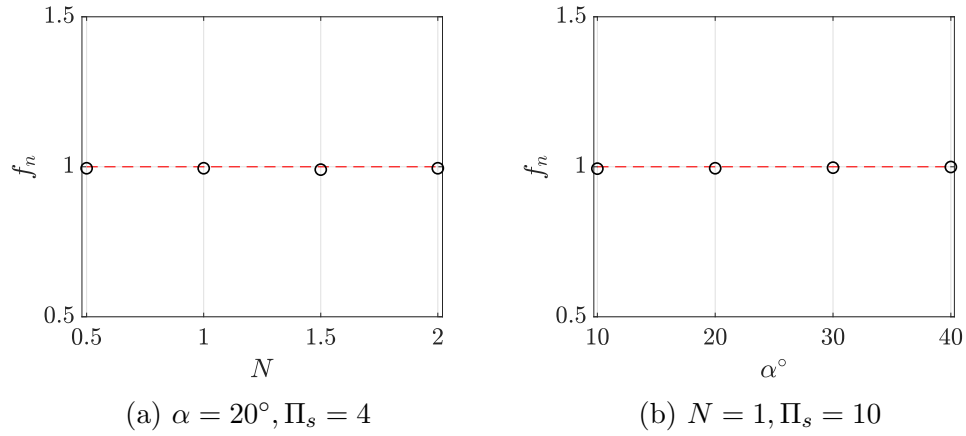


Figure 3.11: Most dominant frequency in the initial oscillatory regime for changing Brunt–Väisälä frequency N and slope α

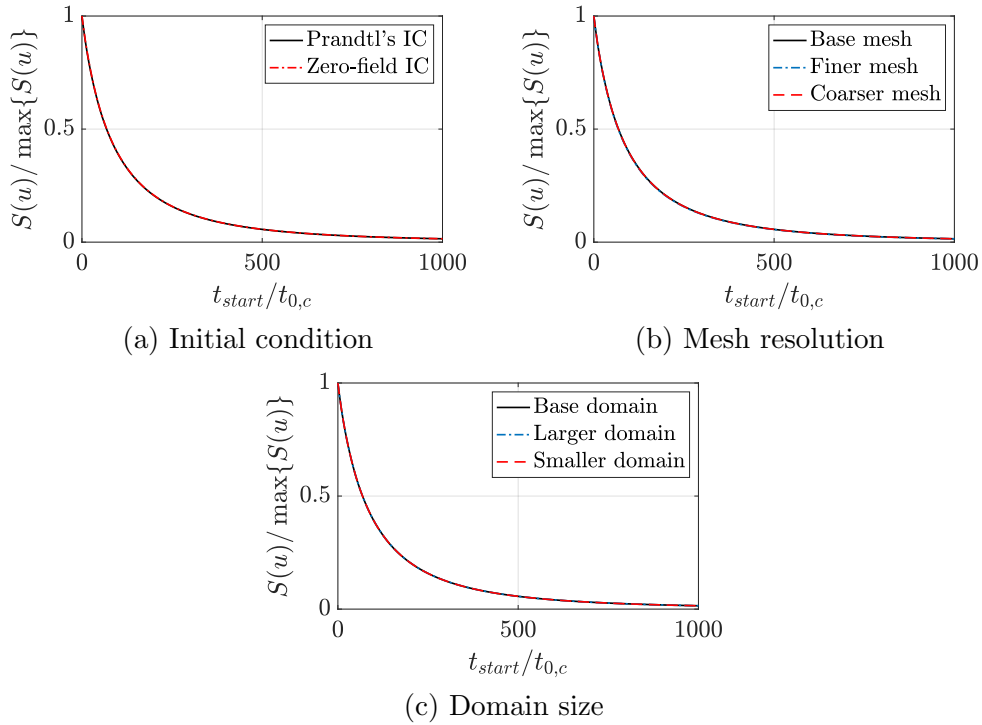


Figure 3.12: Amplitude decay of *en masse* oscillations for multiple simulation parameters ($\alpha = 20^\circ, \Pi_s = 4$). Horizontal temporal axis normalized using the convective time scale shown in Eq. 2.15

3.3 Instability of the Longitudinal Rolls

Longitudinal rolls, while being aligned with the along-slope direction, are not always straight and parallel, as can be observed, for instance, from the slightly curved rolls presented in Fig. 3.5. These disturbed rolls suggest that the instability being observed is also exhibiting an unstable behavior.

Let's consider a different base case defined by $\alpha = 50^\circ$, $\Pi_s = 12$, which corresponds to the transverse mode regime. The contour plot from the normalized u -velocity component field for this case is shown in Fig. 3.13(a), which exhibits continuous and straight longitudinal rolls that are parallel to the along-slope direction. These smooth rolls, however, can be disturbed with increasing Π_s values and without the need of any external perturbation. With a slight increase of the stratification perturbation parameter to $\Pi_s = 13$, Fig. 3.13(b) shows how the instability rolls, while remaining aligned with the along-slope direction, are now curved and have branches, which happens as a result of the rolls colliding with themselves and triggering additional nonlinearities in the flow. These instabilities have now become meandering rolls that exhibit a snaking behavior but remain stationary. These additional dynamics in the longitudinal rolls could be attributed to secondary vortex waves [49].

As Π_s increases, the snaking and meandering dynamics are maintained in the longitudinal rolls, as can be observed in Fig. 3.13(c) and (d) for two additional stratification perturbation parameters. Note, however, that the effect of such nonlinearities was not as drastically intensified by the higher Π_s values as it was when transitioning from the stable condition in Fig. 3.13(a) to the unstable condition in Fig. 3.13(b), thus suggesting the presence of a clear boundary between these two states. Simulations were carried out for multiple slopes to assess the transition toward unstable longitudinal rolls and the results are summarized as a complement to the instability boundaries proposed by Xiao and Senocak [33], and the refined instability map is presented in Fig. 3.14.

For all the cases analyzed above, $L_x = 200l_0$ was set constant, while modifying L_y as needed to include several longitudinal rolls in each of the analyzed flow configurations. However, larger domain sizes along the x direction were also found to destabilize the longitudinal rolls, thus triggering an instability of the primary mode, as seen in Fig. 3.15

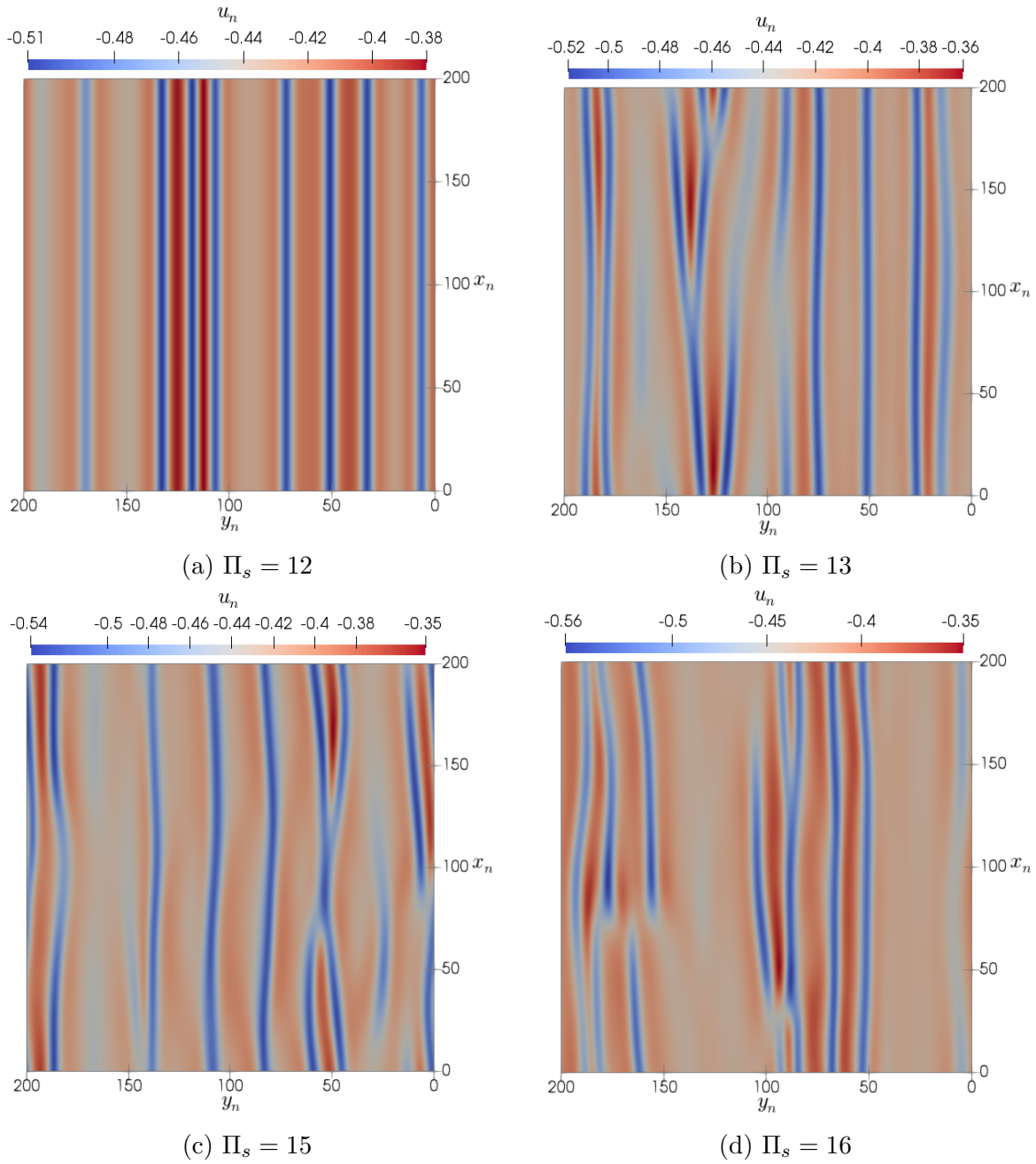


Figure 3.13: Longitudinal rolls disturbance with increasing Π_s for a fixed slope $\alpha = 50^\circ$

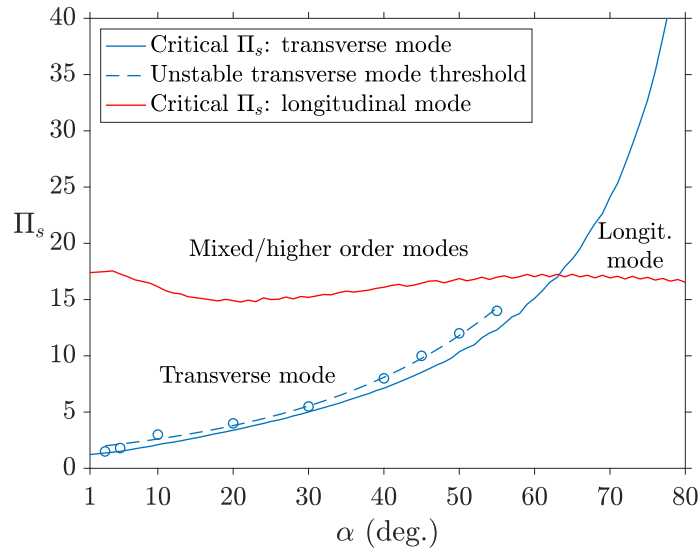


Figure 3.14: Refined instability map. Adapted from [33]. Simulation results are denoted with markers, for which an exponential curve is fitted and shown with a dashed line.

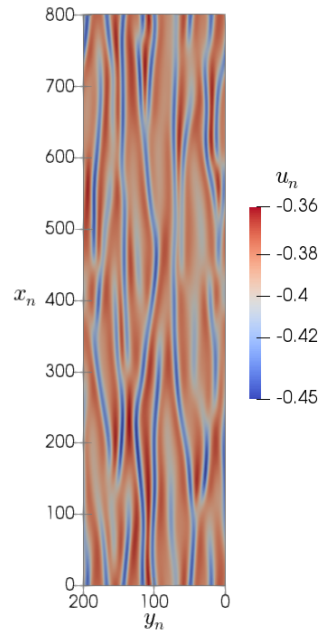


Figure 3.15: Unstable longitudinal rolls for large domain sizes ($\alpha = 20^\circ$, $\Pi_s = 4$)

3.4 Progression Toward Turbulence

All the katabatic flow scenarios presented until now fall within an intermediate regime between fully laminar and turbulent conditions, which can be further defined as the unstable laminar regime given the presence of the instability rolls as has been demonstrated. Let's now consider katabatic flow scenarios with increased values of the stratification perturbation parameter that, as predicted by the formulation of such a parameter, become more dynamically unstable and break into turbulence. The base case for this analysis corresponds to $\alpha = 30^\circ$, $\Pi_s = 10$, $Re = 2.8 \times 10^1$, which falls within the transverse mode regime. Keeping the slope constant, Π_s is then increased to consider two additional scenarios: $\Pi_s = 100$, $Re = 2.8 \times 10^2$ and $\Pi_s = 1000$, $Re = 2.8 \times 10^3$. The Reynolds number (Re) was computed using the length and velocity scales in Eqs. 2.12 and 2.13, respectively.

Regarding the simulation parameters corresponding to these three cases, the spatial mesh resolution was kept constant and the temporal discretization was adjusted, maintaining a stability criterion of $CFL \leq 0.4$. The $\Pi_s = 10$ and 100 cases used a based domain of size $200l_0 \times 200l_0 \times 50l_0$, which was made larger for the highest $\Pi_s = 1000$ case only, which used a domain size of size $800l_0 \times 800l_0 \times 50l_0$. This choice of domain size and mesh resolution relationship intended to analyze the presence of large-scale energy-containing motions in the flow, but does not perform well to resolve the dissipative scales. Based on the resolvability condition for DNS [50], the grid spacing Δx_i for any direction $i = 1, 2, 3$ should satisfy $\Delta x_i \leq 2L_m$, where L_m corresponds to the Kolmogorov scale. This scale is defined in terms of the kinematic viscosity ν and the rate of dissipation of turbulent kinetic energy ε through $L_m = (\nu^3/\varepsilon)^{1/4}$, as proposed by Pope [50]. For katabatic flow scenarios, the surface buoyancy flux B_s and ε are dimensionally equivalent, and the Kolmogorov scale for these kinds of flows is defined by Umphrey et al. as $L_m = (\nu^3/|B_s|)^{1/4}$, whose turbulent katabatic flow simulations satisfied $\Delta \leq 2(\nu^3/|B_s|)^{1/4}$, with Δ being the uniform grid spacing along all directions, and their choice of domain size along both the x and y directions was $60l_0$. In the simulations presented in this thesis, however, the grid spacing is uniform along the x and y directions only ($\Delta x = \Delta y$), and is twice as fine along the z direction ($\Delta z = 0.5\Delta x$). For the most dynamically unstable analyzed case of $\Pi_s = 1000$, the largest grid spacing

satisfies $\Delta x < 4(\nu^3/|B_s|)^{1/4}$ and the domain size along that same direction is $L_x = 800l_0$. Such large domain size for turbulent scenarios constitute the main difference with respect to previously reported turbulent katabatic flow simulations. However, the combined effect of fine grid spacing and large domain sizes remains to be assessed.

The first structural difference among these increasingly unstable flow scenarios comes from the absence of the organized vortical structures initially observed in the unstable laminar regime. Figure 3.16 reveals the presence of the longitudinal rolls through vorticity isosurfaces for the base case in the transverse mode regime. These unstable rolls are also present in the contour plots of the multiple flow fields presented in Fig. 3.17 and exhibit snaking and meandering behaviors. As Π_s increases, these vortical structures become less organized and the isosurfaces become smaller, thus revealing that finer vortex scales corresponding to smaller eddies emerge as the flow breaks into turbulence. Such smaller scales are observed in Fig. 3.18 and Fig. 3.20 for the $\Pi = 100$ and $\Pi_s = 1000$ cases, respectively. When analyzing the flow field contour plots for each of these highly dynamically unstable cases, the w -velocity component is the most susceptible for the organized vortical structures to disappear. Figure 3.19(b) reveals that, for $\Pi_s = 100$, the high and low magnitude regions are much smaller in this one than in the rest of the fields. Such a difference among the fields intensifies for $\Pi = 1000$, for which the w -velocity component field reached a mean and constant value close to zero, as shown in Fig. 3.21(b). Additionally, the u -velocity component contour for the turbulent case at $\Pi_s = 1000$ exhibits a stripe-like structure, as seen in Fig. 3.21(a), that is not observed for the rest of the fields. This structure was also present when this same case was simulated in smaller domain, and remained in the flow even after making the domain 4 times larger in both x and y directions. One possible explanation for such a behavior could be that it corresponds to the signature of the longitudinal rolls. However, Flores and Riley [51] attributed the presence of these kinds of structures in simulated turbulent flows through DNS to constraints coming from the choice of domain size. Therefore, the nature of this structure in the turbulent katabatic flow simulations remains an open question and should be investigated further.

The second major difference among the analyzed cases corresponds to the frequency component of their temporal signals sampled in the quasi-stationary regime. Figure 3.22

shows the PSD computed from temporal signals of pressure with a length corresponding to 10 complete periods of the *en masse* frequency, which is constant for all three dynamically unstable cases. Zooming into the first two normalized frequencies reveals how the *en masse* oscillations become more relevant as Π_s increases. When comparing the amplitude attained by frequencies in proximity to $f_n = 1$ against the amplitude of other identified dominant frequencies in the same flow configuration, Fig. 3.22(a) reveals that these oscillations are insignificant in the unstable laminar regime, but are of comparable, and even higher, amplitude for higher Π_s values, as shown in Figure 3.22(b) and (c) for $\Pi_s = 100$ and $\Pi_s = 1000$, respectively. Figure 3.23, on the other hand, shows the complete PSD spectra in logarithmic scale computed from buoyancy signals, confirming that, as the flows breaks into turbulence, the signals exhibit higher frequency components with increasing Π_s values, and with corresponding amplitudes that are multiple orders of magnitude larger than in the unstable laminar regime, therefore, higher Π_s values reveal higher energy PSD spectra.

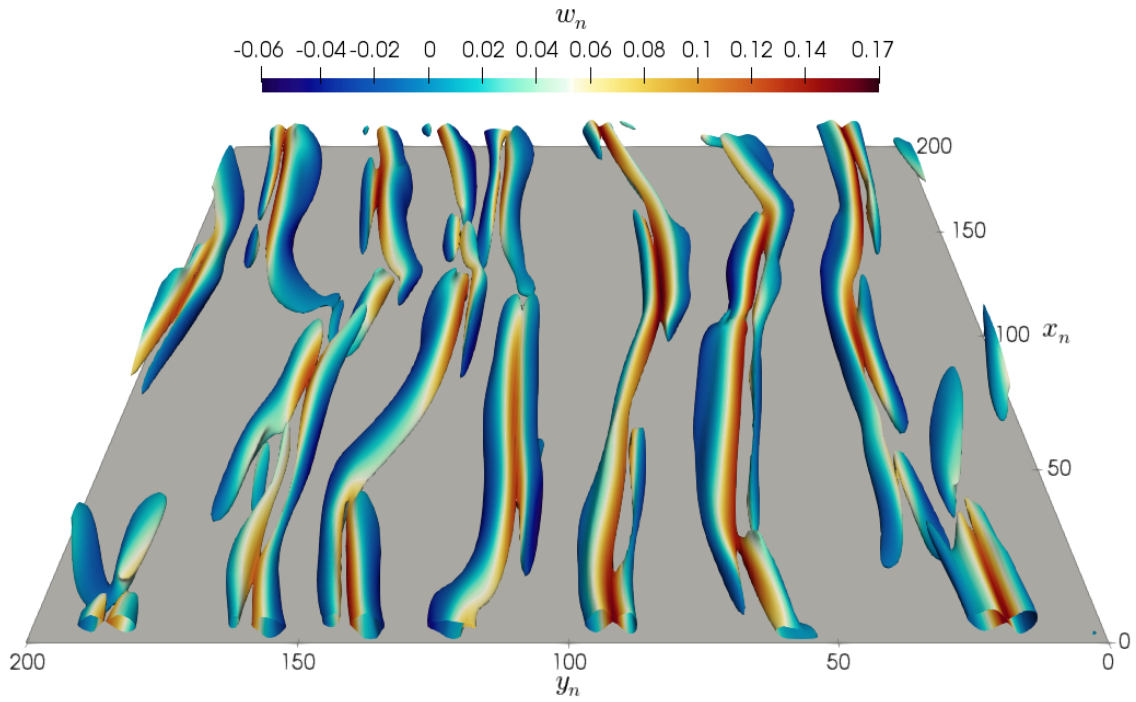


Figure 3.16: Vorticity structures at low Π_s numbers ($\alpha = 30^\circ, \Pi_s = 10$) computed from Q -criterion at 4% of its maximum positive value. The emerging structures correspond to the longitudinal instability rolls.

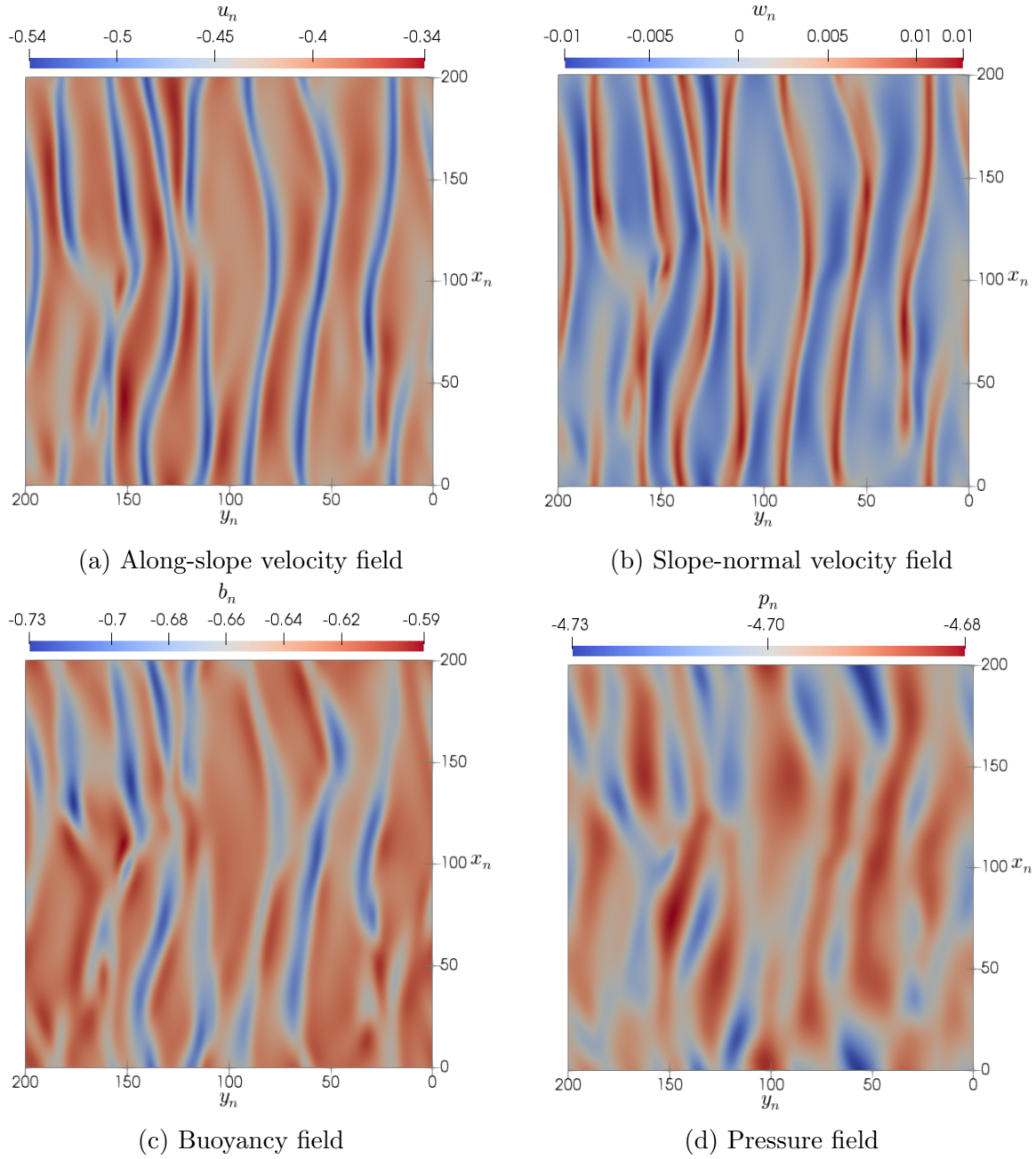


Figure 3.17: Contour plot visualizations at low Π_s numbers ($\alpha = 30^\circ, \Pi_s = 10$). The emerging structures correspond to the longitudinal instability rolls.

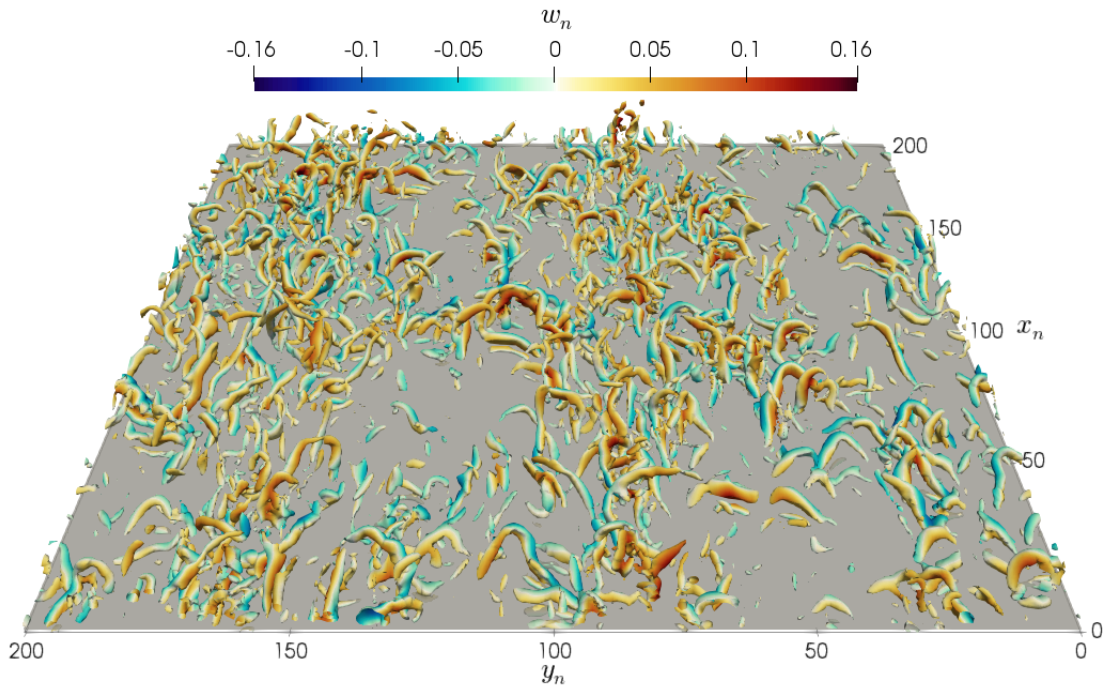


Figure 3.18: Vorticity structures at moderate Π_s numbers ($\alpha = 30^\circ, \Pi_s = 100$) computed from Q -criterion at 4% of its maximum positive value.

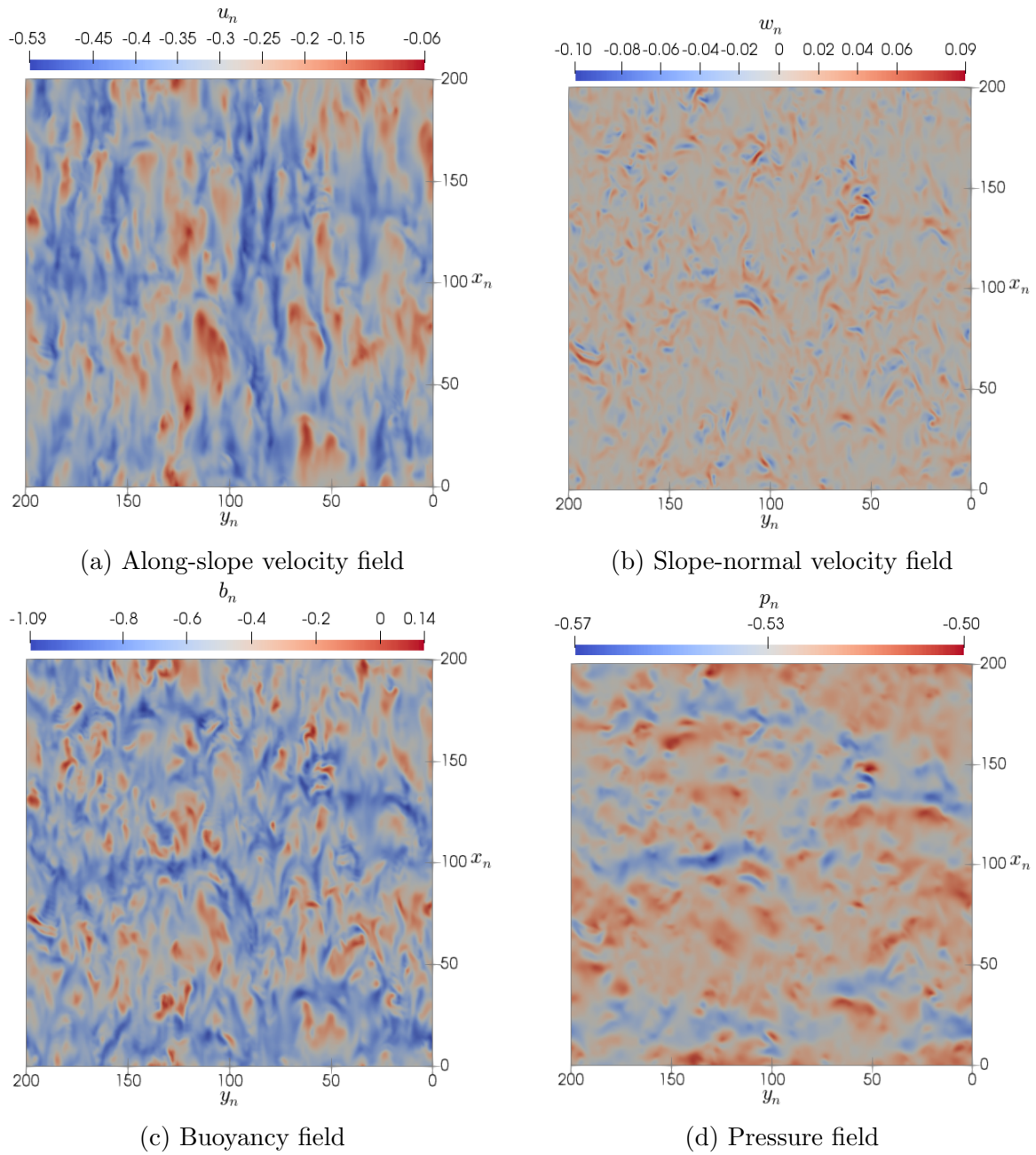


Figure 3.19: Contour plot visualizations at moderate Π_s numbers ($\alpha = 30^\circ, \Pi_s = 100$)

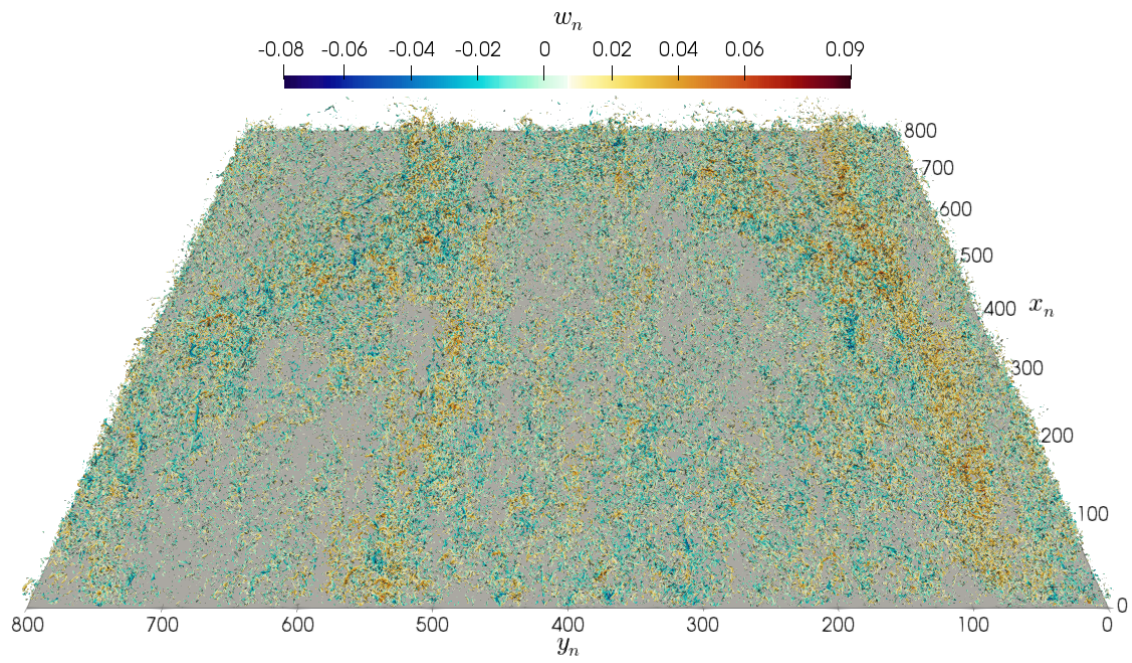


Figure 3.20: Vorticity structures at high Π_s numbers ($\alpha = 30^\circ$, $\Pi_s = 1000$) computed from Q -criterion at 4% of its maximum positive value.

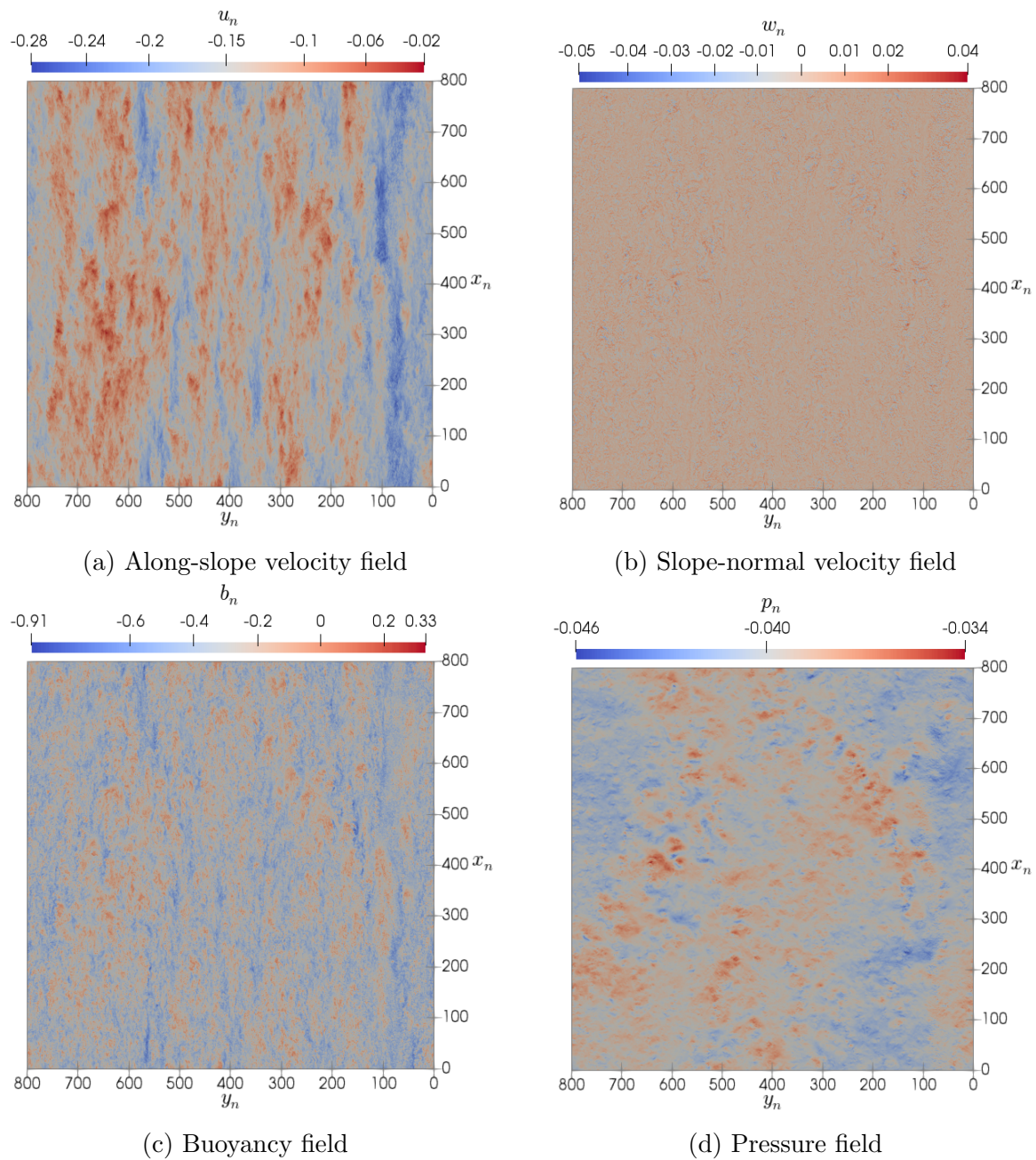
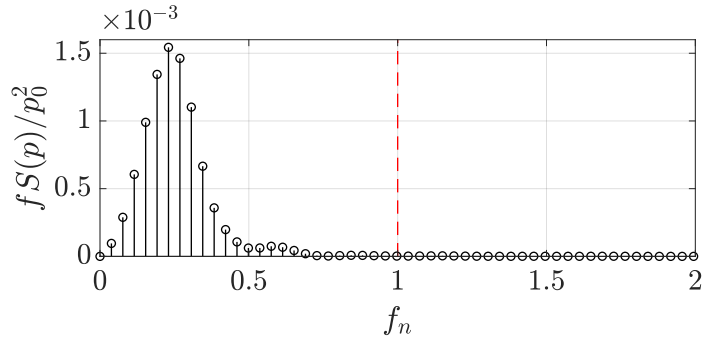
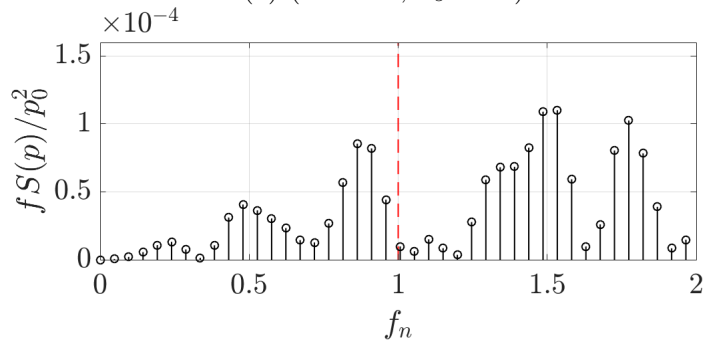


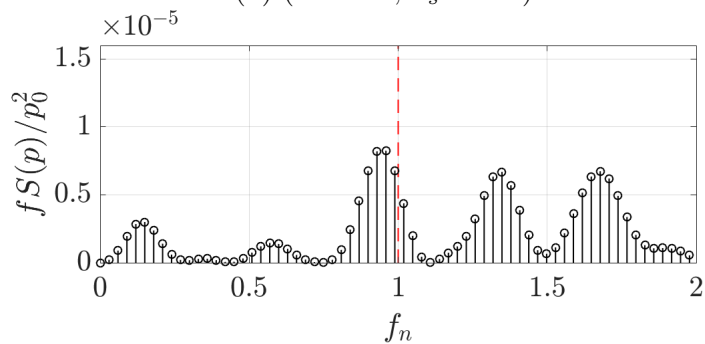
Figure 3.21: Contour plot visualizations at high Π_s numbers ($\alpha = 30^\circ$, $\Pi_s = 1000$)



(a) ($\alpha = 30^\circ, \Pi_s = 10$)

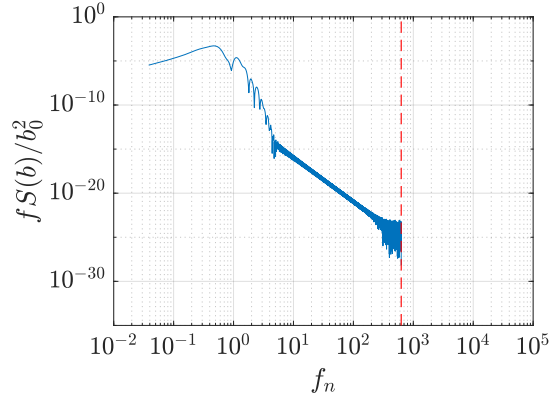


(b) ($\alpha = 30^\circ, \Pi_s = 100$)

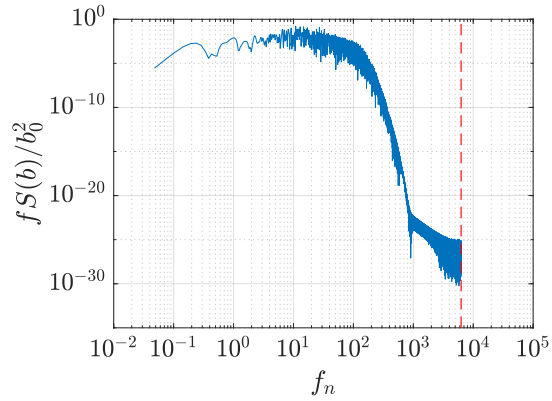


(a) ($\alpha = 30^\circ, \Pi_s = 1000$)

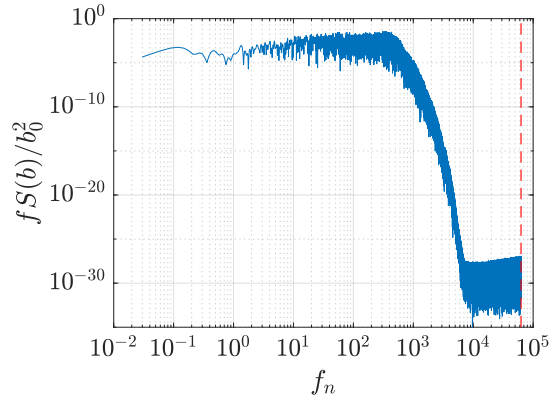
Figure 3.22: Zoomed frequency spectra for low, moderate, and high Π_s values computed from temporal pressure signals. Vertical red dashed line denotes the *en masse* frequency



(a) $\alpha = 30^\circ, \Pi_s = 10$



(b) $\alpha = 30^\circ, \Pi_s = 100$



(c) $\alpha = 30^\circ, \Pi_s = 1000$

Figure 3.23: Complete frequency spectra for low, moderate, and high Π_s values computed from temporal buoyancy signals. Red dashed lines represent the cutoff frequency $F_s = 1/\Delta t$, with $\Delta t = 1 \times 10^{-2}$ s, 1×10^{-3} s, 1×10^{-4} s for subfigures (a), (b), and (c) respectively. The cutoff frequency is normalized with f_0 and divided by 2 to account for the symmetry of the PSD spectra around the folding frequency.

3.5 Longitudinal Rolls Dynamics

Based on the flow field visualizations presented for the longitudinal rolls shown in Figs. 3.5, 3.13, and 3.17, potential patterns in the separation between the rolls could be observed. This section, as a complement to the instability dynamics of the longitudinal rolls discussed in section 3.3, explores the spatial wavelength characteristics of these instability rolls and presents predictive relationships based on simulation results.

Consider the discrete signals in the spatial domain obtained from sampling the u -velocity component at each one of the mesh points along the y direction. For a given domain slice, there will be as many of these signals as points in the x direction, and each of the signals is also a function of time. When those signals are translated into the wavelength domain, as presented in Fig. 2.4, the largest amplitude wavelengths reveal the most dominant wavelengths present in the signals and provide a systematic approach to assessing the separation between the longitudinal rolls. Yet, given the meandering and snaking dynamics of the longitudinal rolls, multiple competing wavelengths with about the same amplitude are identified depending on the chosen location and time snapshot. However, if the results of these analyses in the wavelength domain are averaged among all the signals collected for each location along the x direction and multiple snapshots in time, then the average wavelength is obtained. Results of this analysis implemented for multiple katabatic slope flow configurations are presented in Fig. 3.24, where λ_y/l_0 corresponds to the normalized wavelength along the y directions.

Given the differences in the dynamics of each slope flow configuration, the amplitudes of the wavelengths identified don't exhibit a constant value among the analyzed cases, although the presence of a single most dominant wavelength is clear in each case. These peaks in the wavelength domain show that the average transverse wavelength of longitudinal rolls is indeed a function both of α and Π_s . Extending the analysis to more katabatic flow configurations reveals the underlying relationships between the slope flow parameters and the separation between the longitudinal rolls, which are shown in Fig. 3.25. Note how shallow slopes feature large wavelengths that increase drastically with Π_s , while approaching a constant value of $\lambda_y/l_0 \approx 20$ for steeper slopes such that $\alpha > 30^\circ$, for which the dependence on Π_s is weaker.

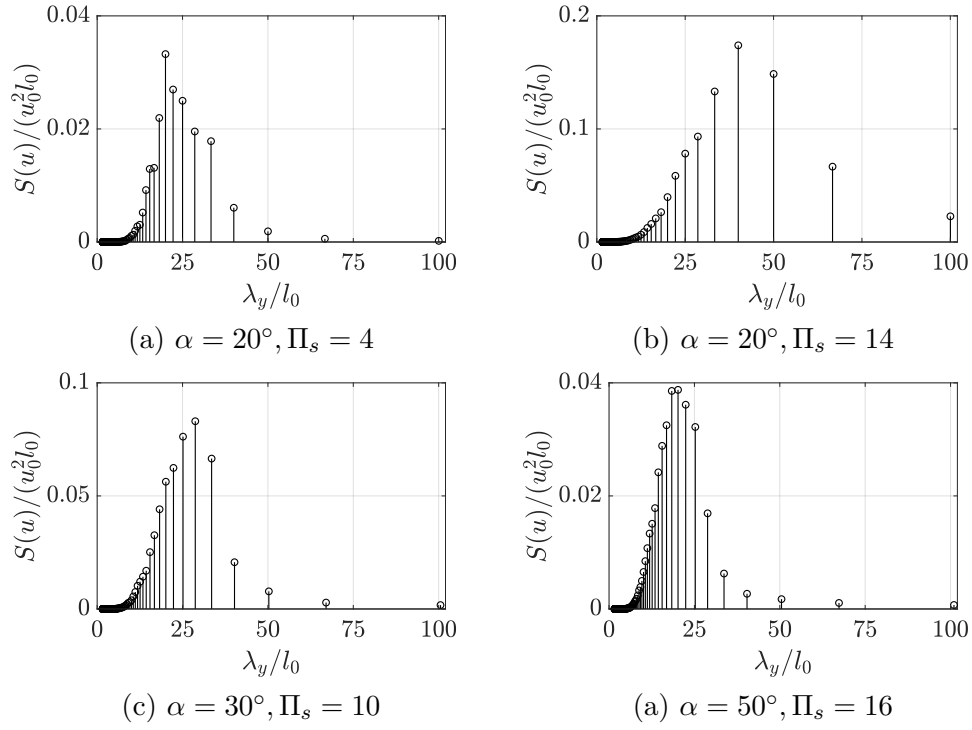


Figure 3.24: Longitudinal rolls wavelength along the cross-slope direction

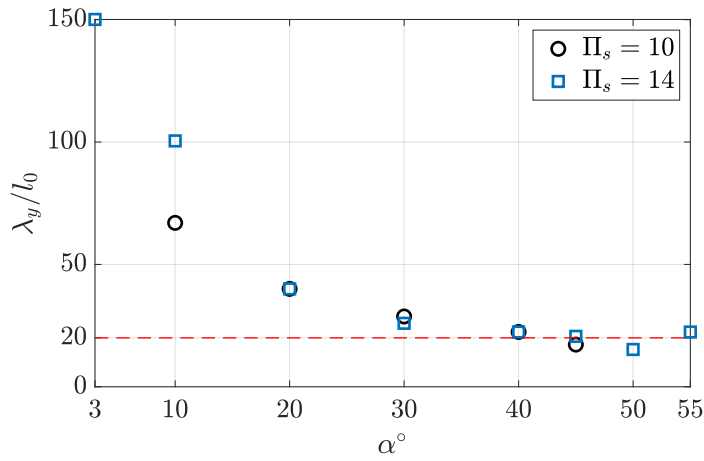


Figure 3.25: Longitudinal rolls wavelength along the cross-slope direction as a function of α and Π_s

3.6 Traveling Wave Rolls

The traveling wave dynamics shown in prior sections have revealed that this type of instability exhibits dominant characteristics both in the temporal and spatial domain, as seen, for instance, in Figs. 3.2(c) and 3.7(a), respectively, for the u -velocity field from the $\alpha = 80^\circ, \Pi_s = 20$ case. This section explores the relationship between the wave speed of these rolls and the slope flow parameters.

The dimensional wave speed, also known a phase velocity, of the traveling wave rolls (v_p) is defined by:

$$v_p = f\lambda_x, \tag{3.1}$$

where f corresponds to the dimensional frequency observed in the time domain and λ_x corresponds to the wavelength along the direction through which the wave propagates, which is the along-slope direction for these type of rolls. The traveling wave dynamics were observed to be stronger in the buoyancy field, therefore, the results to be presented are based on this field. The most dominant wavelength characterizing the separation between the rolls along the x direction was computed using the approach detailed in section 3.5, while the temporal frequency was identified using the PSD estimate outlined in section 2.6. An appropriate scale to normalize the wave speed computations was found to be the average jet velocity \bar{U}_{jet} obtained from the simulations. Such a velocity scale was computed averaging the u -velocity field over time at a slice parallel to the xy plane extracted at the jet's height predicted by Prandtl's laminar solution $z_{n,\text{jet}}$.

Consider the temporal and spatial PSD shown in Figs. 3.26 and 3.27 for two different slope flows scenarios with a fixed slope of $\alpha = 80^\circ$ and $\Pi_s = 20, 40$. These cases correspond to the longitudinal mode of instability and exhibit the traveling wave rolls with different normalized traveling wave frequency and normalized wavelength. Note, however, that these two cases have the same length and frequency scales as defined by Eqs. 2.12 and 2.16, respectively, since only the surface buoyancy flux is modified between them. Consequently, the dimensional values of f and λ_x are different for these two cases and increase with Π_s , which results in a different dimensional wave speed as described by Eq. 3.1. The dependence

of the wavelength and frequency of the traveling wave rolls on the slope angle, on the other hand, has been observed to be weak for the narrow range of slopes where the traveling wave rolls are observed as a single mode and hence it's not addressed here.

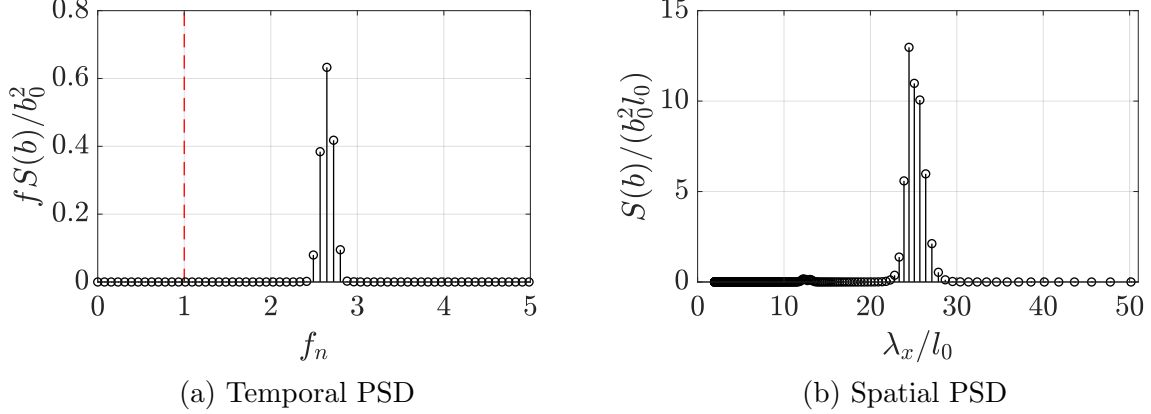


Figure 3.26: Temporal and spatial PSD for $\alpha = 80^\circ, \Pi_s = 20$. Data sampled at height $z = z_{n,\text{jet}} = 0.022L_z$. Domain size with dimensions $L_x = 1000l_0, L_y = L_z = 50l_0$

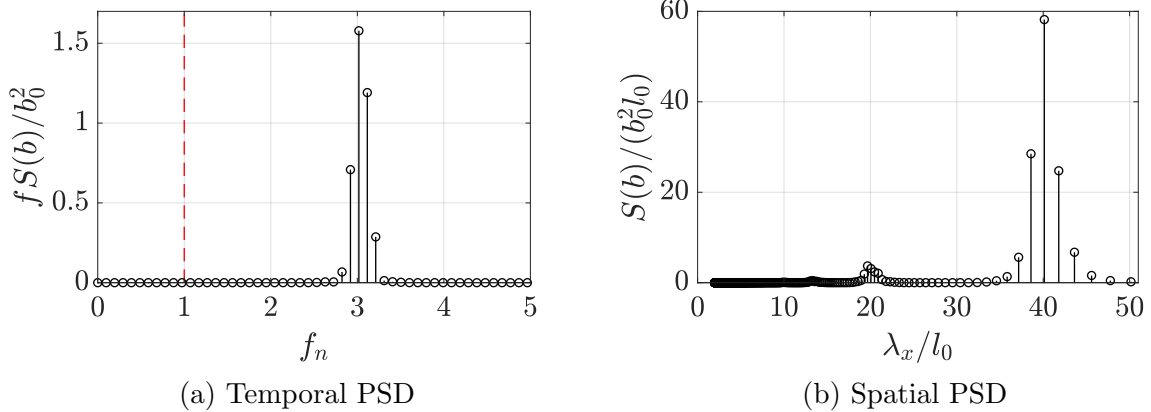


Figure 3.27: Temporal and spatial PSD for $\alpha = 80^\circ, \Pi_s = 40$. Data sampled at height $z = z_{n,\text{jet}} = 0.022L_z$. Domain size with dimensions $L_x = 1000l_0, L_y = L_z = 50l_0$

Analyzing the presence of the traveling wave at multiple heights above the surface, highlights that different temporal frequencies are found for some locations in the flow field. Figures 3.28(a) and (b) shows two particular locations at greater heights that exhibit the same temporal frequency observed at the jet's height $z_{n,\text{jet}}$. However, this behavior doesn't

hold true at the locations shown in Figs. 3.28(c) and (d), for which much smaller amplitude oscillations are observed for distinct frequencies. At the height $z = 0.5L_z$, both the traveling wave frequency and the *en masse* oscillations frequency are dominant, while at $z = 0.7L_z$, only the *en masse* oscillations frequency is dominant but with a smaller amplitude in this case. Therefore, simulation results in the unstable laminar regime, have revealed that the strength of the emerging traveling wave rolls is not constant throughout the domain, as seen in Fig. 3.28, which is a behavior that requires further investigation. However, for the purpose of the current analysis, only the results extracted at jet's height will be considered. Additionally, for temporal signals extracted at several heights for a case exhibiting the longitudinal rolls, Fig. 3.29 shows how the frequency components remain constant while changes only happen in the amplitude of these most dominant frequencies, still the amplitudes remain in the same order of magnitude. Note that for all the heights away from the surface presented in Figs. 3.28 and 3.29, Prandtl's laminar solution predicts buoyancy values that have technically converged to zero, yet it is important to note that the nature of that laminar solution corresponds to exponentially damped sine waves that exhibit infinite inflection points. These inflection points could also be also present in the unstable laminar regime and exhibit different dynamics related to the emergence of the instability rolls, which is a possible explanation for the observed behavior.

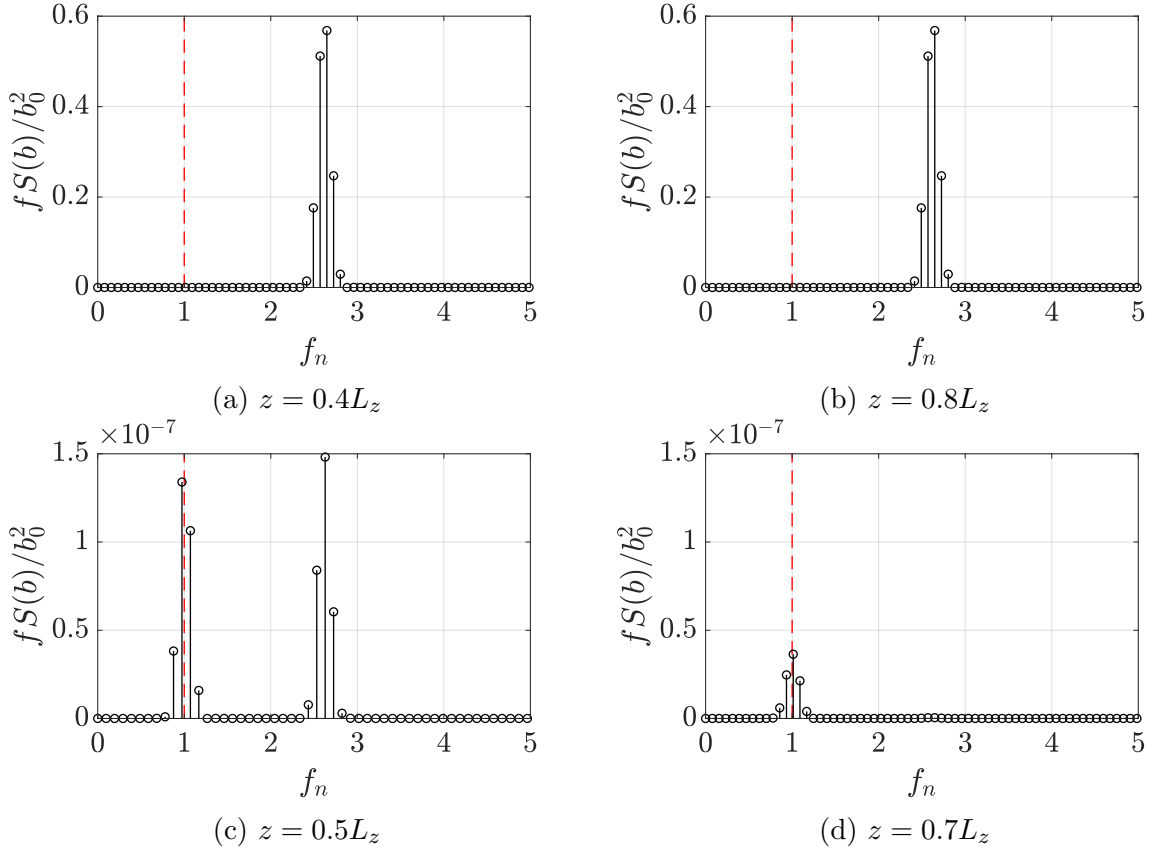


Figure 3.28: Most dominant frequencies at multiple heights above the surface for $\alpha = 80^\circ$, $\Pi_s = 20$. Domain size with dimensions $L_x = 1000l_0$, $L_y = L_z = 50l_0$

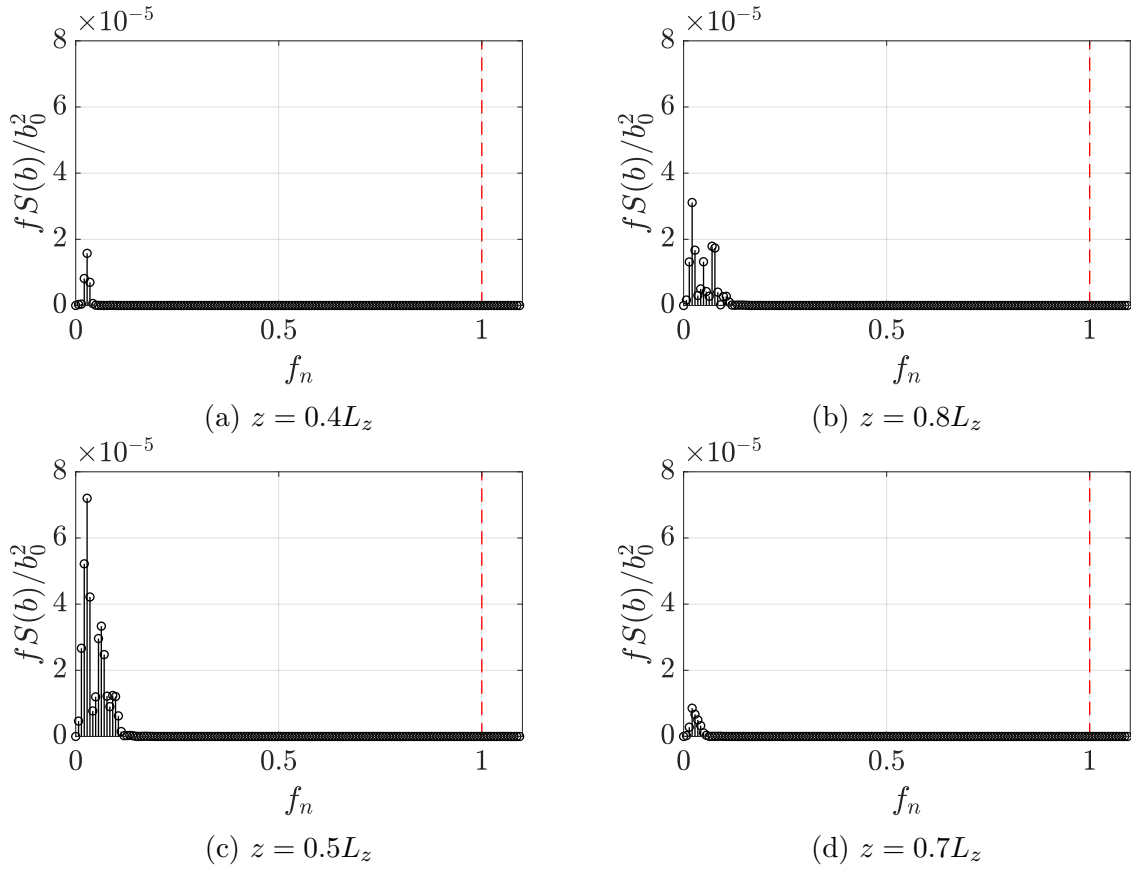


Figure 3.29: Most dominant frequencies at multiple heights above the surface for $\alpha = 20^\circ$, $\Pi_s = 4$. Domain size with dimensions $L_x = L_y = 200l_0$, $L_z = 50l_0$

Computing the wave speed of the longitudinal mode rolls for multiple katabatic flow scenarios reveals that the traveling wave is advected by the mean jet's velocity \bar{U}_{jet} at the height $z = z_{n,\text{jet}}$, as shown in Fig. 3.30. Yet, data collected at other heights away from the surface needs to be evaluated as well to assess if the traveling wave is transported by the mean jet velocity at all locations. Such a wave speed is observed with improved agreement for $\Pi_s < 38$, after which the traveling wave rolls seem to start moving with a slightly faster speed than \bar{U}_{jet} , hence suggesting a regime change. Additionally, the track of the traveling wave was lost for $\Pi_s > 50$. Such a relationship between the traveling wave speed and the mean jet velocity of the flow reveals that predicting \bar{U}_{jet} would be enough to estimate the longitudinal modes wave speed. The normalized mean jet velocity as a function of Π_s for $\alpha = 80^\circ$ is presented in Fig. 3.31 and compared with the jet velocity predicted by Prandtl's laminar solution. Note how the normalized jet velocity from the simulation results decreases as Π_s increases, contrary the velocity scale u_0 , which is an increasing function of Π_s when the remaining variables are kept constant in Eq. 2.13. Therefore, the dimensional mean jet velocity is also an increasing function of Π_s .

Approximate values of the expected wave speed are especially relevant for anticipating the wavelength of the traveling wave rolls, which would help defining the required along-slope domain length accordingly such that several rolls are captured. Figure 3.32 presents the evolution of the traveling wave frequency with Π_s , which has an increasing behavior for $\Pi_s < 38$ and then starts decreasing. Note, however, that the wave speed is a continuously increasing function of Π_s , which means that, once the frequency starts decreasing, the wavelength would need to increase abruptly to match the wave speed. Such a drastic change in the wavelength is observed in Fig. 3.33, where an slightly increasing trend is observed for $\Pi_s = 50$, and then the wavelength is more than doubled for $\Pi_s = 50$.

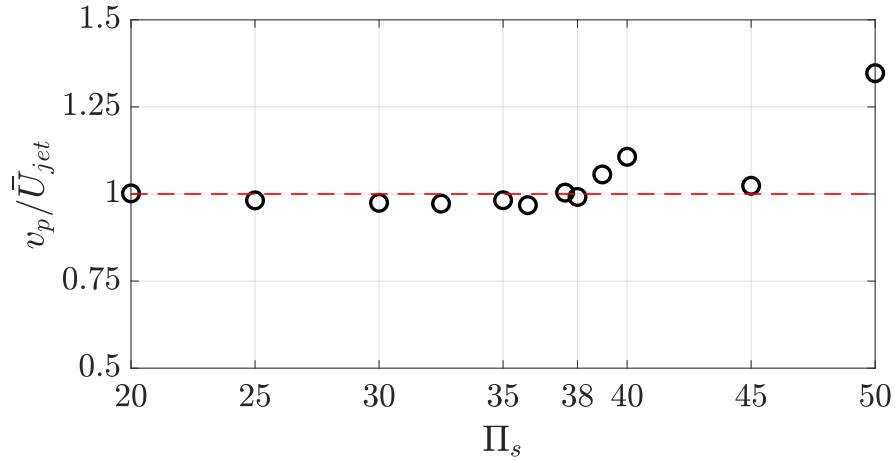


Figure 3.30: Normalized traveling wave speed as a function of Π_s for $\alpha = 80^\circ$

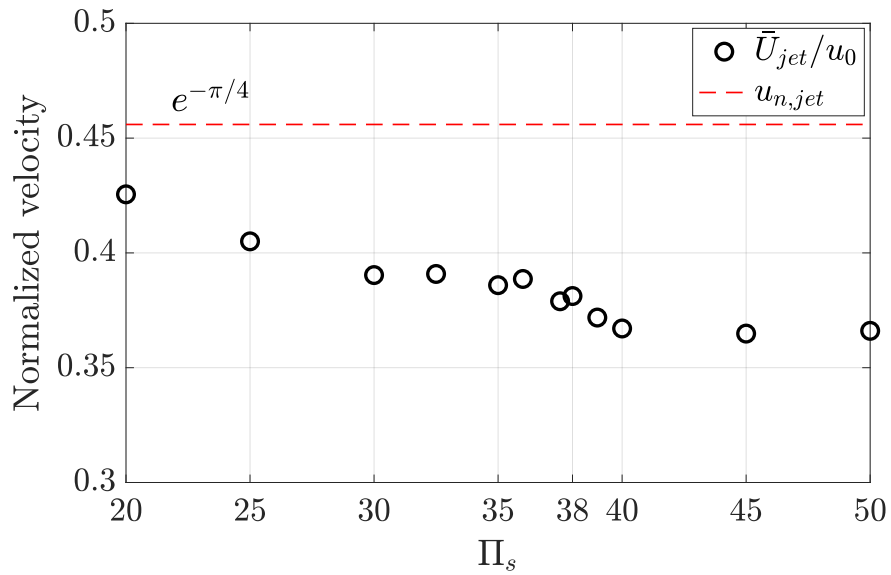


Figure 3.31: Normalized mean jet velocity as a function of Π_s for $\alpha = 80^\circ$. $u_{n,jet} = e^{-\pi/4}$ is the normalized jet velocity predicted by Prandtl's laminar solution, as presented in section 2.2.

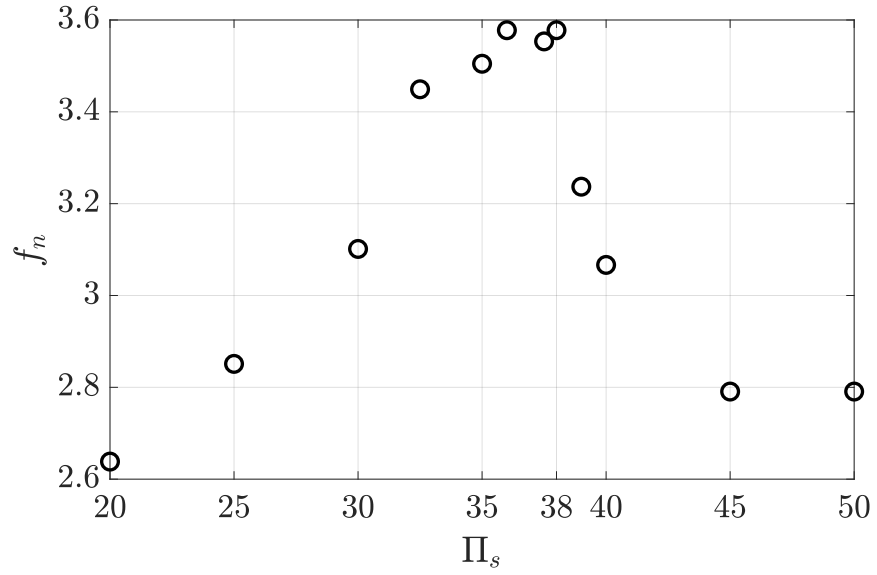


Figure 3.32: Normalized traveling wave frequency as a function of Π_s for $\alpha = 80^\circ$

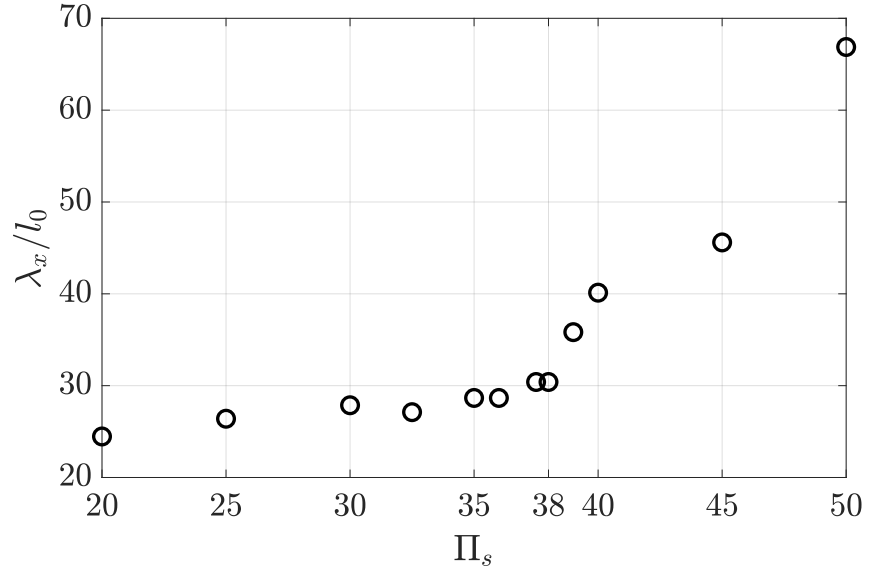


Figure 3.33: Normalized traveling wave wavelength as a function of Π_s for $\alpha = 80^\circ$

Although the presented visualizations of the traveling wave rolls show them as continuous and straight rolls aligned with the cross-slope direction, this is not the case as larger domain sizes along y are analyzed. Figure 3.34 shows how the rolls start curving when the increasing the cross-slope domain size to $L_y = 800l_0$, which could be the result of a secondary instability emerging in the flow. Note that despite being curved, these rolls are not colliding with themselves and continue to be transported by the mean jet velocity of the flow, exhibiting an uniform separation and fixed temporal frequency. Additionally, no a clear trend is identified in the shape of the such a curvature with increasing cross-slope domain sizes, as shown in Figs. 3.35(a) and 3.35(b) for $L_y = 2400l_0$ with two different along-slope domain sizes, corresponding to $L_x = 100l_0$ and $L_x = 200l_0$, respectively. These results show how the domain size along both directions is conditioning the emergence of additional motions that correspond to the instability of the primary traveling wave rolls.

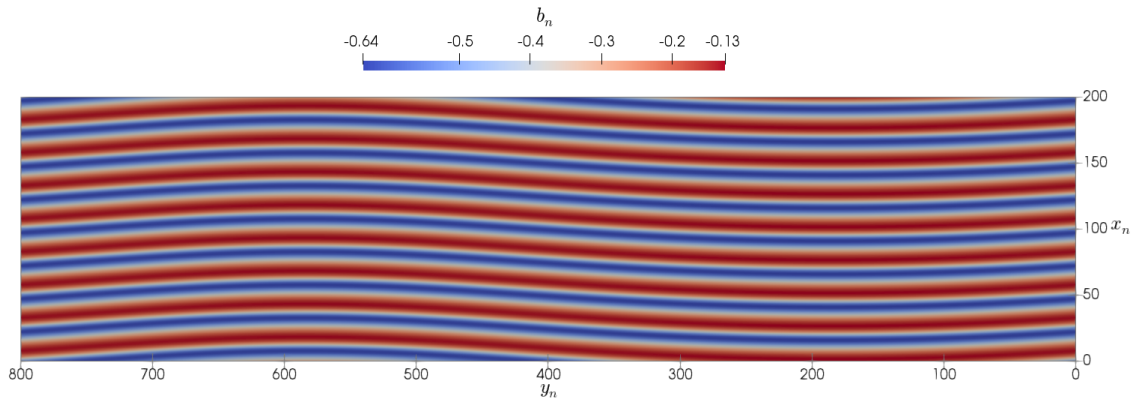


Figure 3.34: Curved traveling wave rolls for large domain sizes - $L_y = 800l_0$ ($\alpha = 80^\circ$, $\Pi_s = 20$)

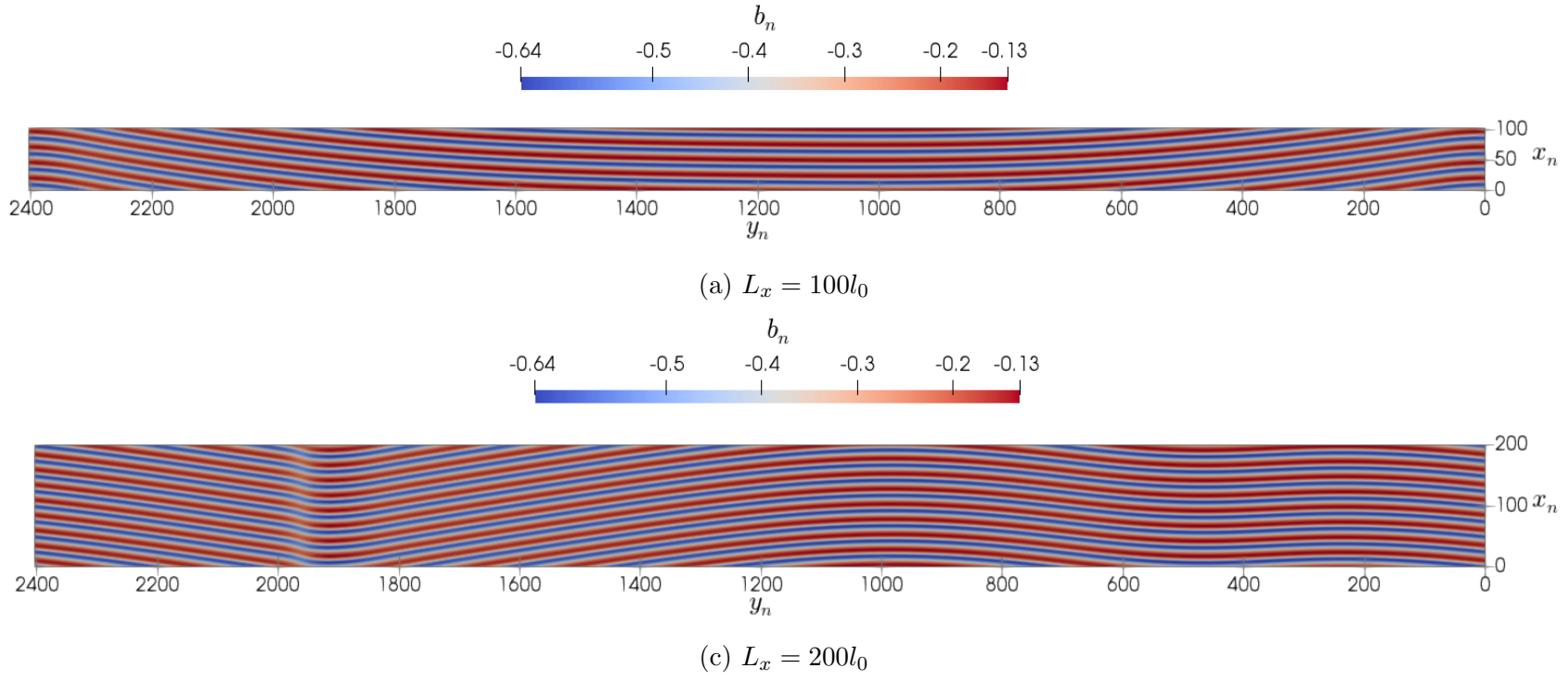


Figure 3.35: Curved traveling wave rolls for large domain sizes - $L_y = 2400l_0$ ($\alpha = 80^\circ$, $\Pi_s = 20$)

3.7 Reduced-Order Representation of Instabilities

ROMs of the dynamical systems governing the evolution of the instability rolls in unstable laminar katabatic flows were built through DMD. Such a technique, presented in detail in section 2.7, was applied to the three katabatic slope flow scenarios introduced in section 3.1, which feature the three types of instability rolls predicted by the instability map (Fig. 2.2) proposed by Xiao and Senocak [33], namely longitudinal rolls, traveling wave rolls, and mixed/higher-order rolls. Each DMD model is presented separately for each type of instability, discussing the minimum number of DMD modes required to capture the dynamics of the instabilities and the accuracy of the flow field reconstructions based on the reduced DMD model.

All DMD models were built using a total of 300 snapshots of the flow field, which were sampled in the quasi-stationary regime with a fixed spacing of $100\Delta t$ between two consecutive snapshots, with Δt being constant for each katabatic flow case. These snapshots correspond to two-dimensional contour plots of the u -velocity component extracted at the jet's height predicted by Prandtl's laminar solution $z_{n,\text{jet}}$. The snapshots were reshaped into one-dimensional column vectors and arranged in the data set matrix discussed in section 2.7. The choice of the reduction size was based on the energy content of each SVD mode, and the overarching goal was to choose as few modes as possible such that most of the dynamics were accurately represented. Note that, while DMD modes ϕ have both real and imaginary parts, only the real part is presented, which is normalized using the velocity scale presented in Eq. 2.13 such that $\phi_n = \phi/u_0$.

Overall, it was observed that a single DMD mode is capable of representing the dynamics of the longitudinal rolls, and two additional modes, which happen to be complex conjugate, are required to represent the traveling wave dynamics. DMD was also found to be a powerful tool for decomposing the mixed/higher-order rolls into their longitudinal and traveling wave components, and, while some information from the data set is lost in the dimensionality reduction, the reconstructed flow fields from the obtained DMD models feature the same temporal and spatial overall characteristics observed in the simulation results. An important result is that the single mode representing the longitudinal rolls dynamics does not exhibit

an imaginary component in its corresponding eigenvalue λ and the mode remains stationary, hence subtracting the meandering dynamics of the rolls in the DMD model. As discussed in section 2.7, the imaginary component of λ corresponds to the oscillatory frequency of the DMD mode, which is observed in the DMD modes that represent the traveling wave only. Yet, this oscillation frequency in the DMD eigenvalue doesn't match directly the temporal oscillation frequency of the flow field observed in the simulation results for the quasi-steady regime, as seen in Fig. 3.26(a), for example. However, extracting the temporal signal from the DMD reconstructed model and computing its frequency component reveals the same oscillation frequency observed in the simulation results. Additionally, the wavelength in the traveling wave rolls from the in the DMD modes also match the simulation results, thus revealing that an accurate representation of the traveling wave dynamics both in space and time is achieved.

Longitudinal Rolls

Figure 3.36(a) presents the magnitude of the SVD eigenvalues of the data set corresponding to the longitudinal rolls snapshots. These eigenvalues experience a sharp change in magnitude from the first to the second mode, thus revealing that the first mode captures most of the information from the data set. This is confirmed by the energy content (Eq. 2.28) for each reduction size r shown in Fig. 3.36(b). If only the first SVD mode is used, corresponding to a reduction size of $r = 1$, then more than 99% of the information would be captured, with small changes for increasing r and ultimately reaching a convergence to 100% for a sufficiently large r . This analysis highlights that $r = 1$ is the optimal reduction size for the longitudinal rolls dynamics, which would result in a single DMD mode, whose real part is shown in Fig. 3.37(a), with corresponding eigenvalue shown in Fig. 3.37(b). Note that this eigenvalue is approximately equal to 1 and only exhibits a real component.

Once the flow field is reconstructed for any time using Eq. 2.27, only the amplitude of the mode changes, but the longitudinal rolls observed in Fig. 3.37(a) remain still, thus defining the corresponding DMD mode as stationary. Such a behavior is observed in Fig. 3.38(b), which corresponds to the flow field reconstructed for the last sampled snapshot. Comparing the DMD reconstruction against the simulation data in Fig. 3.37(a) reveals that the location

of the rolls does not match exactly, and that the DMD reconstructed rolls are not as curved as the ones obtained from the simulations, hence confirming that the DMD mode filtered the meandering behavior from the longitudinal rolls. Additionally, Fig. 3.39 reveals the most dominant wavelength in the cross-slope direction computed directly from the DMD mode shown in Fig. 3.37, which is about $5l_0$ larger than the to the most dominant wavelength identified in the simulation data for this same case, as shown in Fig. 3.24(a).

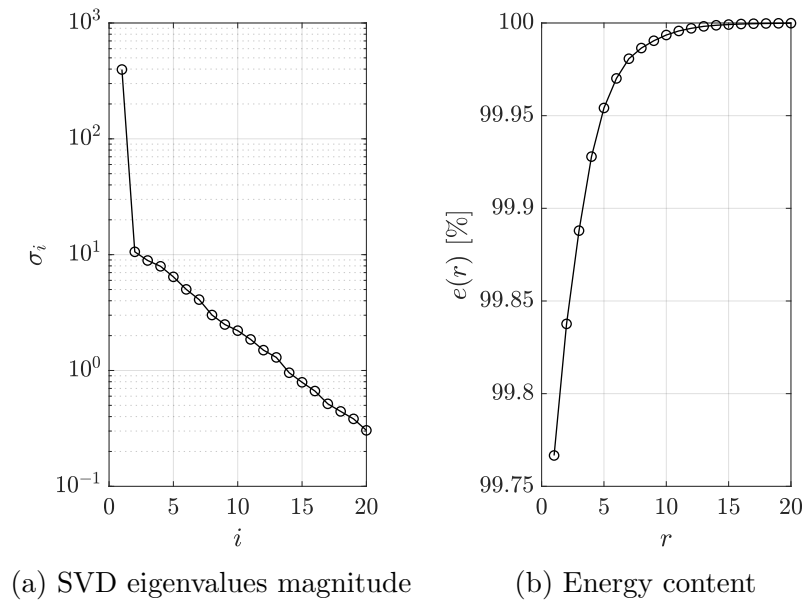


Figure 3.36: SVD eigenvalues for $\alpha = 20^\circ$, $\Pi_s = 4$

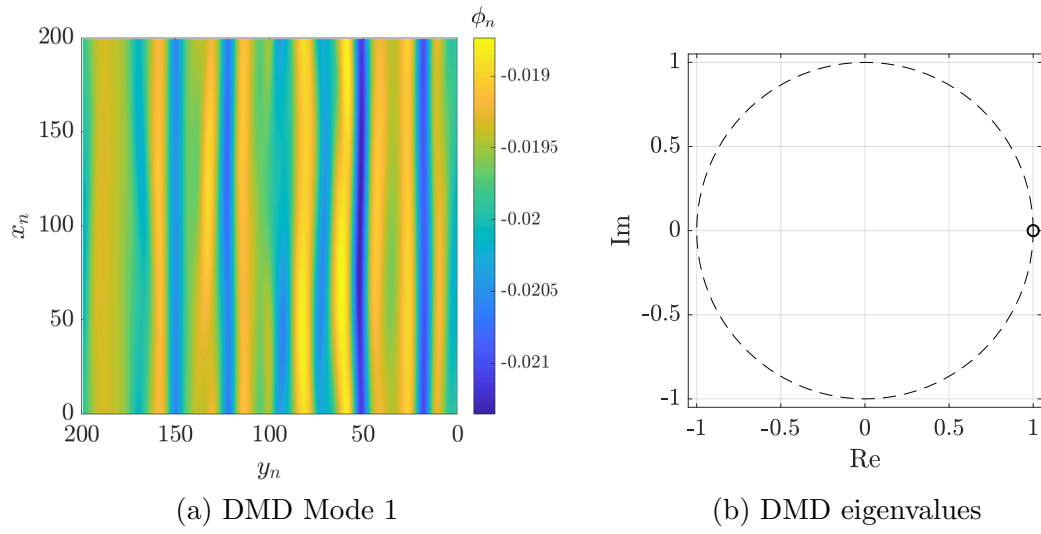


Figure 3.37: DMD modes and eigenvalues for $\alpha = 20^\circ, \Pi_s = 4$

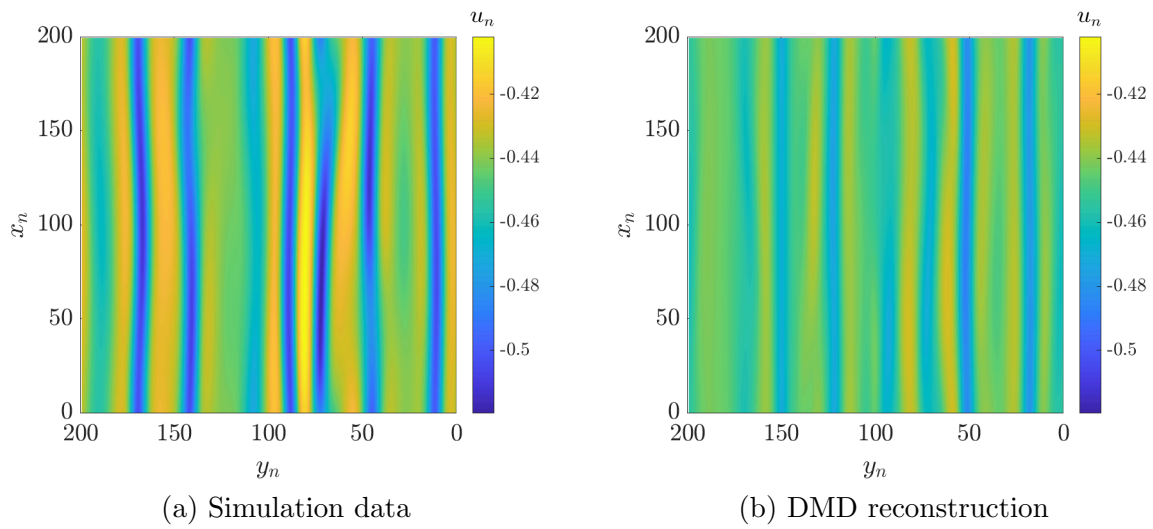


Figure 3.38: DMD reconstruction for $\alpha = 20^\circ, \Pi_s = 4$. Contour plot plotted at final snapshot of training data set

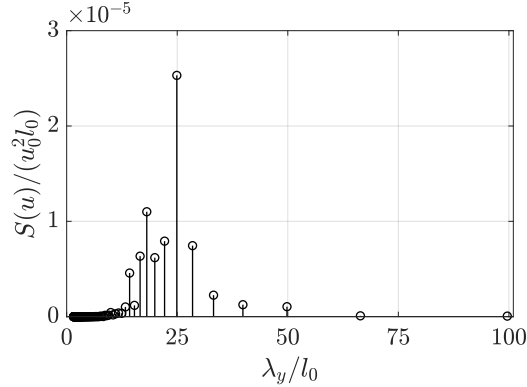


Figure 3.39: Spatial PSD of most dominant DMD mode for $\alpha = 20^\circ$, $\Pi_s = 4$. The wavelength along the cross-slope direction is shown.

Traveling Wave Rolls

The change in the magnitude of the SVD eigenvalues for the data set containing the traveling wave rolls (Fig. 3.40(a)) is not as drastic as the reduction observed for the longitudinal rolls (Fig. 3.36(a)). Additionally, Fig. 3.40(b) reveals how only the first three modes can capture about 100% of the data set information, thus highlighting $r = 3$ as the optimal reduction size for the traveling wave dynamics. Choosing $r = 1$ resulted in a stationary DMD mode, while $r = 2$ resulted in a moving DMD mode that did not represent the traveling wave dynamics correctly. The real part of the three DMD modes obtained with $r = 3$ are shown in Fig. 3.41(a)-(c), and their corresponding eigenvalues are shown in Fig. 3.41(d). The first DMD mode is a stationary mode with eigenvalue $\lambda_1 \approx 1$. The other two modes are complex conjugate, and their corresponding eigenvalues feature both real and imaginary components, thus defining them as traveling modes. Additionally, note that the real part of the DMD mode 1 is almost constant, while modes 2 and 3 exhibit larger changes within the domain.

This combination of modes captures the traveling wave dynamics pretty well both in space and time. Firstly, Fig. 3.42(a) show how much the DMD reconstruction resembles the simulation data for the last snapshot in the data set, shown in Fig. 3.42(b). Additionally, the most dominant wavelength in the second and third DMD modes, presented in Fig. 3.43 matches exactly the most dominant wavelength along the x -direction obtained from simu-

lation data, which is shown in Fig. 3.26(b). Secondly, analyzing the temporal component of the traveling wave oscillations in the DMD model reveals that the exact traveling wave frequency is captured. Note that while the snapshots for the training data set were collected every $100\Delta t$, once the DMD model is built, the solution can be interpolated for any time. Hence, a series of snapshots with spacing $1\Delta t$ can be obtained from the DMD model, from which a temporal signal sampled every time step can be extracted. Analyzing such a signal in the frequency domain reveals the most dominant temporal frequency shown in Fig. 3.44, which matches exactly the most dominant temporal frequency obtained from simulation data that is shown in Fig. 3.26(a). Normalizing the imaginary part of the corresponding eigenvalue λ_2 with the *en masse* frequency (Eq. 2.16) results in $f_{n,\lambda_2} = 3.4$, but the actual normalized traveling wave frequency is $f_{n,tw} = 2.61$. Hence, while the eigenvalue of the DMD mode alone does not reveal the traveling wave frequency directly, the temporal dynamics defined by the DMD model (Eq. 2.27) capture such a frequency correctly from the linear combination of the DMD modes.

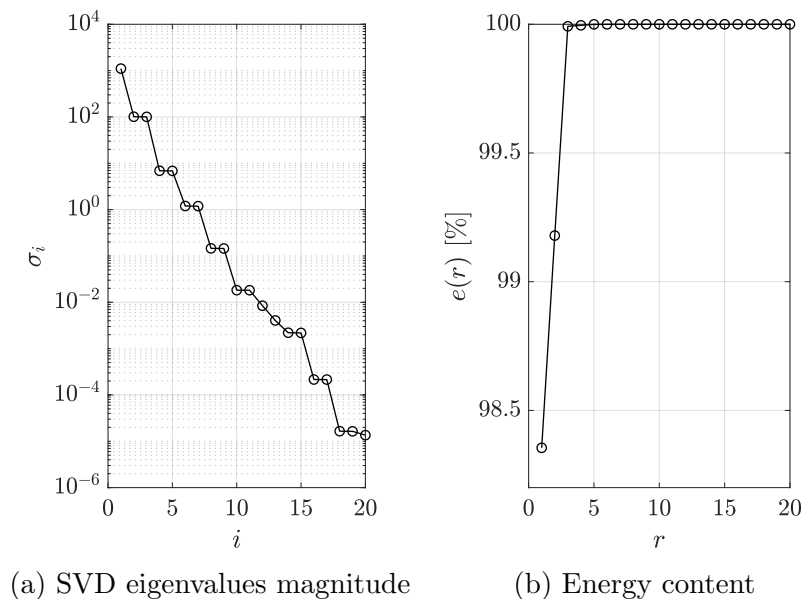


Figure 3.40: SVD eigenvalues for $\alpha = 80^\circ$, $\Pi_s = 20$

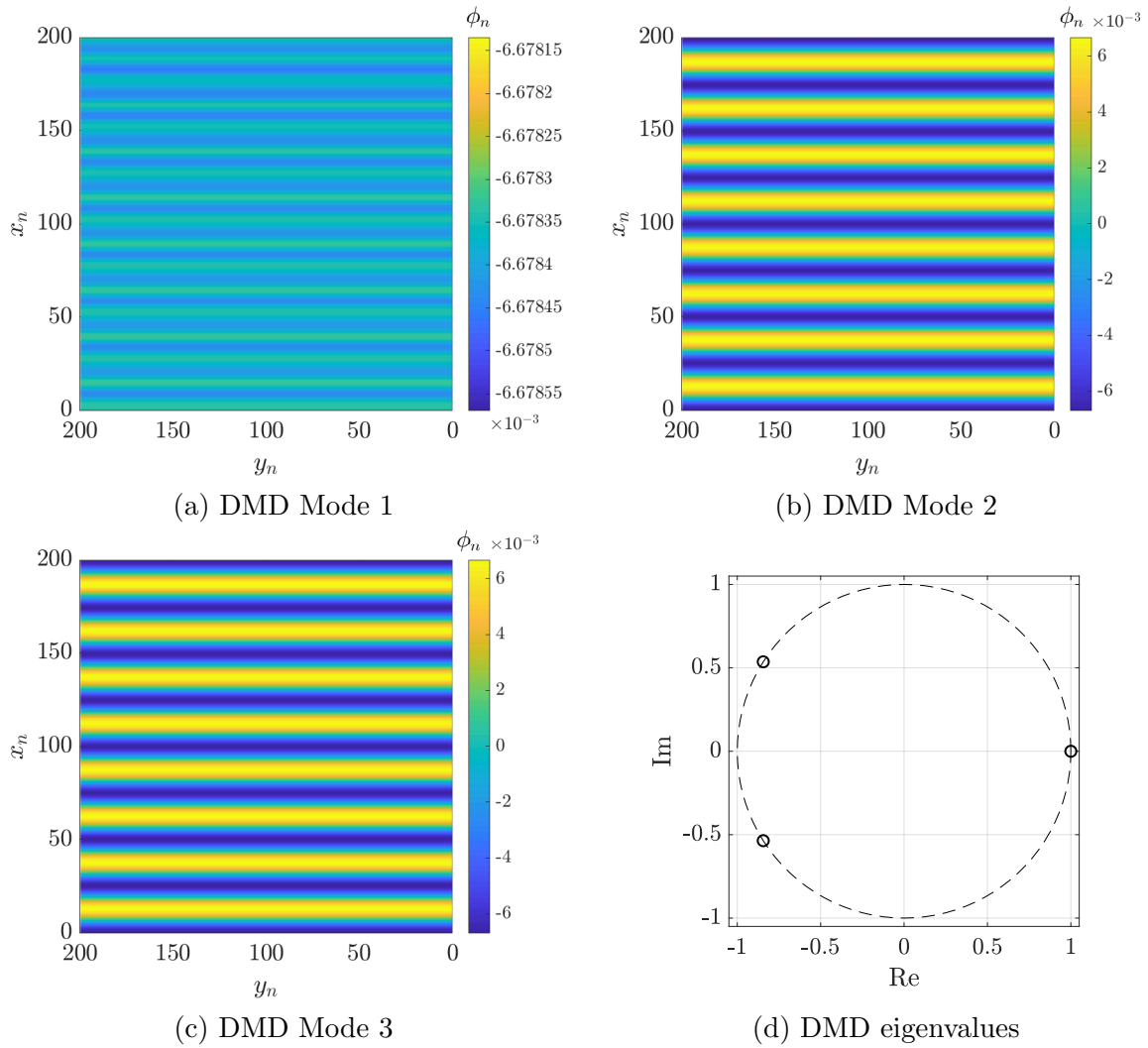


Figure 3.41: DMD modes and eigenvalues for $\alpha = 80^\circ, \Pi_s = 20$

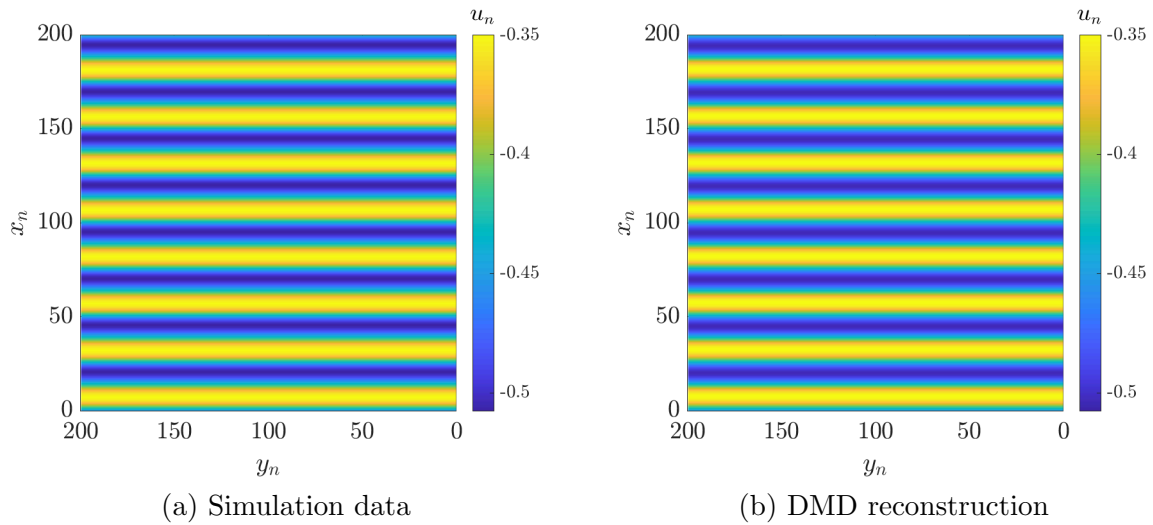


Figure 3.42: DMD reconstruction for $\alpha = 80^\circ, \Pi_s = 20$. Contour plot plotted at final snapshot of training data set

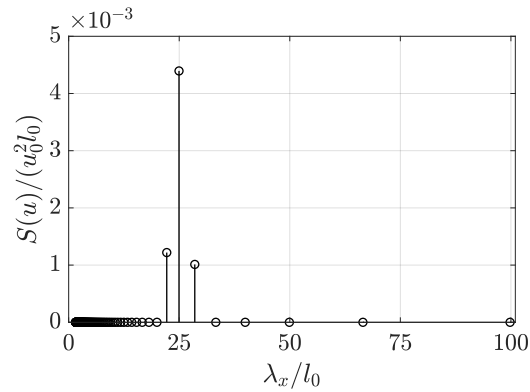


Figure 3.43: Spatial PSD of the second most dominant DMD mode for $\alpha = 80^\circ, \Pi_s = 20$. The wavelength in the along-slope direction is shown.

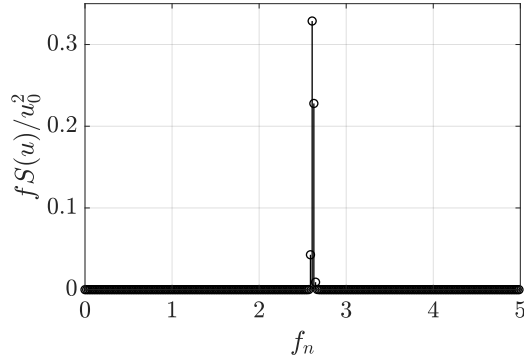


Figure 3.44: Temporal PSD from the DMD reconstruction for $\alpha = 80^\circ, \Pi_s = 20$

Mixed/Higher-Order Rolls

Extending the DMD analysis to the mixed modes regime reveals that the reduced model filters the contributions from the longitudinal and traveling wave rolls, and that the characteristics of the DMD models observed for the solitary instability rolls also apply when analyzed in such a filtered approach. Firstly, note how the magnitude of the eigenvalue drops after the first three SVD modes (Fig. 3.45(a)), which combined capture about 97.7% of the information contained in the data set (Fig. 3.45(b)). In this scenario, capturing at least 99% of the data set information would require more than 20 SVD modes, as opposed to the solitary modes cases, where at most 3 SVD modes were required to capture such a percentage. Note, however, that in the mixed modes regime, there is not much increase for $3 < r < 20$, hence $r = 3$ is chosen as the optimal reduction size. The obtained DMD modes for such a reduction size are shown in Fig. 3.46(a)-(c), and their corresponding eigenvalues are shown in Fig. 3.46(d). Note that the first DMD mode carries most of the information about the longitudinal rolls, while the other two modes carry the information about the traveling wave mostly. The eigenvalue of the first mode is $\lambda_1 \approx 1$, confirming that the first mode is stationary as observed for the solitary longitudinal rolls. The remaining modes, featuring complex eigenvalues, are traveling modes in the same way that was observed in the DMD model for the solitary traveling wave rolls.

Although in this case more information from the original data set is lost after the initial dimensionality reduction through SVD, the obtained DMD model still captures the major characteristics of the interwoven instability rolls, as seen in Fig. 3.47(b) in comparison with the simulation results shown in Fig. 3.47(a). Note that both instability types are present in the DMD reconstruction since Eq. 2.27 defines the linear combination of the DMD modes presented in Fig. 3.46(a)-(c). However, the DMD model underestimates the magnitude of the u -velocity field. Also, in the DMD reconstructed field, the traveling wave contributions are much stronger than the longitudinal rolls contributions, thus revealing that most of the discarded data set information corresponded to the longitudinal rolls, including their meandering and snaking dynamics. Figures. 3.48(a) and (b) show the most dominant wavelengths in the DMD modes 1 and 2, respectively, revealing that there are competing wavelengths for the longitudinal rolls component and a well-defined most dominant wavelength for the traveling wave component. Additionally, Fig. 3.49 presents the temporal frequency component which, as in the DMD model built for the solitary traveling wave rolls, also matches the exact frequency governing the oscillations observed in the simulation data (Fig. 3.3).

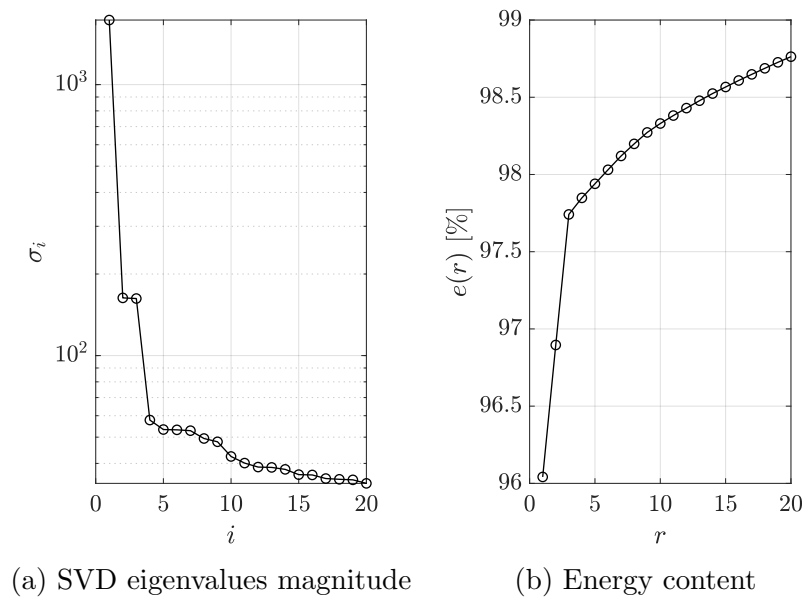


Figure 3.45: SVD eigenvalues for $\alpha = 60^\circ$, $\Pi_s = 30$

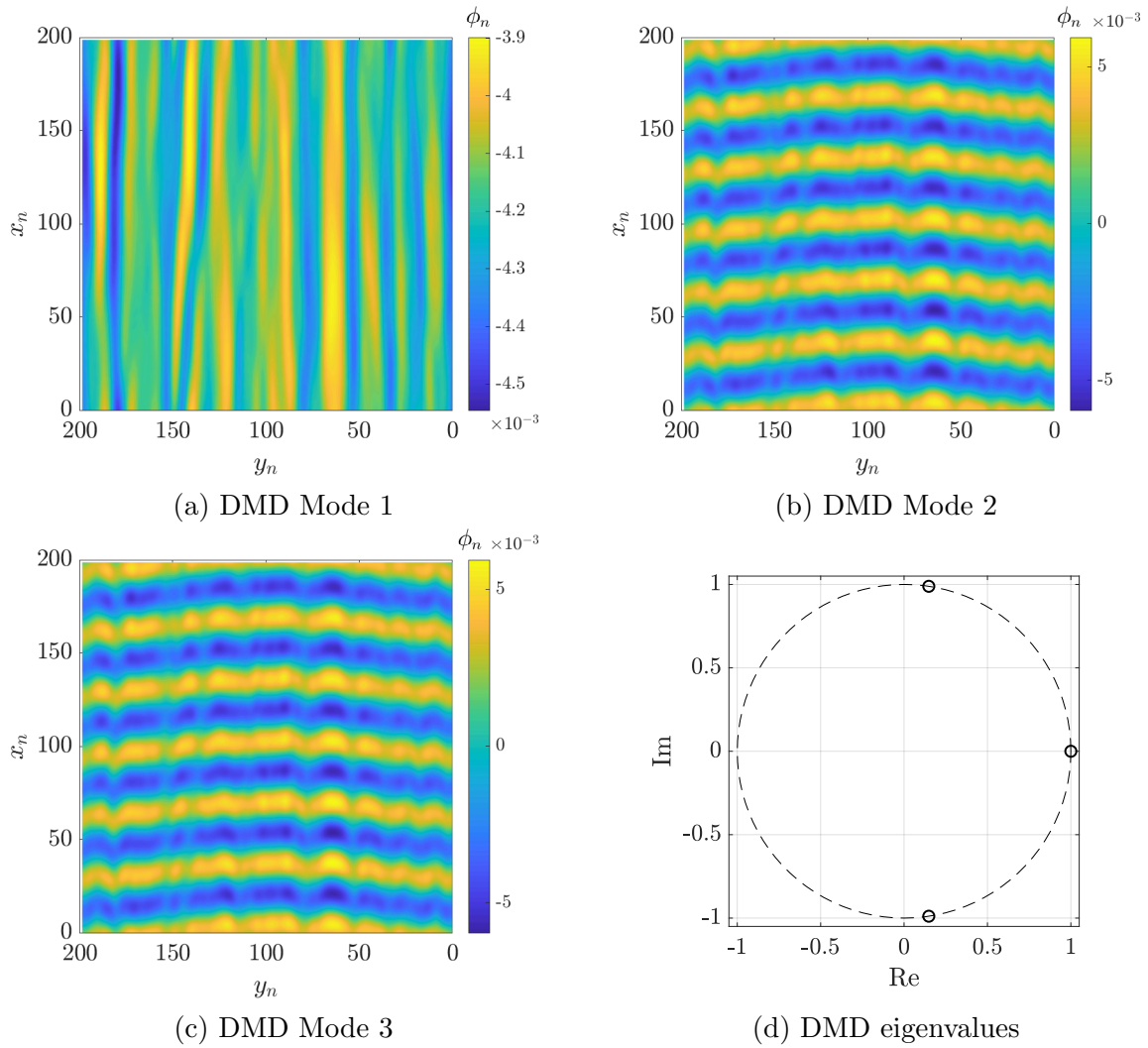


Figure 3.46: DMD modes and eigenvalues for $\alpha = 60^\circ, \Pi_s = 30$

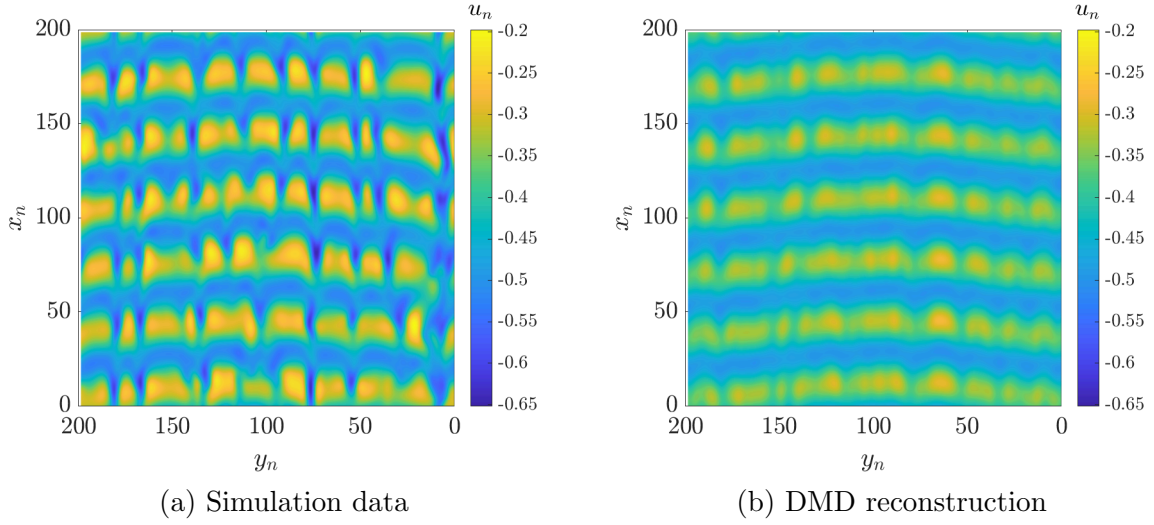


Figure 3.47: DMD reconstruction for $\alpha = 60^\circ, \Pi_s = 30$. Contour plot plotted at final snapshot of training data set

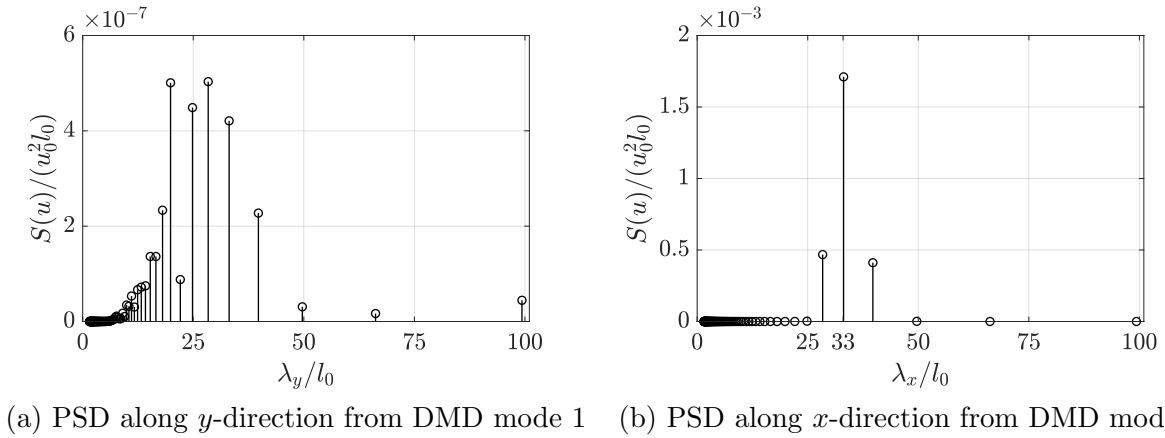


Figure 3.48: Spatial PSD of most dominant DMD modes for $\alpha = 60^\circ, \Pi_s = 30$

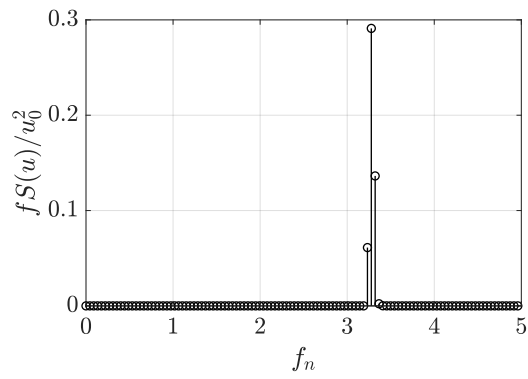


Figure 3.49: Temporal PSD from the DMD reconstruction for $\alpha = 60^\circ$, $\Pi_s = 30$

4.0 Summary

This chapter presents a summary of the main findings obtained from computer simulations carried out of idealized katabatic flows under multiple dynamically unstable configurations. Firstly, the overall characteristics observed across all the types of instability are presented, including the presence of the *en masse* oscillations and the observed vortical structures. Descriptions of the specific characteristics concerning the longitudinal and traveling wave rolls are then presented separately. Finally, recommendations for future works are outlined.

4.1 Overall Dynamics of Instabilities

Three distinct regimes were observed in the temporal signals for any of the flow fields. The flow experiences an initial oscillatory regime governed by the *en masse* oscillations, whose amplitude gets damped exponentially with a rate that is a function of the slope flow parameters. At later simulated times, a transition regime takes place once nonlinear infinitesimal disturbances in the flow have reached a saturation point, which triggers the emergence of the three types of instabilities predicted by instability maps reported in the literature. These instability modes, characterized by distinct types of organized vortical structures that have been visualized both through vorticity isosurfaces and flow field contour plots, persist in the flow field and define a quasi-stationary regime. In such a regime, the longitudinal rolls, corresponding to the transverse mode of instability, and the traveling wave rolls, corresponding to the longitudinal mode of instability, are large-scale structures that dominate the dynamics of the flow. For certain slope flow parameters, both types of instabilities coexist defining weakly-mixed and well-mixed regimes characterized by intricately interwoven instability rolls. At more dynamically unstable scenarios, the presence of these organized vortical structures weakens, and finer vortex scales were observed that correspond to the smaller eddies emerging as the flow breaks into turbulence. For temporal signals from the pressure

field, the amplitude of the *en masse* oscillations was observed to be in the same order of magnitude as the amplitude of the oscillatory dynamics of the flow in the turbulent regime, contrary to observations in the unstable laminar regime. Additionally, reduced-order models based in the dynamic mode decomposition were shown to capture well the dynamics of all observed instability types based on a limited number of low-dimensional structures. These reduced structures exhibit the most dominant characteristics of the solitary modes both in space and time and the reduced models provide a framework to filter the instability types in the mixed mode regime.

4.2 Longitudinal Rolls Dynamics

Longitudinal rolls, which appear at shallow slopes, are rolls observed to be aligned with the along-slope direction for all analyzed cases, although featuring curved and branched shapes for some slope flow conditions. These rolls exhibit either stable or unstable dynamics governed by the stratification perturbation parameter for a given slope angle and domain size. The rolls experience a sharp transition between these two states, being smooth and straight in the stable conditions and then exhibiting snaking and meandering behaviors in the unstable conditions. The longitudinal rolls, which remain stationary for all conditions, are destabilized when they start colliding with themselves without requiring any external perturbation. The average separation between these rolls was observed to be a strong function of the slope angle, with shallow slopes featuring large separations that decrease at steeper slopes, for which a weaker dependence on the stratification perturbation parameter is observed. The temporal dynamics of these rolls in the unstable laminar regime exhibit irregular and intermittent fluctuations which are not characterized by well-defined frequency components when analyzed through the frequency domain.

4.3 Traveling Wave Dynamics

The traveling wave rolls, which appear at steep slopes, correspond to vortical structures aligned with the cross-slope direction that have been observed to be transported by the mean katabatic flow jet velocity in the along-slope direction. The separation between the rolls is constant and they exhibit a well-defined frequency in the flow field signals collected in time. For a fixed slope of 80° , an apparent regime transition is observed for stratification perturbation parameter values higher than 38, for which the obtained wave speed is slightly higher than the mean jet velocity, and when this same parameter is greater than 50, then the track of the traveling wave is lost. For all flow conditions before such a regime transition, the wave speed, frequency, and separation between the rolls are all increasing functions of the stratification perturbation parameter values, with a weaker dependence on the slope angle. The traveling wave rolls were observed to be equally as strong for all flow fields and can dominate over the longitudinal rolls for some fields in the mixed modes regime. All presented results are valid at the jet's height predicted by Prandtl's laminar solution, and data collected at different heights away from the surface needs to be analyzed to assess if the observed characteristics of the traveling wave rolls can be generalized for all locations in the flow field.

4.4 Future Work

The ultimate goal of the presented numerical investigations of idealized katabatic flows is to enable the simulation of turbulent winds over complex terrains under stably stratified atmospheric conditions. To advance the field in this direction, some of the challenges that remain to be addressed are outlined below.

- The destabilizing effect that the along-slope domain size has over the emerging longitudinal rolls, with meandering and snaking behaviors observed for long domain sizes, which trigger the instability of the primary mode.

- The existence of intermittent and irregular fluctuations associated to the longitudinal rolls that have no well-defined frequency components.
- The presence of the *en masse* oscillations at certain heights away from the surface even when the traveling wave dominates in most regions of the flow.
- The presences of curved traveling wave rolls for long domain sizes along the cross-slope direction, which contradicts the straight and parallel rolls observed for smaller domains, but that remain to be continuous with a fixed separation between them.
- The regime transitions where abrupt changes in the traveling wave dynamics are observed leading to lose the track of such wave-like motions. Reduced-order models based on the dynamic mode decomposition can help understand the way the instability modes interact in such scenarios.
- The mixing interactions between the longitudinal and traveling wave rolls for certain slope flow conditions.
- The presence of stripe-like structures in u -velocity contours of turbulent katabatic flows, which could be attributed to either the signature of the longitudinal rolls or to numerical artifacts consequence of using small simulation domains.
- To carry out turbulent katabatic simulations with appropriate mesh resolution and sufficiently large domain sizes, such that the resolvability condition for DNS based on the Kolmogorov microscale is satisfied while providing a computational domain large enough for all relevant scales of motion to emerge.

Appendix A MATLAB Implementation of the PSD Estimate

```
1 %*****Defining the frequency domain for temporal signals*****
2     dt = t(2) - t(1);
3     Fs = 1/dt; %samples/sec = [Hz]
4     L = length(t); %Dataset size
5     NFFT = 2^(nextpow2(L)); %Nyquist frequency
6     f = (Fs/NFFT)*(0:(NFFT/2)); %Frequency vector
7
8 %*****Defining the wavelength domain for spatial signals*****
9     Fs = 1/dx; %samples/unit length = [1/m]
10    L = length(x); %Dataset size
11    NFFT = 2^(nextpow2(L)); %Nyquist frequency
12    k = 2*pi*(Fs/NFFT)*(0:(NFFT/2)); %Wavenumber vector
13    lambda = 2*pi./k; %Wavelength vector
14
15 %*****Computes FFT*****
16     %S represents the original signal
17     s = S-mean(S); %Fluctuating component of the signal
18     window = hann(L)'; %Hann window
19     s = s.*window;
20     factor = 2.02; %Windowed FFT = 2.02; no window = 1
21     Y = factor*fft(s, NFFT); %Two-sided FFT spectrum
22
23 %**FFT amplitude**
24     P2_FFT = abs(Y)/L;
25     P1_FFT = P2_FFT(1:(floor(NFFT/2+1)));
26     P1_FFT(2:end-1) = 2*P1_FFT(2:end-1);
27
28 %**PSD estimate**
29     P2_PSD = (1/(Fs*L))*abs(Y).^2;
30     P1_PSD = P2_PSD(1:(floor(NFFT/2+1)));
31     P1_PSD(2:end-1) = 2*P1_PSD(2:end-1);
```

Appendix B MATLAB Implementation of the DMD algorithm

```

1 function [Phi, omega, lambda, b, X_dmd] = DMD_fn(X1, X2, r, t, dt)
2 %Computes the Dynamic Mode Decomposition from a provided data set
3 %and returns all relevant data structures
4
5 %***Parameters***
6     % N: Number of measurements per snapshot
7     % M: Number of snapshots
8     % r: Number of DMD modes to use
9 %***Inputs***
10    % X1: Data matrix (N,M-1)
11    % X2: Shifted data matrix (N,M-1)
12    % r: Reduction size if r > 0.
13    %     Energy percentage to capture after the reduction if r < 0
14    % t: Dimensional time vector (1,M)
15    % dt: Dimensional time step between measurements in data matrix
16 %***Outputs***
17    % Phi: Unsorted DMD modes (N,r)
18    % omega: log(lambda)/dt (r,1)
19    % lambda: Unsorted DMD eigenvalues (r,1)
20    % b: Projection of the initial condition x1 = X1(:,1)
21    %     onto the DMD modes (r,1)
22    % X_dmd: Whole data set reconstructed using DMD for the times
23    %         specified in vector t (N,M)
24
25 %% ***** Singular Value Decomposition *****
26 %SVD of X1
27 [U, S, V] = svd(X1, 'econ');
28
29 %Plotting the magnitude of the singular values
30 sigma = diag(S);
31 semilogy(sigma, '-o', 'MarkerSize', 5, 'LineWidth', 1);
32 xlabel('Index'); ylabel('Eigenvalue magnitude');
33
34 %Plotting the energy content of each mode
35 e = []; %Energy vector
36 e_total = sigma'*sigma;
37 for i = 1:length(sigma)
38     e_r = sigma(1:i)'*sigma(1:i);
39     e(i) = e_r/e_total*100;
40 end
41 plot(e, '-o', 'MarkerSize', 5, 'LineWidth', 1);
42 xlabel('Reduction size'); ylabel('Energy percentage');
43
44 %Specifying the energy percentage instead of the reduction size: r<0
45 if r<0
46     r = find(e >= abs(r),1);
47 end
48

```

```

49 %Reduction
50 Ur = U(:, 1:r);
51 Sr = S(1:r, 1:r);
52 Vr = V(:, 1:r);
53
54 %% ***** Computing DMD for the reduction size r *****
55 %Build Atilde and DMD Modes
56 inv_Sr = inv(Sr);
57 Atilde = Ur'*X2*Vr*inv_Sr;
58 [W, D] = eig(Atilde);
59 Phi = X2*Vr*inv_Sr*W; % Exact DMD Modes
60 %Phi = Ur*W; % Projected DMD Modes
61
62 %DMD eigenvalues
63 lambda = diag(D);
64 omega = log(lambda)/dt;
65
66 %Compute DMD Solution
67 M = size(X1,2)+1;
68 x1 = X1(:,1);
69 b = Phi\x1;
70 time_dynamics = zeros(r, M);
71 for i = 1:M
72     time_dynamics(:,i) = (b.*exp(omega*t(i)));
73 end
74 X_dmd = Phi*time_dynamics;
75 end

```

Bibliography

- [1] R. B. Stull, *Meteorology for scientists and engineers*. Univ. of British Columbia, 3rd ed., 2011.
- [2] U. Schumann, “Large-eddy simulation of the up-slope boundary layer,” *Quarterly Journal of the Royal Meteorological Society*, vol. 116, no. 493, pp. 637–670, 1990.
- [3] E. Fedorovich and A. Shapiro, “Structure of numerically simulated katabatic and anabatic flows along steep slopes,” *Acta Geophysica*, vol. 57, no. 4, pp. 981–1010, 2009.
- [4] I. Senocak and C.-N. Xiao, “Linear Instability of Stably Stratified Down-Slope Flows,” in *Modeling and Simulation of Turbulent Mixing and Reaction*, pp. 47–68, Springer Singapore, 2020.
- [5] I. A. Renfrew, “The dynamics of idealized katabatic flow over a moderate slope and ice shelf,” *Quarterly Journal of the Royal Meteorological Society*, vol. 130, pp. 1023–1045, 4 2004.
- [6] A. Meesters, “Dependence of the energy balance of the Greenland ice sheet on climate change: Influence of katabatic wind and tundra,” *Quarterly Journal of the Royal Meteorological Society*, vol. 120, pp. 491–517, 4 1994.
- [7] T. R. Parish, “A Numerical Study of Strong Katabatic Winds over Antarctica,” *Monthly Weather Review*, vol. 112, 3 1984.
- [8] T. R. Parish and D. H. Bromwich, “Continental-Scale Simulation of the Antarctic Katabatic Wind Regime,” *Journal of Climate*, vol. 4, 2 1991.
- [9] H. Gallée and G. Schayes, “Development of a Three-Dimensional Meso- γ Primitive Equation Model: Katabatic Winds Simulation in the Area of Terra Nova Bay, Antarctica,” *Monthly Weather Review*, vol. 122, 4 1994.
- [10] J. Oerlemans, “The atmospheric boundary layer over melting glaciers,” in *Clear and Cloudy Boundary Layers*, vol. 48, pp. 129–153, Amsterdam: Royal Netherlands Academy of Arts and Sciences, 1998.

- [11] J. Lenaerts, S. Lhermitte, R. Drews, S. Ligtenberg, S. Berger, V. Helm, C. Smeets, M. Broeke, W. van de Berg, E. van Meijgaard, M. Eijkelboom, O. Eisen, and F. Pattyn, “Meltwater produced by wind–albedo interaction stored in an East Antarctic ice shelf,” *Nature Climate Change* 2017 7:1, vol. 7, pp. 58–62, 12 2016.
- [12] H. J. S. Fernando and J. C. Weil, “Whither the Stable Boundary Layer?: A Shift in the Research Agenda,” *Bulletin of the American Meteorological Society*, vol. 91, pp. 1475–1484, 11 2010.
- [13] H. Fernando, “Fluid Dynamics of Urban Atmospheres in Complex Terrain,” *Annual Review of Fluid Mechanics*, vol. 42, pp. 365–389, 12 2009.
- [14] J. A. Salmond and I. G. McKendry, “A review of turbulence in the very stable nocturnal boundary layer and its implications for air quality,” *Progress in Physical Geography: Earth and Environment*, vol. 29, pp. 171–188, 8 2005.
- [15] H. Fernando, S. Lee, J. Anderson, M. Princevac, E. Pardyjak, and S. Grossman-Clarke, “Urban Fluid Mechanics: Air Circulation and Contaminant Dispersion in Cities,” *Environmental Fluid Mechanics* 2001 1:1, vol. 1, no. 1, pp. 107–164, 2001.
- [16] R. Lu and R. P. Turco, “Air Pollutant Transport in a Coastal Environment. Part I: Two-Dimensional Simulations of Sea-Breeze and Mountain Effects,” *Journal of the Atmospheric Sciences*, vol. 51, 8 1994.
- [17] J. C. R. Hunt, H. J. S. Fernando, and M. Princevac, “Unsteady Thermally Driven Flows on Gentle Slopes,” *Journal of the Atmospheric Sciences*, vol. 60, 9 2003.
- [18] S.-M. Lee, H. J. Fernando, M. Princevac, D. Zajic, M. Sinesi, J. L. McCulley, and J. Anderson, “Transport and Diffusion of Ozone in the Nocturnal and Morning Planetary Boundary Layer of the Phoenix Valley,” *Environmental Fluid Mechanics* 2003 3:4, vol. 3, pp. 331–362, 12 2003.
- [19] A. J. Brazel, H. J. S. Fernando, J. C. R. Hunt, N. Selover, B. C. Hedquist, and E. Pardyjak, “Evening Transition Observations in Phoenix, Arizona,” *Journal of Applied Meteorology*, vol. 44, 1 2005.
- [20] L. Mahrt, “Stably stratified atmospheric boundary layers,” *Annual Review of Fluid Mechanics*, vol. 46, pp. 23–45, 2014.

- [21] A. S. Monin and A. M. Obukhov, “Basic laws of turbulent mixing in the surface layer of the atmosphere,” *Originally published in Tr. Akad. Nauk SSSR Geophys. Inst.*, vol. 24, no. 151, pp. 163–187, 1954.
- [22] C.-N. Xiao and I. Senocak, “Stability of the anabatic Prandtl slope flow in a stably stratified medium,” *Journal of Fluid Mechanics*, 2019.
- [23] G. S. P. Heywood, “Katabatic winds in a valley,” *Quarterly Journal of the Royal Meteorological Society*, vol. 59, no. 248, pp. 47–58, 1933.
- [24] T. W. Horst and J. C. Doran, “Nocturnal drainage flow on simple slopes,” *Boundary-Layer Meteorology*, vol. 34, no. 3, pp. 263–286, 1986.
- [25] C. G. Helmis and K. H. Papadopoulos, “Some aspects of the variation with time of katabatic flow over a simple slope,” *Quarterly Journal of the Royal Meteorological Society*, vol. 122, no. 531, pp. 595–610, 1996.
- [26] K. H. Papadopoulos, C. G. Helmis, A. T. Soilemes, J. Kalogiros, P. G. Papageorgas, and D. N. Asimakopoulos, “The structure of katabatic flows down a simple slope,” *Quarterly Journal of the Royal Meteorological Society*, vol. 123, no. 542, pp. 1581–1601, 1997.
- [27] A. Geiss and L. Mahrt, “Decomposition of Spatial Structure of Nocturnal Flow over Gentle Terrain,” *Boundary-Layer Meteorology*, vol. 156, no. 3, 2015.
- [28] I. Stiperski, A. A. M. Holtslag, M. Lehner, S. W. Hoch, and C. D. Whiteman, “On the turbulence structure of deep katabatic flows on a gentle mesoscale slope,” *Quarterly Journal of the Royal Meteorological Society*, vol. 146, no. 728, pp. 1206–1231, 2020.
- [29] L. Prandtl, “Führer durch die Strömungslehre,” *Vieweg und Sohn*, 1942.
- [30] F. Defant, “Zur Theorie der Hangwinde, nebst Bemerkungen zur Theorie der Berg- und Talwinde,” *Arch. Met. Geophys. Bioklim*, vol. A1, pp. 421–450, 1949.
- [31] E. Fedorovich and A. Shapiro, “Oscillations in Prandtl slope flow started from rest,” *Quarterly Journal of the Royal Meteorological Society*, vol. 143, no. 703, pp. 670–677, 2017.

- [32] V. N. Lykosov and L. N. Gutman, “Turbulent boundary-layer over a sloping underlying surface,” *Izv. Acad. Sci. USSR Atmos. Ocean. Phys.*, vol. 8, no. 8, pp. 799–809, 1972.
- [33] C.-N. Xiao and I. Senocak, “Stability of the Prandtl model for katabatic slope flows,” *Journal of Fluid Mechanics*, vol. 865, p. R2, 2019.
- [34] C.-N. Xiao and I. Senocak, “Linear stability of katabatic Prandtl slope flows with ambient wind forcing,” *Journal of Fluid Mechanics*, vol. 886, pp. 1–14, 2020.
- [35] P. J. Mason and S. H. Derbyshire, “Large-Eddy Simulation of the stably-stratified atmospheric boundary layer,” *Boundary-Layer Meteorology*, vol. 53, no. 1-2, pp. 117–162, 1990.
- [36] C. Umphrey, R. DeLeon, and I. Senocak, “Direct Numerical Simulation of Turbulent Katabatic Slope Flows with an Immersed-Boundary Method,” *Boundary-Layer Meteorology*, vol. 164, no. 3, pp. 367–382, 2017.
- [37] J. W. Miles, “On the stability of heterogeneous shear flows,” *Journal of Fluid Mechanics*, vol. 10, no. 4, pp. 496–508, 1961.
- [38] P. K. Kundu, I. M. Cohen, and D. R. Dowling, *Fluid Mechanics*. Elsevier, 6 ed., 2016.
- [39] D. A. Jacobsen and I. Senocak, “Multi-level parallelism for incompressible flow computations on GPU clusters,” *Parallel Computing*, vol. 39, pp. 1–20, 1 2013.
- [40] S. L. Brunton and J. N. Kutz, *Data-Driven Science and Engineering*. Cambridge University Press, 1 2019.
- [41] R. G. Lyons, *Understanding digital signal processing*. Pearson Education, 2011.
- [42] F. J. Harris, “On the Use of Windows for Harmonic Analysis with the Discrete Fourier Transform,” *Proceedings of the IEEE*, vol. 66, no. 1, pp. 51–83, 1978.
- [43] J. N. Kutz, *Data-Driven Modeling & Scientific Computation: Methods for Complex Systems & Big Data*. Oxford University Press, 2013.
- [44] P. Schmid, “Dynamic mode decomposition of numerical and experimental data,” *J. Fluid Mech*, vol. 656, pp. 5–28, 2010.

- [45] J. H. Tu, C. W. Rowley, D. M. Luchtenburg, S. L. Brunton, and J. N. Kutz, “On Dynamic Mode Decomposition: Theory and Applications,” *Journal of Computational Dynamics*, vol. 1, pp. 391–421, 11 2013.
- [46] J. N. Kutz, S. L. Brunton, B. W. Brunton, and J. L. Proctor, *Dynamic Mode Decomposition*. Society for Industrial and Applied Mathematics, 11 2016.
- [47] P. J. Schmid, L. Li, M. P. Juniper, and O. Pust, “Applications of the dynamic mode decomposition,” *Theoretical and Computational Fluid Dynamics*, vol. 25, pp. 249–259, 6 2011.
- [48] J. C. R. Hunt, A. Wray, and P. Moin, “Eddies, Streams, and Convergence Zones in Turbulent Flows,” in *Proceedings of the 1988 Summer Program*, pp. 193–208, Center for Turbulence Research, 1988.
- [49] P. G. Saffman, *Vortex Dynamics*. Cambridge University Press, 1 1993.
- [50] S. B. Pope, *Turbulent Flows*. Cambridge University Press, 8 2000.
- [51] O. Flores and J. J. Riley, “Analysis of Turbulence Collapse in the Stably Stratified Surface Layer Using Direct Numerical Simulation,” *Boundary-Layer Meteorology* 2011 139:2, vol. 139, pp. 241–259, 1 2011.